1-1-2013

Theoretical Investigation of the Water-Gas Shift Reaction At the Three Phase Boundary of Ceria Supported Platinum Metal Clusters

Sara Aranifard
University of South Carolina

Theoretical Investigation of the Water-Gas Shift Reaction at the Three Phase Boundary of Ceria Supported Platinum Metal Clusters

by

Sara Aranifard

Bachelor of Science
Sharif University of Technology, 2005

Master of Science
Sharif University of Technology, 2008

Submitted in Partial Fulfillment of the Requirements

For the Degree of Doctor of Philosophy in

Chemical Engineering

College of Engineering and Computing

University of South Carolina

2013

Accepted by:

Andreas Heyden, Major Professor

Donna A. Chen, Committee Member

Jochen Lauterbach, Committee Member

Christopher T. Williams, Committee Member

Lacy Ford, Vice Provost and Dean of Graduate Studies

Acknowledgements

I would like to thank my advisor, Professor Andreas Heyden for guiding, teaching, and inspiring the research in this dissertation. I appreciate all his contributions of time and ideas to make my Ph.D. experience productive and stimulating. My thanks and appreciation also goes to Dr. Salai Ammal, for spending her time in providing her useful perspectives on this research. I would like to thank my committee members, Dr. Christopher Williams, Dr. Jochen Lauterbach, and Dr. Donna Chen for all of their time, attention, and guidance.

I would like to thank the members of the Heyden's Group who have provided me a lot of support, particularly from Suwit Suthirakun, Sina Behtash, and Mian Muhammad Faheem. I would also like to thank a number of people I met while studying at USC who also helped me during these past 5 years: Zahra Nazar Poor, Behnam Bahrami, Saeed Khaleghi, Narges Kaveshgar, Kaveh Majidi, Saeedeh Mahdavisefat, and all my other friends who I hope I could mention them here.

I would like to thank my mother, Iran Ghasemi, for supporting me and encouraging me all the time and giving me the opportunity to pursue my dreams. I would like to thank my sisters and brothers, Sozan, Soheila, Soodabeh, Siavash, and Saeed for their trust and belief in me and I specially thank Sozan for providing me an endless support through the hard times of my life. I am thankful of my father, Akbar Aranifard, for his encouragements to be strong. I thank God for helping me all the time.

Abstract

The Water-Gas Shift (WGS: $CO+H_2O \leftrightarrow CO_2+H_2$) reaction is a key step in hydrogen fuel processing for mobile fuel cell applications. Since the reaction is equilibrium-limited and exothermic, high conversions are favored by low temperatures. However, conventional low-temperature shift catalysts are not active enough. Reducible oxide supported small noble metal clusters have shown excellent activity as low temperature WGS catalysts and it is generally believed that these catalysts are bifunctional. In other words, the reaction occurs at the three-phase boundary (TPB) of the noble metal, the reducible oxide, and the gas phase. The small noble metal cluster adsorbs/activates the CO molecules and the reducible oxide, in this study ceria, activates the water molecules to provide necessary hydroxyl groups in the vicinity of the metal cluster for further reaction. While many experimental observations suggest that the TPB is the active site of ceria supported noble metal clusters, no systematic theoretical investigation of the WGS reaction mechanism at the TPB of these catalysts has been reported that could unambiguously prove this hypothesis.

In this computational study, density functional theory (DFT+U) has been used to study the ceria (111) surface and the effect of small platinum clusters on the reducibility of the surface. Then, constraint *ab initio* thermodynamic calculations have been performed to determine a meaningful catalyst model for a systematic kinetic study of the platinum-ceria interface. Next, different reaction mechanisms have been investigated

from first principles and microkinetic reactor models based on parameters obtained from DFT+U and transition state theory are developed to study the effect of temperature and partial pressure of the gas phase environment and to compare various reaction mechanisms to experimental data. To conclude, the importance of the TPB of ceria supported Pt clusters for the WGS reaction is theoretically verified and a redox pathway involving the creation of oxygen vacancies at the Pt/ceria interface is identified as the most dominant reaction pathways at relevant experimental conditions.

Table of Contents

List of Tables

List of Figures

1. Introduction

The Water-Gas Shift (WGS) reaction is a key step in hydrogen fuel processing, methanol and ammonia syntheses, Fischer-Tropsch reaction, etc. [1-10]. Current commercialized WGS technology involves multiple stages/catalysts that are based on high temperature shift over Fe_2O_3/Cr_2O_3 catalysts in a temperature range of 350-450 °C and low temperature shift over $Cu/ZnO/Al_2O_3$ catalysts in a temperature range of 190-250 °C. However, this multi-stage technology is not suitable for mobile fuel cell applications because of its technical complexity, such as sensitivity to start-up/shut-down cycles [11, 12]. Besides, the catalytic reactor for these applications should have reduced volume and weight in order to be economical and the catalyst should be non-pyrophoric and oxidation tolerant upon exposure to air.

Since the WGS reaction is an equilibrium-limited exothermic reaction, high conversions are favored by low temperatures. However, conventional low-temperature shift catalysts are not active enough. Besides, due to the necessity of careful *in-situ* pre-reduction of these catalysts, they are very sensitive to start-up/shut-down cycles. Furthermore, they are pyrophoric and sensitive to air and the condensed water that may form during shut-downs. As a result, for mobile fuel cell applications, there is a need for new single-stage WGS catalysts that are active at low temperatures, specifically between 250-400 °C.

Reducible oxide supported noble metal clusters have shown excellent activity as low temperature WGS catalysts [13-17]. These catalysts, especially ceria supported noble metal clusters, also proved to be very successful in three-way automotive converters [18]. However, the operating condition in the WGS reaction is quite different from the conditions in auto converters. While the former should be carried out at reducing conditions with high partial pressure of hydrogen and at low temperatures, the latter operating condition is oxidative at high temperatures. Consequently, numerous investigations are related to improve these catalysts for the WGS reaction to make them more active, stable, and economic.

Generally, it is believed that noble metal catalysts supported by reducible oxides are bifunctional [16, 19-23]. In other words, the reaction occurs at the three-phase boundary (TPB) of the noble metal, the reducible oxide, and the gas phase; while the small noble metal cluster adsorb/activate the CO molecules, the reducible oxide, specifically ceria in this study, activates the water molecules to provide necessary hydroxyl groups in the vicinity of the metal cluster for further reaction. Even though there is experimental evidence about the importance of the three-phase boundary of ceria supported noble metal clusters, no systematic theoretical study related to the WGS mechanism over these catalysts has been reported and the role of each of the involved phases on the activity of the active site is still unclear.

In this work, we used the DFT+U method with PBE exchange correlation functional to study the ceria (111) surface and the effect of small platinum clusters on the reducibility of the surface. We also utilized the constraint *ab initio* thermodynamics method in order to determine a meaningful catalyst model for kinetic studies. Next, we

developed different reaction mechanisms with reasonably accurate reaction energies and barriers. After that it became possible to develop a microkinetic reactor model and to study the effect of temperature and partial pressure of the gas phase species on the reaction mechanism and key reaction intermediates.

The following chapters are organized as follows: Chapter (2) contains a literature review that is divided into four subsections. The first subsection is an overview of the WGS reaction. It briefly describes the reaction history and its industrial applications. Some thermodynamic considerations about the reaction will be described and more details about five different types of catalysts (high temperature shift, low temperature shift, moderate temperature shift, sour gas shift, and noble metal based catalysts) will be given. The second subsection is on ceria catalysts; from its current commercial use in three-way automobile converters to buffer the oxygen partial pressure to the more recent applications as catalytically active catalysts support. The third subsection is aimed at showing the importance of the bifunctional nature of ceria supported noble metal catalysts by describing many experimental observations that highlight the potential importance of the three-phase boundary as an active site for these catalysts. The final subsection of Chapter (2) reviews computational research on ceria surfaces. Next, Chapter (3) provides details on the computational methods used in this research. Chapter (4) describes the results of our computations for identifying a suitable catalyst model for mechanistic studies. And Chapter (5) describes the results of the mechanistic studies.

2. Literature Review

2.1. Overview of the Water-Gas Shift Reaction

The Water-Gas Shift (WGS) reaction is a well-known process to increase hydrogen yield from hydrocarbon reforming and to decrease the CO concentration.

$$CO + H_2O \leftrightarrow CO_2 + H_2$$
$$\Delta H_{298K} = -41.1 \quad kJ\ mol^{-1}$$

It was first reported in 1888 [24]; and years later, in 1913, the reaction was applied industrially in the ammonia synthesis process [25]. Since iron based catalysts for ammonia synthesis are sensitive to carbon oxides, the WGS became important to convert carbon monoxide into carbon dioxide that can be separated in subsequent separation processes.

The name of the WGS reaction comes from the "water-gas" or "synthesis gas" that is a mixture of carbon monoxide and hydrogen. It has wide industrial usage. For instance, in the ammonia [3-6], methanol [7, 8, 26, 27], and hydrogen syntheses [1, 2, 28-36], hydrogenation steps in petroleum refining and petrochemical industry [9, 36], Fischer-Tropsch process [9, 10, 37-40], and also reduction of oxide ores to produce metals [41, 42].

Carbonaceous materials like coal, coke, natural gas, naphtha, etc. can react with steam, oxygen, or carbon dioxide to produce water-gas with different ratios of hydrogen to carbon monoxide. For instance, in steam reforming of coal and dry reforming methane

the ratio is one [11]. However, in partial oxidation of methane the ratio increases to two and in steam reforming of methane it is as high as three.

steam reforming of coal:

$$C + H_2O \leftrightarrow CO + H_2 \qquad \Delta H = 131.2 \quad kJ\ mol^{-1}$$

dry reforming of methane:

$$CH_4 + CO_2 \leftrightarrow 2CO + 2H_2 \qquad \Delta H = 247.4 \quad kJ\ mol^{-1}$$

partial oxidation of methane:

$$CH_4 + 0.5O_2 \leftrightarrow CO + 2H_2 \qquad \Delta H = -35.6 \quad kJ\ mol^{-1}$$

steam reforming of methane:

$$CH_4 + H_2O \leftrightarrow CO + 3H_2 \qquad \Delta H = 206.3 \quad kJ\ mol^{-1}$$

In order to increase the hydrogen yield, the WGS reaction can be utilized to have higher hydrogen to carbon monoxide ratios. As a consequence, this reaction step is becoming very important in many aspects of catalyst and reactor design to adjust the ratio of hydrogen to carbon monoxide depending on its usage.

In the first generation of WGS reactors, the reaction was conducted in a single stage at temperatures around 450-600 °C with an iron oxide catalyst stabilized by chromium oxide [43, 44]. In order to improve the performance, the reaction was then conducted in two stages with the same catalyst and the second stage at temperatures of around 320-360 °C. The two stage reactor reduced the carbon monoxide level to 3000-4000 ppm, while the single stage reactor could not reduce the CO level below 10000 ppm [45]. Already in the 1960s could the CO level be reduced to less than 5000 ppm [46] by using

Cu based catalysts in the low temperature stage and optimizing the high temperature Fe-based catalysts.

Following the increasing demand for hydrogen production since the beginning of the 20th century, the WGS has again become very important. Using natural gas instead of coal for water-gas production and employing better catalysts that improve the yield and selectivity this increasing demand can likely be met. It is worth mentioning here that nowadays environmental concerns are very crucial. For instance, hydrogen production from synthesis gas for fuel cell applications has found huge attention. And there is a growing need for new non-pyrophoric catalysts which can provide H_2 safer and at more efficient reaction condition such as low operating temperatures.

Next, it is noted that the WGS reaction is an equilibrium-limited and exothermic reaction. As a result, hydrogen production is favored at low reaction temperatures. However, at low temperatures the reaction is controlled by the kinetics and it is vital to make highly active and stable catalysts for these conditions. The pressure does not affect the equilibrium of the reaction since there is no variation in the number of moles during the reaction. However, until reaching equilibrium, a high total pressure positively affects the CO conversion since it increases the reaction rate.

Traditionally the reaction is conducted in two or three catalytic stages with the first stage operating at relatively high temperatures and subsequent stages working at lower temperatures [43]. While the first stage is favoring fast CO conversion and low residence time, the following stages increase the conversion which is limited by the reaction equilibrium.

Catalysts for the WGS reaction can be classified into 5 main groups [11]. The first group consists of high temperature shift catalysts which are based on iron oxide and perform best at relatively high temperatures between 350 °C and 450 °C. The second group consists of low temperature shift catalysts which are primarily copper-zinc oxides that work best at low temperatures between 190 °C to 250 °C. Medium temperature shift catalysts are usually copper-zinc oxides modified by iron oxides and operate between 275 °C to 350 °C. The fourth group consists of sour gas shift catalysts. These catalysts are sulfur tolerant and can be used for feed streams that are sour. The active ingredients in these catalysts are usually cobalt and molybdenum. Finally, precious metal based catalysts such as platinum and gold group catalysts can be categorized in a fifth group.

This group of WGS catalysts is currently under intensive investigation for use in fuel cell applications especially for mobile applications like automobiles. For instance, the catalyst bed for these applications should have a reduced volume and weight to be economical and should also be robust enough to withstand rapid start-up and shut-down conditions. Since a multi-stage technology for the reaction is sensitive to start-up and shut-down cycles it is desirable to conduct the reaction in a single stage and since the reaction is exothermic and equilibrium limited it should occur at relatively low temperatures. The catalyst should be non-pyrophoric and oxidation tolerant upon exposure to air. Considering these needs, precious metal based catalysts are very promising. In the following, more details about each group of the introduced catalysts will be given.

As high temperature shift catalysts, Fe_2O_3-Cr_2O_3 based catalysts have been in commercial use for more than 60 years [11]. Conventional catalysts contain about 80-90

wt% of Fe_2O_3, 8-10 wt% of Cr_2O_3 and some promoters and stabilizers like copper oxide, Al_2O_3, alkali, MgO, ZnO, etc. [47-51]. While pure Fe_2O_3 deactivates fast during the reaction due to sintering of iron oxide crystallites, Cr_2O_3 prevents the sintering of iron oxide crystallites by being a textural promoter. Cr_2O_3 also functions as a structural promoter that increases the intrinsic catalytic activity of Fe_2O_3. These catalysts have a life time of 3-5 years depending mainly on the operating temperature and are not very sensitive to the presence of sulfur, even up to about 1000 ppm. Their deactivation is mainly caused by loss of iron oxide surface area due to thermal sintering.

Due to the exothermic nature of the WGS reaction it is necessary to provide adequate heat removal stages to the reacting system to control the temperature [11]. Therefore, these catalysts are used in two or three beds with inter-bed coolers. Under normal operating conditions, the outlet temperature can vary between 400 and 500 °C with CO content between 3-5 wt% while the reactor inlet temperature is about 300 to 360 °C. The operating pressure is usually between 10 to 60 bars.

Three major drawbacks can be mentioned for this group of catalysts especially for mobile fuel cell applications. First of all, Cr^{+6} ions are water soluble toxic ions which pose major hazards during the catalyst manufacturing and handling. The second major drawback of these catalysts is their low activity at low temperatures which necessitating large catalytic beds that is not desired for mobile applications. Finally, they are pyrophoric.

Relatively poor efficiency of the conventional Fe_2O_3-Cr_2O_3 at low temperatures motivated further investigation for low temperature shift catalysts. Even though the

activity of metallic copper in the WGS reaction had been known for a long time, easy copper sintering necessitated the use of supports [52]. Various supports like Al_2O_3, SiO_2, MgO and Cr_2O_3 were examined but all of them had a relatively short life time and low activity [11]. Important progress was made in early 1960s by the introduction of ZnO as catalyst support [53], and later by ZnO-Al_2O_3. These Cu-ZnO-Al_2O_3 catalysts provide high and more stable copper surface area and are used almost exclusively in industrial low temperature shift reactions [11].

Even though high surface area of copper is necessary for catalytic activity, it is also probable that the presence of Zn ions affects the structure of copper nano-crystallites and provides an increased activity of the catalyst [11]. If formulated properly and operated under standard low temperature shift conditions, Cu-ZnO-Al_2O_3 catalysts can have a life time of a few years. The major causes of catalysts deactivation are sulfur and chloride poisoning and thermal sintering of copper crystallites [54-58]. These catalysts sinter and lose copper surface area and catalytic activity when heated above 300 °C and one major role of Al_2O_3 is to prevent the growth of copper crystallites and functions as a textural promoter [55]. Since loss of copper surface area and catalytic activity begins above 250 °C where copper clusters start agglomerating on the ZnO support [57], it is probable that the active site for the WGS reaction is related to small copper clusters [59].

Using well-formulated, rugged Cu-ZnO-Al_2O_3 catalysts in low temperature shift reactors with an exit temperature of 200 °C, the CO level can be reduced to a value of about 0.3 wt% [11]. The lower limit of the operating temperature in the reactor is the dew point of water at the operating pressure (190-200 °C at 30 bar) since condensed steam adversely affects the catalytic activity of this group of shift catalysts.

As mentioned, one major drawback of these catalysts is their extreme sensitivity to sulfur poisoning [55, 60, 61]. For example, the sulfur levels in natural gas or light petroleum naphtha are in the range of 5-50 ppm and conventionally desulfurization steps have to be applied upstream to reduce the sulfur content of the feed to the water-gas shift reactor to about 10 ppb since Cu-ZnO-Al_2O_3 catalysts are adversely affected by higher sulfur contents [11]. As a result, the volume of the actual low temperature shift reactor is three times larger than the volume needed by the WGS kinetics alone and in cases that the synthesis gas has a high level of sulfur content it is ultimately necessary to use a sulfur-tolerant WGS catalyst.

When the synthesis gas is generated by the gasification or partial oxidation of heavy fuel oil, tar sands, oil shale, coal, coke or biomass, the CO and sulfur concentrations are high (up to 50 and 3 wt% respectively) [11, 53, 62]. Under these conditions, the Cu-based low temperature shift catalysts cannot be used and the high temperature shift catalysts will have a low activity due to sulfidation. As a result, it is necessary to remove sulfur compounds from the process stream before it enters the shift reactor. This reaction can be carried out using sulfided Co-Mo-alumina catalysts [63-65]. Since these cobalt and molybdenum based catalysts can also remove CO by the water-gas shift reaction, they can be classified as sulfur-tolerant, sour gas shift catalysts. These catalysts are mainly active in their sulfided form and the non-sulfided form of them has very little activity toward the WGS. So it is preferred that the minimum sulfur content of the feed stream be about 300 ppm [11].

Commercialized catalysts operate in a temperature range of 250 to 350 °C and pressure range of 1 to 40 bars [11]. Addition of alkali to the sulfided form of these catalysts

promotes their water-gas shift activity [66-68]. Different factors may cause deactivation of these catalysts; for instance, sulfur and coke deposition, active site sintering, and poisoning [69-71]. High concentrations (above 0.5%) of NH_3 and HCN will affect the sulfided Co-Mo catalysts adversely [11]. Phenol is poisonous but the rate of deactivation is low at low concentrations and deactivation is reversible and the catalyst can be regenerated by steam-air regeneration. Benzene is also poisonous at high concentrations (about 10%). Chloride is the main poison for this group of catalysts even at low concentrations of about 1-2 ppb that deactivates the catalyst irreversibly.

As mentioned before future mobile fuel cell applications have imposed an urgent need for active, robust, non-pyrophoric, and oxidation tolerant catalysts that can be used in a single, compact, low temperature reactor. Commercialized Cu-ZnO catalysts are not suitable since they require a lengthy *in situ* pre-reduction during which the temperature must be increased very gradually to prevent the agglomeration of metal [12]. As a result they are very sensitive to start-up/shut-down cycles. Besides they are sensitive to air and water. Considering that for automobile fuel processing the chamber is exposed to air leaking and water condensation during shutdowns, these catalysts are not a good choice for these applications.

Precious metal based small nanoclusters supported on reducible oxides are subject to intense investigation as the activity of platinum group metals for the water-gas shift reaction is known for many decades even though their high price precluded them from becoming commercialized for industrial applications [72]. Besides, these catalysts could be used as automobile exhaust catalysts [18, 73-77]. However, it should be noted that auto exhaust catalysts operate under an oxidative atmosphere and the temperature is above 400

°C, while the WGS reaction in fuel processing occurs under reducing condition with high partial pressure of hydrogen and a temperature between 180 to 450 °C.

Precious metals such as Au, Pd, and Pt on reducible oxides such as ceria, titania, zirconia, and mixed oxides like ceria-zirconia have been mostly investigated [13-17, 78-92]. Other transition metals like cobalt and nickel have also been investigated; however, they mostly catalyzed methanation of CO especially below 350 °C [11]. Next, it has been shown that precious metal based catalysts supported on reducible oxides are bifunctional [16, 19-23, 72, 81, 93-99]. In other words, both metal and support have a considerable influence on the activity of the catalyst and it is commonly agreed upon that the metal adsorbs and activates CO while the oxide support activates H_2O.

Even though a large number of different formulations have been examined and reported, a meaningful comparison and ranking of various catalysts is difficult since the preparation method, feed composition, and reaction condition considerably affect the catalyst activity [100]. In an attempt to compare catalytic activity of some oxide supported metals for the WGS reaction, Thinon et al. [81] examined catalysts based on Pt, Au, Cu, Rh, Pd, and Ru on ceria, alumina, zirconia, iron oxide, and titania with the same preparation methods in a temperature range between 250 to 350 °C and 1 bar. The feed stream had a composition of typical reformate consisting of 10% CO, 10% CO_2, 20% H_2O, 30% H_2 and 30% Ar. Rh and Ru based catalysts showed a significant amount of methanation while Pt/TiO_2 and Pt/CeO_2-Al_2O_3 are the most active WGS catalysts at 300 °C. It is interesting to note that the Pt based catalysts had the highest apparent activation energies while the Au based catalysts had the lowest. This trend was consistent with other studies [101-103].

The low apparent activation energy for gold catalysts is very interesting since Au catalysts can then potentially be used for low temperature shift reactions between 180 to 250 °C where Pt group metals are not sufficiently active [11, 104, 105]. The activity of gold catalysts supported on reducible oxides is associated with a high dispersion of small gold nano-particles and it is known that pure gold surface is not catalytically very active [102, 106-121]. This phenomenon can usually be generalized to other transition metals. In other words, low coordinated transition metal atoms are usually more active in catalytic reactions than high coordinated atoms, since they have higher lying d states which make it easier for adsorbates to interact with them [109, 122]. Even though quantum size effects are important for very small particles [123], they seem not to have a considerable effect if metal particles are larger than 1.5 nm [11].

Considering Pt/TiO_2 catalysts, even though they are very active and selective for the WGS reaction, they deactivate with time on stream [124]. Catalyst deactivation during the reaction was also observed for palladium catalysts supported on ceria [125, 126]. Many mechanisms have been suggested for catalysts deactivation. For instance, over reduction of ceria, metal agglomeration, metal encapsulation by the support, and active sites poisoning by CO or other intermediate species [12, 124, 127].

Analyzing experimental observations to study the deactivation mechanism is not easy. For example, just because there is high surface coverage of one species does not mean that that species is causing deactivation [11]. If it is so, the coverage should increase with time. However, loss of metal support interaction, for example by metal particle growth, can also cause the coverage of intermediates to increase in case that the metal particle is assisting those intermediates decomposition at its interface with the support.

To summarize, catalyst deactivation of this group of catalysts is a major obstacle for their commercialization for the WGS reaction. Studies in industry showed that the addition of elements from rare earth metals like lanthanum or praseodymium to the ceria-zirconia support can reduce the agglomeration of ceria crystallites to some extent [128-130]. As a consequence, deactivation of Pt-ceria-zirconia can also decrease. Besides, Pt group metals have high activity for Fischer-Tropsch reactions especially at temperatures between 200-350 °C [11]. Once hydrocarbons form they may undergo further reactions like carbonization to block active sites for the WGS reaction. Since ionic Pt is active in redox reactions but not known to be active for Fischer-Tropsch, it has been suggested that by incorporating metal in lattice sites of ceria and preserving the ionic state of it under the WGS reaction conditions, one may be able to reduce the deactivation of these catalysts and also increase the stability of the catalyst [131-134].

Gold catalysts are even more prone to deactivation compared to Pt group catalysts during the reaction [122, 135]. One approach to improve their performance is to combine Au with another metal like Pt to have bimetallic catalysts [135, 136]. Otherwise, promoters can be incorporated in the ceria support. For instance, alumina can be utilized as a textural promoter to stabilize the Au and ceria crystallites against agglomeration during the reaction [137]. Alumina addition also results in smaller ceria crystallites and hence increased oxygen storage capacity of ceria. It has been suggested that there is a direct relationship between oxygen storage capacity of the catalysts and their activity towards the WGS reaction [136, 137]. Structural promoters can also be utilized in other Pt group catalysts [138]. For example, using nanocomposites of ceria and silica for the platinum support can improve the activity and thermal stability of these catalysts.

2.2. Overview of Ceria Catalysts

Cerium oxide, also known as ceric oxide, cerium dioxide or ceria, is a vital component in automotive catalysis [139]. The primary importance of ceria in catalysis is due to its remarkable oxygen storage capacity. Ceria can undergo rapid redox cycles without decomposition of the material depending on the partial pressure of oxygen in its environment. Due to these redox properties, ceria can be a co-catalyst for many important reactions where it can be used as a support or promoter for another catalytic material. Even though the original application of ceria was in automotive for emission control, recently it is finding new applications for example in hydrocarbon reforming, hydrocarbon oxidation, Fischer-Tropsch catalysis, and also the WGS reaction. Application of the redox properties of ceria in the WGS reaction was described in the previous section. In the following more details of other applications will be given.

Commercial use of automotive catalysts for detoxification of exhaust gas dates back to 1975 where the catalysts were noble metals free of ceria [18]. These catalysts aimed mainly at fully oxidizing the residual uncombusted hydrocarbons and carbon monoxide as the major byproduct of the partial combustion by applying excess oxygen to the hot exhaust stream. However, by early 1980s, emission standards for NO_x in the US had been tightened to the point where NO_x removal was needed in addition to hydrocarbon and carbon monoxide removal. By that time use of noble metals, as the only sufficiently active catalyst, was adapted to be economical with monolithic catalysts. The monoliths were multi-channeled ceramic catalytic bodies with the exhaust stream flowing through channels [140, 141]. The walls of the channels were coated by a porous layer with high surface area having finely dispersed noble metal catalytic particles.

Using precious metals such as platinum group metals, as the active component in automotive converters was based on three main factors: first of all, the catalyst should be active enough to remove pollutants from the exhaust gas stream with a large volumetric flow in a compact space and only precious metals were active enough to meet this very short residence time criterion. Second, the catalyst should be resistant to residual amounts of sulfur oxides in the exhaust gas stream and precious metals could meet this criterion too. Finally, dispersed precious metal particles supported on insulator oxides of alumina, zirconia, etc. were less prone but not totally immune to deactivation, given the high temperature of the exhaust stream. While initially platinum and palladium where used as the precious metal particles, rhodium was later introduced due to its higher activity for the catalytic reduction of the oxides of nitrogen.

As mentioned before, by the 1980s instead of just two major pollutants there were three to be removed from the exhaust stream: hydrocarbon, carbon monoxide, and NO_x. While hydrocarbon and carbon monoxide needed oxidizing conditions with excess air for their conversion, noxious materials needed to be reduced to nitrogen with excess fuel. However, if the air-fuel ratio could be controlled sufficiently close to the stoichiometric value, all three pollutants could be converted with high efficiency in a single step.

Using closed-loop engine control, the idea was to monitor the exhaust gas oxygen [142]. If at any time the oxygen partial pressure deviates to provide net oxidizing or net reducing environment, then the sensor should send a signal back to the electronic engine control module. This module, in turn, signals the fuel injectors to increase or decrease the fueling rate as to drive the exhaust gas mixture back to the stoichiometric point. Considering that by utilization of any control system there are still unavoidable

deviations from set point composition, ceria was added to the catalytic formulation of automotive catalysts to buffer the exhaust composition through its oxygen storage capacity.

As the first generation of this type of catalysts, noble metals were impregnated onto an alumina porous layer of a monolithic media. Ceria with small weight fraction was co-impregnated onto alumina along with the noble metals. Even a small fraction of ceria could dramatically improve the catalyst performance. In the late 1980s and early 1990s, more ceria usage was adapted since it was less expensive compared to precious metals. The primary concern was then to provide high contact surface area of ceria and the precious metals considering that the effectiveness of the oxygen storage capacity of ceria is to store and supply oxygen to the metals on which CO oxidation occurs. However, the oxygen came mainly from the surface or near surface region of ceria at the interface with the metal particles so that sintering of either ceria or the metal particles was a major problem for these catalysts. Thermal sintering was very eminent due to the high temperature of the exhaust gas stream which was more than 800 °C.

In the 1990s, the requirement for durability of the auto catalysts increased from 50000 miles to 100000 miles. In order to solve the problem of thermal deactivation of high ceria loaded catalysts, new technology for oxygen storage became inevitable. As a result, ceria was stabilized by another metal oxide to form a solid solution able to withstand severe thermal aging [143-147]. It is worth mentioning that, even though stabilization of ceria particles by addition of secondary oxides is important, the importance of reducible oxide solutions is not restricted to stabilization. For instance, solid solutions of ceria and zirconia increase the oxygen storage capacity of these

materials [148, 149]. Even bulk oxygen can diffuse to the surface and consequently it becomes possible to relax the constraint of a high surface area of the monolith catalysts.

Currently exhaust emission control for gasoline engines has been well developed and the aim is to develop catalysts stable enough to withstand any exhaust stream without deactivation over the life of the vehicle. The other effort is to reduce the contributions of the transport system to the accumulation of CO_2 in the atmosphere. One solution is to completely replace fossil fuels with hydrogen, ideally derived from solar energy. However, more time is needed to develop an affordable technology. The other, more promising, solution is to use fuel cells as the power source of automobiles by electrochemical conversion of hydrogen into electricity which is known to have a very high theoretical efficiency. The problem is then the low volumetric energy density of hydrogen which is a practical problem for on-vehicle storage and also hydrogen fuel distribution. As a solution, it is proposed to reform liquids such as alcohols or gasoline on-board to hydrogen to be used in the fuel cell for electricity generation.

Alcohol fuels such as methanol have a five to seven times higher energy density compared to compressed hydrogen and they can be easily stored and distributed [150]. Besides, renewable sources such as biomass can be used as the primary source for them to have net zero contribution to the CO_2 accumulation in the atmosphere. Furthermore, conversion of methanol is much simpler compared to other liquid fuels. Next, gasoline, another source for hydrogen production, has this advantage that it is already widely available. In other words, there is no need to think about new fuels and a new distribution system.

Reforming an oxygenated or non-oxygenated hydrocarbon fuel requires breaking the chemical bonds in the fuel to have CO and H_2 molecules. It is usually done by steam or a mixture of steam and oxygen. Use of oxygen provides an extra path for partial oxidation of the fuel which is exothermic and the heat is used in steam reforming that occurs simultaneously. Then it is needed to shift CO further into CO_2 for additional hydrogen production via the WGS reaction. After removal of CO_2, more purification of hydrogen from CO is needed to make it ready to be fed to the fuel cell electrode.

Among many candidates for catalysts of these reactions, noble metals surpass others due to special needs which arise for automotive catalysis, mainly activity and also safety and reliability. However the situation is quite different for these applications compared to emission control application [18]. First and foremost, the system should work flawlessly which means any possible disturbance or malfunction would likely have undesirable effects on the vehicle performance. The other difference is the amount of noble metals usage between the two applications. As a rough estimation, about 100-150 gr of precious metals are necessary for un-board fuel reforming and the fuel cell itself to produce 50 kW power. This value is much higher than for emission control (about 2-5 gr for a similar engine power of 50 kW).

The high price of noble metals motivates the search to find less expensive, still highly active catalysts. For example, nickel-based catalysts supported on ceria have been studied for hydrogen production via steam reforming of ethanol [151-153]. Although these catalysts are prone to coke deposition, by using a support with good redox properties and an appropriate promoter it was possible to reduce carbon formation [151]. For example, mixed oxides of ceria and zirconia showed less carbon formation for these catalysts.

Similarly, $Ce_{0.8}Ni_{0.2}O_{2-y}$ has been suggested to be a highly efficient, stable, and inexpensive catalyst [154]. Under the reaction conditions, the catalyst had small metal particles dispersed on partially reduced nickel-doped ceria. It was found that metal-oxide interactions alter the electronic properties of Ni and make it less active for methanation. The nickel embedded in ceria induced the formation of oxygen vacancies and facilitated the dissociation of ethanol and water. So both metal and metal-doped-oxide phases were found to be important for ethanol steam reforming.

For on-board reforming of diesel fuels through autothermal reforming, a catalyst with $Rh_{3.0}Ce_{10}La_{10}/\delta\text{-}Al_2O_3$ formulation has been proposed in the form of a monolith catalyst [155]. The activity results showed high fuel conversion and hydrogen production with 3 wt% of rhodium. The characterization results showed the presence of highly dispersed Rh particles in the support. Rhodium oxides where found both on the surface and in the bulk. Considering cerium and lanthanum as dopant, cerium oxides were found both in the bulk and on the surface and lanthanum was dispersed on the surface. These promoters were believed to improve the catalyst activity and durability.

Next, ceria catalysts are used for the preferential oxidation of CO (PROX). Proton exchange membrane fuel cells (PEMFC), as one promising type of fuel cells for automotive application, are known to be sensitive to the CO concentration in their hydrogen feed. CO concentration should be below 10 ppm for platinum anodes and below 100 ppm for CO-tolerant alloy anodes. One solution to provide hydrogen with high purity is to shift the reaction after reforming in order to convert the trace residual amounts of CO and produce highly purified hydrogen. Another simple and economical method is preferential CO oxidation in hydrogen rich streams. The task is here to find

catalysts that can operate at fuel cell operating temperature, between 80 to 100 °C and also to minimize hydrogen oxidation.

Gold nano-particles supported on ceria have been subject of many studies as a promising catalyst for PROX reaction since ceria can provide oxygen for CO oxidation and it can also stabilize small gold particles. Gold nano-particles are very active even at low temperatures and at those conditions they are more selective toward CO oxidation than hydrogen oxidation compared to platinum [156-159]. For example, Au supported on ceria doped with FeO_x and MnO_x showed good redox and catalytic properties [157]. Gold on FeO_x and MnO_x was also active towards preferential oxidation. It was suggested that the support structure, depending on the dopant nature and on the preparation method, determines the redox and catalytic properties of ceria.

All examples illustrated above had their primary application in the automotive industry, either down-stream for emission control or up-stream for power generation. However, application of redox properties of ceria is not restricted to the automotive industry. For instance, replacing alumina as a traditional support for cobalt based catalysts of the Fischer-Tropsch reaction with ceria increased the selectivity of these catalysts toward oxygenates especially linear alcohols [160].

2.3. Importance of the Three Phase Boundary for Ceria Catalysis

Ceria plays two major roles in catalysis: it releases and stores oxygen and it promotes dispersion and activity of another catalytic material. Both of these roles depend on the type, size, and distribution of defects on the ceria surface. Oxygen vacancies are the most

studied type of defects in ceria; however, other defects like metal substitution are also possible and important.

Ceria crystallizes in a cubic fluorite structure and the most thermodynamically stable low-index surface is (111) [161]. This surface has threefold coordinated oxygen atoms atop and sevenfold coordinated cerium atoms in the next layer. Non-polar stoichiometric O-Ce-O tri-layer repetition along the (111) direction represents a perfect CeO_2 (111) crystal. In its unreduced form, CeO_2 is an insulator with experimental band gap of 6.0 eV between O 2p and Ce 5d states and upon reduction the electron conductivity increases.

Surface oxygen vacancies can participate in chemical reactions. For example, oxidation of an adsorbent can occur by ceria surface oxygen, resulting in a surface oxygen vacancy. Adsorbates then bind to vacancies more strongly which may help in their dissociation [162]. Specifically in the WGS reaction which is the subject of this study, water is an oxidant and it can adsorb and dissociate on vacancy sites near metal particles and provide its OH group for further reactions [16, 19, 20, 23, 91, 163, 164].

Under ultrahigh vacuum conditions, on the slightly reduced surface, single vacancies are dominant and both surface and subsurface oxygen vacancies are present with similar coverages [165]. High temperature results in vacancy clustering with the formation of mainly linear surface vacancy clusters [165, 166]. The next most abundant shape of vacancy clusters is in the form of a triangle with three surface oxygen vacancies centered above subsurface oxygen [165]. Upon prolonged annealing, about 68% of all oxygen vacancies are in the form of linear vacancy clusters, 23% are single oxygen

vacancies, and about 2% are in form of triangles. One subsurface oxygen vacancy is required to nucleate each linear vacancy cluster [165, 166]. The most abundant oxygen vacancy clusters only expose Ce^{3+} ions to the gas phase as a very reactive site [165].

Presence of subsurface oxygen vacancy as a stabilizer for linear surface vacancy cluster can be a new explanation for the effect of dopants on ceria [165, 167]. For instance, it was mentioned before that one way to enhance oxygen storage capacity of ceria and also its thermal stability is to use Zr^{4+} ions as dopant [143-145, 168, 169]. In fact by using zirconia with less oxygen storage capacity, both oxygen storage capacity and thermal stability of the solid solution increases. One possible explanation is that these ions help linear vacancies to grow without the need for subsurface oxygen vacancies whose formation is more endothermic compared to surface oxygen vacancies. Besides, formation of subsurface oxygen vacancies results in considerable rearrangement in the lattice structure which may affect the stability of the catalyst.

Upon formation of oxygen vacancies, their mobility becomes another important phenomenon. Under ultrahigh vacuum condition, there is no diffusion of oxygen on a time scale of minutes even up to 400 °C [165, 170]. However, presence of even small amounts of adsorbates may make diffusion easier. Comparing the maximal rate of isotope exchange ($^{18}O_2$ with ^{16}O) for different oxides by means of the temperature programmed isotope exchange method, CeO_2 (410 °C) surpasses other oxides like ZrO_2 (530 °C) and γ-Al_2O_3 (620 °C) [171]. Presence of metals like rhodium considerably affects the oxygen exchange with the support. In fact, the maximum rate can be observed at about 200 to 300 °C lower temperatures for Rh supported oxides compared to bare oxides. Surface oxygen diffusion is much higher for ceria compared to other oxides. For instance, at 400

°C the relative mobility of surface oxygen on CeO_2 is about 280 times higher than γ-Al_2O_3 and 100 times higher than ZrO_2. Bulk oxygen diffusion can be observed above 400 °C for CeO_2, ZrO_2, and γ-Al_2O_3. The coefficient of bulk diffusion of oxygen in ZrO_2 is about two orders of magnitude higher than in γ-Al_2O_3 and ceria has a very high internal mobility. As a matter of comparison between pure ceria bulk oxygen diffusion and its solid solution with zirconia, temperature program reduction of the solid solution of 70 wt% ceria with 30 wt% zirconia showed a new peak between 100 and 200 °C which were not present for pure ceria [148, 149]. The new peak was related to the bulk oxygen diffusing to the surface. In the experiment, both solid solution and pure ceria were support of Pd nanoparticles.

Oxygen vacancies can alter the dispersion and activity of metal nanoparticles. For example, even though there are controversies whether the nucleation site for gold atoms is Ce vacancy or O vacancy [172, 173], the conventional view assumes the oxygen vacancy model [174]. So very small gold nanoparticles can nucleate into highly dispersed surface oxygen vacancies of ceria and provide more highly dispersed exposed gold atoms which are active [109]. The role of a structural promoter like alumina is then to provide highly dispersed ceria with more surface oxygen vacancies available for gold nucleation and also for redox cycles [137]. In fact, the addition of alumina by mechanochemical activation rather than co-precipitation resulted in less surface concentration of Ce^{3+} and while the first method produced highly active and stable gold catalysts the second was not found active toward the WSG reaction. It seems that metal barring could be responsible for less activity of the catalyst that was prepared by the co-precipitation method.

Along with oxygen vacancies, other defects like metal substitution in ceria are also important to provide highly active catalysts. For instance, recent findings revealed that active platinum and gold species for the low temperature WGS reaction are possibly highly dispersed positively charged ions [13]. This ionic state and the observed increase in the amount of surface oxygen lead the authors to conclude that the active metals could be the result of lattice substitution. In fact, this substitution must occur during the heating step of their preparation process since they found their sample to be much less active before heating. They further showed that by annealing the catalyst sample at high temperatures it becomes less active due to the loss of surface defects in ceria.

It is necessary to say that there is a mutual interaction between the ceria support and the metal catalyst. In other words, nature and morphology of the support will affect its interaction with the metal nanoparticles and the presence of metals alters the properties of the support. For instance, surface oxygen atoms in association with supported platinum atoms are more available for reduction compared to the pure ceria surface oxygen atoms. It is believed that these boundary sites are the active sites for the WGS reaction. In other words, while noble metals adsorb/activate CO, ceria's role is to activate water and the reaction occurs in the vicinity of the boundary sites.

It has recently been reported that in fact Ce ions are important to stabilize the active positively charged highly dispersed Pt sites and it is necessary that these active ions be surrounded by hydroxyl groups for the WGS reaction at low temperatures to proceed [175]. The authors tried both alumina and silica instead of ceria and they added small amounts of alkali ions (sodium or potassium) to activate the adsorbed platinum for the low temperature WGS reaction. They found that a partially oxidized Pt-alkali-

$O_x(OH)_y$ species are possibly the active sites for the reaction. In fact, they hypothesized that the presence of Pt makes oxygen in direct contact with the metal and alkali ions become "reducible" even at low temperatures. It is worth mentioning here that, it is possible to produce highly dispersed positively charged Pt ions on surfaces. For example, for γ-Al_2O_3 supported Pt, this can be done by utilizing under-coordinate Al^{+3} sites of γ-Al_2O_3 as binding site for Pt atoms [176]. However, controlling the dispersion and morphology of metal particles is still a challenge due to the lack of technology to systematically control the number density of Al^{3+} sites.

To further reinforce the importance of the boundary sites of ceria supported noble metals for the low temperature WGS reaction it is noted that the reaction rate scales linearly with the total length of the boundary [93, 97, 98]. Besides nearly metal free ceria catalysts and inversely supported CeO_x nanoparticles grown on Au (111) surface showed significant activity for the WGS reaction [13, 21, 99, 102].

The origin of this activity, however, is still ambiguous due to inter-related interactions between metal particles, support, and the gas phase environment [13, 177]. Interestingly, it has been found that the alkali promoted platinum catalysts on alumina or silica have quite the same apparent activation energy, 70±5 kJ/mol, as other Pt based catalysts for the WGS reaction; such as, Pt-CeO_2, Pt-TiO_2, Pt-Al_2O_3, Pt-ZrO_2, irrespective of the support (although these catalysts have different activity at different temperatures) [175]. Considering the importance of the oxygen containing (OH) groups in the vicinity of Pt atoms, the role of the support may be restricted to stabilizing the active Pt sites, partially oxidized Pt-M-$O_x(OH)_y$, in the reaction environment.

Another interesting finding is related to the core-shell Pt-ceria catalysts [128]. The authors reported that a bimetallic core of Pt and Au with 1:1 ratio at about 5 wt% of ceria shell, shows a high WGS activity, higher than Pt with 5 wt% of ceria. They found their catalysts to be unselective toward methane formation at even higher temperatures and noticed that doping of rare earth metal ions to the ceria coat did not result in any higher activity. This suggests that the overall catalytic activity of these types of catalysts depends on the electronic aspects of the metal-ceria interface and the importance of oxygen mobility and storage capacity of the promoted ceria shell does not play a significant role. They further mentioned that pure gold in the shell is probably inactive toward the WGS reaction. Considering that both ionic gold and platinum on ceria are active toward the WGS reaction, they mentioned that the reaction mechanism for these two metals is probably different.

In fact, understanding the real mechanism of reactions over different catalysts and finding the origin of activity and selectivity of different catalysts for different possible reactions can probably only be done with the help of theoretical investigations [178]. An appropriate theory helps to analyze data from different experiments. For example, simple experiments show that for transition metals there is a trend in their reactivity; bond strengths of an adsorbed atom generally increase from the right to the left of the periodic table. More advanced surface science experiments show that surface defects like steps and kinks of transition metals are more reactive.

Using theoretical tools like density functional theory (DFT), it is possible to rationalize these experimental findings. In other words, by means of DFT calculations it is possible to calculate the electronic structure of the surface. By further analyzing the

electronic structure it can be seen that when a “quantity” like the d band center is closer to another quantity like the “Fermi level” then the adsorption energy of that transition metal is higher. Furthermore, for steps and kinks of transition metals the d band center is closer to the Fermi level and also moving from the right to the left of the periodic table, the d band center gets closer to the Fermi level. Indeed, by analyzing more experimental data, it is possible to find a more physical interpretation for these “quantities”. Interestingly, if by any means we would be able to move the d band center of the metal closer to the Fermi level then we made it more reactive (possibly also for a poison).

For real catalysts, however, there are many elementary processes in addition to simple adsorption: dissociation of reactants from the gas phase, diffusion of surface species, surface reactions to form intermediates and products, and desorption of products to the gas phase. Even though with the development of more surface sensitive spectroscopic techniques it is possible to observe catalytic surface reactions in more detail, there is a limitation in spatial, temporal, and energy resolution of any experimental technique [179]. Theoretical calculations let us postulate a reaction mechanism; and by means of microkinetic modeling it is possible to predict more details about the reaction, like the surface species’ coverages and apparent activation energy. Then the validity of the mechanism can be checked by the available experimental data.

In fact, reaction mechanisms help us to understand which elementary steps are the most important one in order to make the catalyst more active and selective. If we would know the exact origin of activity of different steps it could be possible to alter the properties of catalysts in such a way to make them more active and selective. However, the main problem is that “quantities” that may increase the activity of the catalyst toward

one particular step usually increases the activity of the other steps as well. Considering a complex reaction mechanism that involves, for example for the WGS reaction, there may be many steps that control the activity and selectivity of the catalyst. Then the concept of the three phase boundary (TPB) potentially can provide us with more "independent quantities", in order to find a better catalyst for the reaction at different conditions [178, 180].

2.4. Overview of Theoretical Studies of Ceria Catalysts

In a wide variety of applications that have been mentioned for ceria till now, it can basically play two roles to provide a highly active catalyst: it can release and store oxygen and it can promote dispersion and activity of another catalytic material. However, under what conditions which of these roles are dominant is the subject of discussion in this section. Indeed, experiments can provide a good insight. For instance, it has been observed experimentally that for transition metals steps and kinks are more reactive. In other words, for simple CO or H_2 adsorption, molecules interaction with steps and kinks is higher compared to flat traces [178]. Since metal nanoparticles can provide more low coordinated sites like kinks and corners compared to larger particles, they are more reactive.

However, using porous supports as media for metal nanoparticles to provide high dispersion for them, not all supports are inert. For instance, again for the simple CO or H_2 adsorption, it was observed that even though noble metals were completely dispersed on titania, they showed less chemisorption for CO and H_2 after reduction of the material at 500 °C compared to reduction at 200 °C [181]. It was concluded that "strong metal-support interaction had somehow deprived these metals of one of their most characteristic properties [182]." Spectroscopic data also showed a direct interaction between metal atoms

and reduced titanium ions. These observations and also other observations like the tendency of many metal-oxide systems to increase their interfacial area even at the expense of breaking other strong bonds in order to merge phases, led to the conclusion that there is an interfacial bonding interaction between metal particles and reduced titania which can be generalized to other metal oxides such as ceria or even alumina provided that the surface is reducible. Indeed, upon bond formation the electronic structure, geometry, and other properties of the system would change compared to either the metal or metal oxide alone.

Utilizing theoretical or in other words first principle computational studies, the aim is to estimate the electronic structure of the system accurate enough to provide a good estimation of other properties of the system like bond dissociation energies or activation barriers. After that, it will be possible to understand the real mechanism behind the reaction and find the exact role that each of the involved phases play in making a site active. Along with accuracy, affordability of computational methods is also very important.

One of the most widely used theories for studying the electronic structure of materials is density functional theory (DFT). Based on this theory, it is not necessary to describe the interacting electrons with a multi-dimensional wave-function. Instead, the formulation is based on a simple three-dimensional electron density to fully describe the electronic structure. However, in order to know how nuclei will affect the electron density it is necessary to utilize exchange correlation functionals. In fact, the most important part in the application of DFT is to find an appropriate functional from many that are available; for example, Local Density Approximation (LDA), Generalized

Gradient Approximation (GGA) such as PBE or PW91, and also another class of functionals which are called Hybrid Functionals (HF), for example HSE, PBE0, or B3LYP.

It is known that typical DFT functionals, LDA and GGA, underestimate the band gap of materials and also barriers of chemical reactions [183]. They also cannot give accurate interaction energies in strongly correlated oxides and band dissociation energies of transition metal dimers which have degenerate or near degenerate states. Strongly correlated materials like Fe_2O_3 or CeO_{2-x} typically have partially filled d or f electron shells and show unusual electronic and magnetic properties, such as metal-insulator transitions or half-metallicity. For instance, upon formation of one oxygen vacancy on a fully oxidized ceria surface, it is generally believed that the two left over electrons will localize on two near vacancy Ce ions to reduce them from Ce^{+4} into Ce^{+3} , i.e., the electrons will partially occupy 4f states. However, both LDA and GGA fail to localize electrons and they delocalize them over the whole surface. Consequently, these two methods underestimate the band gap of the reduced ceria and predict a metallic behavior which is wrong.

To accurately describe the electronic structure of strongly correlated materials and consequently their properties, mainly two approches have been considered: Hybrid Functionals and DFT+U. Hybrid functionals add a certain percentage of Hartree-Fock exchange to the traditional exchange, GGA, in order to correct the delocalization error. For instance, they can partly localize electrons and remove the delocalization error of reduced ceria. However, these functionals are less accurate compared to pure functionals

for metal surfaces. The other approach to correct the electronic structure of strongly correlated systems is via the U parameter.

U parameter or Hubbard parameter is in fact an attraction term to correct the strong on-site Coulomb repulsion among localized f or d electrons in traditional DFT exchange functionals, LDA and GGA. By choosing an appropriate value for the U parameter it is possible to localize electrons. However, the choice of the value is empirical and it depends on the property of interest, the functional, and also the system [184-190]. For instance, the value for correcting the band gap of fully reduced ceria is different for GGA and LDA functionals and these values cannot be used for other reduced transition metal oxides. Besides, there is no guarantee that these best values will also be the best for other properties such as the lattice parameter. However, using a U parameter proved to be a more practical way to improve the electronic structure of cerium oxides since hybrid functionals are very computationally expensive in case that the solid surface is being modeled by the conventional periodic boundary slab model approach.

Even though the slab model approach for modeling a solid surface is a very traditional and efficient way due to periodic boundary conditions, the unit cell should be large enough for defective surfaces or surfaces with metal clusters and adsorbents to minimize their artificial interactions with their images caused by periodicity. The other modeling approach for solid surfaces is based on cluster embedding which let us model an infinite dilution of defects or any other active sites on the surface [191-194].

For instance, the periodic electrostatic embedding approach considers electronic embedding of a finite quantum mechanical cluster in a periodic infinite array of point

charges. In other words, an ionic cluster in a two dimensional slab would be treated quantum mechanically while all the other atoms in the infinite slab will interact with that ionic cluster just via their electrostatic potential. Using this method, it would be possible to provide a correct Madelung potential for the system. In fact, approximating a single ion in an ionic solid by a point charge, the Madelung constant is useful to determine the electrostatic potential of that ion. By choosing an appropriate quantum cluster model it would be possible to model different surfaces either with defects or metal clusters.

It is worth mentioning that in order to bridge the gap in temperature and pressure of real reactions with DFT based theoretical studies, we used transition state theory to calculate elementary reactions' rate constants and performed a microkinetic analysis to study the interplay of various elementary reactions. However, there are other methods based on both quantum mechanics and molecular dynamics in order to model the dynamic behavior of all atoms at finite temperatures [195-198]. These methods are computationally very expensive compared to microkinetic modeling. Assuming that the morphology of the active site will not change due to the reaction conditions, microkinetic modeling can provide us with very useful information like surface species' coverages and the apparent activation energy that can be compared with the experimental data.

There are many reports published related to theoretical studies of ceria systems either with vacancies or with adsorbed metal clusters or other adsorbents. In the following some of the most interesting ones for this study will be discussed briefly.

Considering fully oxidized and fully reduced cerium oxides, CeO_2 and Ce_2O_3, many efforts have been devoted to evaluate different DFT based functionals for

describing the electronic structure and other properties of these oxides. For instance, Kullgren et al. tried different functionals, namely B3LYP, PBE0, LDA, GGA, LDA+U and GGA+U [184]. They found the B3LYP functional to be slightly better than the PBE0 functional for describing electronic properties such as the band gap and a little worse for structural properties such as cell parameters. However, LDA+U with U = 6 eV and GGA(PBE)+U with U = 5 eV were better compared to both hybrid functionals PBE0 and B3LYP.

Da Silva et al. also found GGA(PBE)+U to be better than hybrid functionals such as HSE0 and PBE0 [190]. However, they showed that the best U parameter is property dependent. For instance, U = 3.25 eV in LDA+U resulted in correct reduction energy, while it did not give a good result for the band gap and lattice parameter of Ce_2O_3. They suggested that for GGA(PBE), U ≈ 2.0 eV would give the overall best description for energetics, lattice parameter, and magnetic ordering in Ce_2O_3. For LDA they suggested U to be between 3 and 4 eV. It is worth saying that even for the same property of the same material different reports suggested different "best" values for the U parameter. It seems that other computational settings are also important.

Another topic of interest in many studies is the oxygen vacancy formation on the CeO_2 (111) surface as it is known to be thermodynamically more stable compared to other low index surfaces. Ganduglia-Pirovano et al. tried HSE06, LDA+U with U = 5.3 eV, and GGA(PBE)+U with U = 4.5 eV functionals and found that with 0.25 monolayer of defects, subsurface oxygen vacancies are more stable compared to surface oxygen vacancies even though the value of stability was quantitatively different between different functionals [199]. They also found electrons to become localized on the next

nearest neighbor Ce ions instead of the general believe for localization of electrons on the nearest neighbor Ce ions. Burow et al. used the periodic electrostatic embedded cluster approach with PBE0 functional and found that the electrons were localized on near vacancy Ce ions [193]. It seems that, as suggested by Ganduglia-Pirovano et al., structural relaxation is very crucial in finding the most stable configuration and also to get correct electron localization. In fact, localization of electrons on nearest neighbor Ce ions may correspond to delocalization of electrons on all of them.

Even though the (111) surface is thermodynamically more stable compared to (110) and (100) surfaces, the (110) surface has been suggested to be more reactive for example toward CO oxidation [200]. Indeed, oxygen vacancy formation and CO adsorption on (110) and (100) surfaces have also been studied both with slab model and embedded cluster approaches [191, 194, 200-202]. For instance, it has been suggested that the (110) surface oxygen vacancy is more stable compared to the bulk vacancy and (111) surface vacancy. Also, upon CO adsorption, on the (110) surface carbonate complexes may form [194, 202], while theoretical calculations suggest that the fully oxidized (111) surface interaction with CO is just physisorption [202].

Considering the wide application of ceria supported metals in catalysis, many studies are trying to find the interaction between metals, either a single atom or a cluster, with ceria supports, either fully oxidized or partially reduced. Yang et al. used GGA(PBE)+U with U = 5.0 eV to study single platinum adsorption on fully oxidized and partially reduced ceria (111) surfaces [203]. On a fully oxidized surface, the bridging site between two surface oxygens was the most stable site for Pt adsorption while on reduced surfaces vacancy sites were the most stable adsorption sites. Adsorption on reduced

surfaces was stronger than adsorption on the oxidized surface. They observed a strong metal support interaction between Pt adatoms and the surfaces and the formation of Pt-O-Ce bonds was found possible. The lower lying metal induced gap states, mainly from Pt 4d states, made the ceria surface more reducible. In another words, it was easier to form an oxygen vacancy on the Pt adsorbed oxidized surface compared to the pure oxidized surface since the metal induced gap state could help accommodating left over electrons after reduction. For clean surfaces these electrons localize on 4f states on reduced Ce ions. Removing different surface oxygens in the vicinity of Pt required between 1.06 to 0.36 eV less energy compared to a clean surface with the vacancy formation energy of 2.89 eV. In fact, the vacancy formation energy of surface oxygens far away from Pt adatoms was quite similar to the pure surface illustrating that there was a metal-oxide interaction which improved the reducibility of the oxide.

Next, Lu and Yang showed that Ce ions become reduced upon adsorption of Pt atoms on fully oxidized surfaces [204]. They studied the adsorption of single Pd, Pt, and Rh atoms and their tetrahedral clusters on the CeO_2 (111) surface with the GGA(PBE)+U with U = 5 eV methodology. Single Pt atoms had a partial positive charge upon adsorption and for tetrahedral clusters the three base atoms had a positive charge while the top atom had a slightly negative charge. Upon adsorption of a single atom, the electrons became localized on the next nearest neighbor Ce ions to reduce it from Ce^{+4} into Ce^{+3}. The authors further explained that their previous work was corresponding to a metastable state with a little different geometry; for example, longer metal-O distances and shorter metal-Ce distances. Comparing different metals, Rh adsorption was stronger, followed by Pt and then Pd. While Pt and Pd adatoms preferred the bridge site between

two oxygens for adsorption, Rh preferred the hollow site between three surface oxygen atoms.

To clarify the oxidation state of adsorbed Pt on CeO_2 (111) surface, Bruix et al. used LDA+U with U = 5 eV, GGA(PW91)+U with U = 3 eV, and also the HSE06 hybrid functional [205]. They tested the singlet state with no unpaired electrons and triplet state with two unpaired electrons and found that the singlet state is a little more stable. While the Pt charge for the singlet state was almost neutral, the triplet state resulted in oxidized Pt and reduced Ce atoms. They emphasized that small energy difference may provide a spontaneous charge transfer even at room temperature. Studying Pt diffusion over the surface, they found the energy barrier to be small. In other words, adsorbed Pt atoms could easily nucleate to form larger clusters.

Indeed, nucleation or in another words agglomeration of metal nanoparticles is an important phenomenon during both the reaction and preparation. Li et al. studied Rh and Pd agglomeration over the CeO_2 (111) surface by means of GGA(PBE)+U with U = 5 eV and also molecular dynamics simulations [206]. They found that single particles tend to form three dimensional clusters on the surface due to the strong cohesion energy. Pd showed greater tendency for agglomeration compared to Rh. Using molecular dynamics simulations, they found that the oxidation state of Rh atoms play an important role in the morphology of particles on the support surface. While under oxidizing condition strong O-Rh-O inhibited Rh agglomeration, removal of surface O atoms from oxidized Rh caused subsequent metal particle agglomeration.

Mayernick and Janik, however, used the *ab initio* thermodynamics approach to study the effect of a gas phase environment on the morphology, oxidation state, and agglomeration of catalysts [207]. They studied single Pd atoms on CeO_2 (111), (110), and (100) surfaces and noticed that Pd atoms could substitute lattice Ce atoms on the CeO_2 (111) surface with +4 oxidation state. Then upon oxygen vacancy formation near Pd, it was possible to reduce its oxidation state to +2 or zero. They used GGA(PW91)+U with U = 5 eV to find the electronic energies. The *ab initio* thermodynamics approach was then used to find the Gibbs free energies of different reactions in order to find the most stable surfaces at different temperatures and partial pressures of oxygen. For instance, they found that at room temperature and oxygen partial pressure higher than 10^{-10} atm, adsorbed Pd atoms incorporate into the ceria (111) surface to form a mixed oxide.

In order to show the effect of support on CO adsorption, Jung et al. considered Pt_4 and Pd_4 clusters over c-ZrO_2 (111) and CeO_2 (111) surfaces [208]. They found that the support changes the site preference for the CO adsorption. For instance, while CO molecules preferred to adsorb on atop sites of isolated Pt_4 clusters, adsorption on the bridge site of supported clusters had the highest energy compared to other sites. They found clusters to be positively charged yet they still could donate electrons in order to activate adsorbed CO molecules.

Studying CO adsorption and the WGS reaction over ceria supported gold, Liu et al. used the GGA(PBE) functional without U parameter and showed that due to the presence of empty localized non-bonding f states of ceria, gold can become oxidized facilitating CO adsorption [209]. They attributed the localized f states to an electron reservoir like delocalized Fermi-level states in metallic materials, able to accept or donate

electrons. While individual gold atoms adsorbed on vacancy sites were not active toward CO adsorption due to its large negative charge, they found that 4 to 6 gold atoms clustering on an oxygen vacancy can provide partially oxidized gold atoms to be active toward CO adsorption. In order to relate the activity of oxidized gold toward CO adsorption to the activity toward the WGS reaction, they proposed a reaction mechanism via formate intermediate and found a maximum barrier related to CO_2 desorption from formate by 1.08 eV. Nevertheless the exact origin of the activity is still controversial [109, 209].

It is worth mentioning that Liu et al. did not use U parameter since in their calculations (using CASTEP) individual f orbitals never had more than one electron leading to insulating behavior for both CeO_2 and Ce_2O_3 surfaces. While they found individual gold adatoms on the fully oxidized surface to be positively charged, recent work by Branda at al. shows that the oxidation state of single Au on CeO_2 (111) surface cannot be definitely determined by theoretical methods [210]. They used the HSE06 hybrid functional and the LDA+U and GGA+U methods with different U values, namely 0, 3, and 5 eV, and showed that the oxidation state of gold is very sensitive to the method and the surface model. In some cases they found two very close energy systems but with different electronic structures, one with neutral Au and the other with oxidized Au. The energy difference usually was small and within the accuracy of the DFT methods.

To conclude, even though theoretical methods can provide more understanding about the catalytic surfaces and their origin of activity, along with affordability there are also some limitations in their accuracy. Indeed, by using experimental data at different

levels and appropriate theoretical calculations and multi-scale modeling, one can gain more insight about the exact role of each of the involved phases during the reaction.

3. Computational Method

3.1. Periodic DFT Calculations

The slab model approach has been utilized to model the Pt/CeO_2 (111) catalyst surface using the Vienna Ab-initio Simulation Package (VASP). To describe the effect of the core electrons on the valance electrons the projected augmented wave method has been used. The Ce 5s, 5p, 5d, 4f, and 6s electrons; the O 2s, 2p electrons; the C 2s, 2p electrons; the H 1s electron; and the Pt 5d, 6s electrons were treated explicitly with a plane wave energy cutoff of 500 eV.

Electron exchange correlation was described with the Perdew-Burke-Ernzerhof (PBE) functional. A Hubbard, U-J, parameter has been employed to be able to describe the strongly correlated 4f electrons of reduced ceria. While in the rotationally invariant GGA+U approach, two parameters, U and J enter into the density functional formulation that should be specified explicitly [211], the formulation in the simplified spherically averaged version is based on one effective interaction parameter [212], U-J. Here we used U-J equal to 5 eV as suggested by Nolan et al. [201]; as U = 5 eV was high enough to give a localized electronic structure in agreement with earlier studies [213].

An optimized bulk CeO_2 with 5.48 Å lattice parameter was used to construct the (111) surface. A p(4 × 4) unit cell with nine atomic layers and 15 Å vacuum gap was used for all surface calculations. While the bottom three atomic layers were fixed in their bulk position, all the other atoms were relaxed until the forces were smaller than 0.05

eV/Å. For this model, we find that the surface oxygen vacancy formation energies and Pt adsorption energies described in the next section are converged to within 0.05 eV with respect to increasing the number of layers from 9 to 15 and 18. The Hellmann-Feynman theorem is used for calculating the forces at the end of each self-consistent field calculation and the Harris-Foulkes correction is added to the forces [214, 215]. Brillouin zone sampling was performed with 2 × 2 × 1 Monkhorst-Pack k-point mesh. Calculations were spin polarized with dipole and quadrupole corrections to the energy solely in the surface normal direction. Fractional occupancies of bands were allowed using the Gaussian smearing method with sigma value equal to 0.1 eV. For gas phase species and isolated metal clusters, gamma point calculations were performed within a 15 Å cubic box and Gaussian smearing of 0.1 eV.

For the mechanistic study we used this set up for all calculations except that we used gamma point calculations instead of a 2 × 2 × 1 Monkhorst-Pack k-point mesh to reduce the expense of the transition state search calculations. The transition states of the elementary steps were found via the CI-NEB and Dimer methods.[216, 217]

3.2. Effect of Platinum Cluster Size on Reducibility of the Ceria (111) Surface

Since ceria is well-known for its oxygen storage capacity and its ability to undergo rapid redox cycles by releasing and storing oxygen atoms, and also since it is known that the reducibility of the ceria surface increases in the presence of Pt atoms, we studied the effect of small platinum clusters on the reducibility of the ceria (111) surface. For each size, we identified the most stable configurations of the clusters on both the stoichiometric and partially reduced ceria surfaces with 0.063 monolayer oxygen

vacancy. We added one, two, and three Pt atoms at the same time to the most stable or otherwise representative (already optimized) smaller cluster structure to ensure that many different initial configurations for each Pt cluster size have been studied in the search for the lowest energy structures. Next, we used the energy of those final structures to calculate the oxygen vacancy formation energies in the presence of a Pt_n cluster on the surface:

$$E^{vf}_{Pt_n} = E_{Pt_n...CeO_{2-x}} + 0.5E_{O_2} - E_{Pt_n...CeO_2} \quad (3\text{-}1)$$

where E denotes the DFT energies of the related species and subscript n refers to the number of platinum atoms in the clusters. In order to avoid the errors associated with DFT methods for describing a triplet state of the gas-phase oxygen molecule, the O_2 energy is obtained using the H_2O splitting reaction with the experimental reaction energy and calculated DFT-GGA energies of H_2 and H_2O in the gas phase [192]:

$$E^{elec}_{O_2} = 2\left[\left(E^{elec}_{H_2O} + E^{zpe}_{H_2O}\right) - \left(E^{elec}_{H_2} + E^{zpe}_{H_2}\right) - E_{hof}\right] - E^{zpe}_{O_2} \quad (3\text{-}2)$$

where E_{hof} is the experimental heat of formation of a gas phase H_2O molecule. E^{zpe} and E^{elec} denote the experimental zero point energy and the calculated DFT energy of the related molecules. The E^{zpe} values of H_2O, H_2, and O_2 are 0.558, 0.273, and 0.098 eV; and E_{hof} is equal to -2.505 eV. We note that such a correction increases the energy of the oxygen molecule by about 0.4 eV and will thus have a significant effect on all reaction energies involving the O_2 molecule. Next, it is worth noticing that, for the largest Pt cluster that we studied (Pt_{10}), the distance between cluster images is more than 10 Å so that cluster−cluster interactions are negligible. Also, by using the most stable

stoichiometric and reduced structures, we assume that the surface is able to equilibrate fast.

Next, we calculated the clustering energies (E^{clu}) of the metal atoms on the surfaces by using the energies of the most stable configurations of Pt clusters on stoichiometric and partially reduced ceria:

$$E^{clu}_{Pt_n,CeO_2} = \frac{1}{n} \times \left(E_{Pt_n/CeO_2} - E_{CeO_2} - nE_{Pt} \right) \quad (3\text{-}3)$$

$$E^{clu}_{Pt_n,CeO_{2-x}} = \frac{1}{n} \times \left(E_{Pt_n/CeO_{2-x}} - E_{CeO_{2-x}} - nE_{Pt} \right) \quad (3\text{-}4)$$

3.3. Catalyst Model Identification via the Constrained Ab Initio Thermodynamics Calculations

Under finite temperature and pressure conditions, the stable surface structure is a result of the statistical average of all the involved elementary reactions. One rigorous yet time demanding approach to find the dynamic behavior of the surface is via kinetic Monte Carlo simulations which are able to give details about correlations and distributions of the intermediates on the surface under steady state conditions [218, 219]. In this approach it is necessary to have a reaction mechanism and all rate constants at hand. However, without knowing the kinetics of the elementary reactions it is still possible to find the relative stability of different surface species under specific gas phase conditions via the constrained ab initio thermodynamic approach [172, 207]. In this study, we performed constrained *ab initio* thermodynamic calculations to understand the effect of a gas phase environment on the stability of various catalytic sites.

The constrained *ab initio* thermodynamic approach considers a solid surface in equilibrium with a gas phase environment and assumes there is enough gas and bulk solid where both can be treated like a reservoir at a specified temperature and pressure, and they are able to exchange atoms with each other [220-222]. Considering the experimental conditions, the appropriate thermodynamic potential to study the system is the Gibbs free energy. Then in order to compare the stability of two surface structures under specified conditions a reaction such as equation (3-5) can be written:

$$A_{solid} + B_{gas} \rightarrow C_{solid} + D_{gas} \quad (3\text{-}5)$$

For instance, in a gas environment of CO and CO_2, the relative stability of a fully oxidized surface with respect to a partially reduced surface can be evaluated by the following reaction:

$$CeO_{2,solid} + CO_{gas} \rightarrow CeO_{2-x,solid} + CO_{2,gas} \quad (3\text{-}6)$$

which is assumed to be in equilibrium.

In order to find the relative stability of species A and C under the gas phase condition exerted by B and D, the Gibbs free energy of the reaction (3-5) under a specified temperature and pressure can be calculated. A negative Gibbs free energy means that the reaction is thermodynamically possible and the products are more stable than the reactants. In other words, the surface C structure is more stable than the surface A structure. On the other hand, a positive Gibbs free energy means that the reverse reaction is thermodynamically preferred and the reactants are more stable than the products; then, the surface A structure is more stable than the surface C structure.

The Gibbs free energy of a solid surface like A can be written as:

$$\Omega_A = E_{A,elec} + \Delta G_A{}^{vib} - \sum N_{i,A}\hat{\mu}_i \qquad (3\text{-}7)$$

where $E_{A,elec}$ is the self consistent field energy of the solid surface, $\Delta G_A{}^{vib}$ is the vibrational contribution to the Gibbs free energy (including zero point energy), $N_{i,A}$ is the number of atoms i in the slab and $\hat{\mu}_i$ refers to the chemical potential of atom i in the slab [221]. The rotational and translational contribution to the Gibbs free energy of the solid surface is assumed to be zero.

For gas phase species such as B, the Gibbs free energy can be written as:

$$\mu_B = E_{B,elec} + \Delta G_B{}^{vib} + \Delta G_B{}^{rot} + \Delta G_B{}^{trans} - \sum N_{i,B}\hat{\mu}_i + k_B T \ln\left(\frac{P_B}{P^0}\right) \qquad (3\text{-}8)$$

where $\Delta G_B{}^{rot}$ and $\Delta G_B{}^{trans}$ refer to the rotational and translational contribution to the Gibbs free energy, k_B is the Boltzmann constant, P^0 is the reference pressure, P_B is the partial pressure of B, and definitions of the other terms are the same as for the solid surface.

Having expressions for the Gibbs free energy of the species in the reaction (3-5), it is possible to calculate the Gibbs free energy of reaction to find the relative stabilities of surface structures A and C,

$$\Delta G_r = \sum_{products} G - \sum_{reactants} G = \Omega_C - \Omega_A + \mu_D - \mu_B \qquad (3\text{-}9)$$

Replacing the expressions for the Gibbs free energies of surfaces and gas phase species will give

$$\Delta G_r = \Delta_r(E_{elec}) + \Delta_r(\Delta G^{vib}) + \Delta_r(\Delta G^{rot}) + \Delta_r(\Delta G^{trans}) - \sum \Delta_r(N_i)\hat{\mu}_i + k_B T \ln\left(\frac{P_D}{P_B}\right) \quad (3\text{-}10)$$

where

$$\Delta_r(X) \equiv X_C - X_A + X_D - X_B$$

Due to the atomic balance in the reaction, $\Delta_r(N_i)$ is zero for each atom type and the formulation will reduce to

$$\Delta G_r = \Delta_r(E_{elec}) + \Delta_r(\Delta G^{vib}) + \Delta_r(\Delta G^{rot}) + \Delta_r(\Delta G^{trans}) + k_B T \ln\left(\frac{P_D}{P_B}\right) \quad (3\text{-}11)$$

Considering that most of the times the vibrational contribution to the Gibbs free energy of the solid surface is negligible compared to other terms [220], the three $\Delta_r(\Delta G^{vib})$, $\Delta_r(\Delta G^{rot})$, and $\Delta_r(\Delta G^{trans})$ terms are dominated by the gas phase species and are often recombined as $\Delta\mu_D{}^0 - \Delta\mu_B{}^0$ and evaluated at the reference pressure and reaction temperature. All the temperature and pressure dependency then lies in $(\Delta\mu_D - \Delta\mu_B) \equiv (\Delta\mu_D{}^0 - \Delta\mu_B{}^0) + k_B T \ln\left(\frac{P_D}{P_B}\right)$ which can be evaluated by standard statistical mechanics calculations or by using thermodynamic tables and relations [221, 223]. In this study we used the former method via the TURBOMOLE program package.

3.4. Calculation of the Langmuir Adsorption Isotherms

Competitive adsorption of several species from the gas phase on a surface site can be calculated using the Langmuir adsorption isotherms. The Langmuir adsorption equation relates the coverage or amount of adsorption of molecules on a surface to the gas pressure. Here, the adsorbed species have no interaction with each other and no reaction occurs between them. Also, the adsorption and desorption processes are fast and consequently at equilibrium. For example, for competitive adsorption of two species, A and B, on a surface site, *, we have:

$$A + * \rightarrow A* \qquad , B + * \rightarrow B* \tag{3-12}$$

$$K_A = \frac{\theta_A}{\theta_* P_A} \qquad , K_B = \frac{\theta_B}{\theta_* P_B} \qquad , K_i = e^{\frac{-\Delta G_i}{k_B T}} \tag{3-13}$$

$$\Rightarrow \quad \theta_A = K_A P_A \theta_* \qquad , \theta_B = K_B P_B \theta_* \tag{3-14}$$

$$\theta_A + \theta_B + \theta_* = 1 \tag{3-15}$$

$$\Rightarrow \quad \theta_* = \frac{1}{K_A P_A + K_B P_B + 1} \tag{3-16}$$

$$\Rightarrow \quad \theta_A = \frac{K_A P_A}{K_A P_A + K_B P_B + 1} \qquad , \theta_B = \frac{K_B P_B}{K_A P_A + K_B P_B + 1} \tag{3-17}$$

Here, ΔG_i is the Gibbs free energy of the adsorption of specie i on the surface site that can be calculated as a function of temperature at a reference pressure. Θ_i is the surface coverage of specie i and θ_* is the free site coverage. P_i is the partial pressure for i in the gas phase; while k_B is the Boltzmann constant and T is the absolute temperature.

3.5. Mechanistic Study via Microkinetic Modeling

For DFT calculations for the mechanistic study we used the same computational set up as has been described in section 3.1. However, due to the expense of the calculations, specifically for transition state search algorithms, we used gamma point calculations instead of sampling the Brillouin zone with 2 × 2 × 1 Monkhorst-Pack k-point mesh. The transition state of each elementary step was found via the CI-NEB and Dimer methods [216, 217].

After finding the energies of intermediates and transition states for each designated pathway, we used transition state theory to find the forward and reverse rate constants. For a surface reaction, A*→B*, the forward and reverse rate constants can be calculated as:

$$k_{for} = A_{for} e^{\frac{-E^{a}_{for}}{k_B T}} \quad , k_{rev} = A_{rev} e^{\frac{-E^{a}_{rev}}{k_B T}} \tag{3-18}$$

where E^{a}_{for} and E^{a}_{rev} corresponds to the zero-point corrected forward and reverse activation barriers, respectively; while k_B is the Boltzmann constant and T is the absolute temperature. The frequency factors (A) are calculated from the vibrational partition functions (q_{vib}) using the following expressions:

$$A_{for} = \frac{k_B T}{h} \frac{q_{TS,\,vib}}{q_{A^*,\,vib}} \quad , A_{rev} = \frac{k_B T}{h} \frac{q_{TS,\,vib}}{q_{B^*,\,vib}} \tag{3-19}$$

Here, h is the Planck's constant. The vibrational partition function can be calculated from the frequencies (υ_i) as follows:

$$q_{vib} = \prod_i \frac{1}{1 - e^{\frac{-h\upsilon_i}{k_B T}}} \tag{3-20}$$

For an adsorption reaction, A+*→A*, we used collision theory to calculate forward rate constant:

$$k_{for} = \frac{10^5}{\sqrt{2\pi m_A k_B T}} S_{unit} \tag{3-21}$$

Here, k_{for} has the unit of $s^{-1}\,bar^{-1}$. S_{unit} is the surface area per active site which is 8.19×10^{-19} m^2 for our model and m_A is the molecular weight of specie A in kg. The reverse rate constant can be calculated from the calculated equilibrium constant (K) and the k_{for} as follows:

$$K = \frac{q_{A*}}{q_A q_*} e^{\frac{-\Delta E}{k_B T}} \qquad , k_{rev} = \frac{k_{for}}{K} \tag{3-22}$$

where ΔE is the zero-point corrected adsorption energy.

For all hydrogen transfer processes, we considered the hydrogen tunneling correction. The corrected forward and reverse rate constants are the results of multiplication of the transmission coefficient for tunneling, κ, with the uncorrected rate constants. κ can be approximated by the following equation:

$$\kappa(T) = 1 + \frac{1}{24}\left(\frac{h\upsilon_c}{k_B T}\right)^2 \left(1 + \frac{k_B T}{E^{TS}}\right) \tag{3-23}$$

where υ_c and E^{TS} are the curvature of the barrier and the energy of the barrier, respectively. After finding the forward and reverse rate constants, for each pathway we assumed a linear reaction set and applied a pseudo-steady-state approximation for surface species and solved a set of linear equations to find the coverage of each species and the empty site. For clarity, some of the elementary reactions in this work are represented with multiple species. The surface coverages are used to find the rate (turn over frequency) of each pathway. The apparent activation energy is calculated over the temperature range of 373-573 K using the following equation:

$$E^{app} = RT^2\left(\frac{\partial \ln \Re}{\partial T}\right)_{p_i} \tag{3-24}$$

Here, $\Re$ is the rate of the WGS cycle and p_i is the partial pressure of the gas phase specie i in the reaction mixture. The reaction orders are calculated as follows:

$$n_i = \left(\frac{\partial \ln \Re}{\partial \ln p_i}\right)_{T,p_{j\neq i}} \tag{3-25}$$

For further analysis, we calculated Campbell's degree of rate control and degree of thermodynamics rate control to gain insight about the most important elementary step and reaction intermediate of each pathway [224]. The equations that we used are:

$$X_{RC,i} = \frac{k_i}{\Re}\left(\frac{\partial \Re}{\partial k_i}\right)_{K_i,k_{j\neq i}} \tag{3-26}$$

$$X_{TRC,n} = \frac{k_l}{\Re}\left(\frac{\partial \Re}{\partial k_l}\right)_{k_{p\neq l}} \tag{3-27}$$

$X_{RC,i}$ is the degree of rate control for reaction step i in the cycle. $X_{TRC,n}$ is the degree of thermodynamics rate control for intermediate n. Index l is for all the reaction steps that the intermediate n is either the reactant or the product.

4. Catalyst Model Development

Reproduced in part with permission from [The Journal of Physical Chemistry C, 2012, 116, 9029-9042.] Copyright [2013] American Chemical Society

The optimized bulk CeO_2 structure with lattice parameter of 5.48 Å was used to construct the CeO_2(111) surface. Nine atomic layers with the three bottom layers fixed at their bulk positions were utilized in order to simulate the surface. For this model we found that the surface oxygen vacancy formation energies and platinum adsorption energies were converged within 0.05 eV by increasing the number of layers from 9 to 15, and 18.

The structure of the stoichiometric CeO_2(111) surface is depicted in Figure (4-1). The first atomic layer only contains oxygen atoms that are three fold coordinated and have bonds with three Ce atoms in the second atomic layer. The second atomic layer atoms only have seven fold coordinated Ce atoms which have bonds with three surface oxygen atoms at their top and three subsurface oxygen atoms in the third atomic layer.

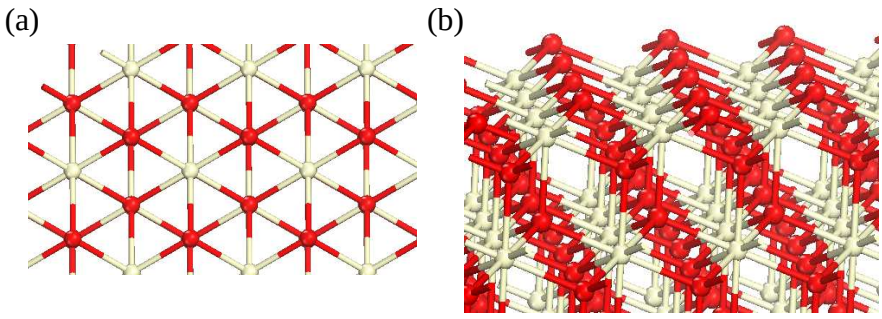

FIGURE 4-1. Structure of CeO_2(111) surface: (a) top view and (b) side view. Cream, and red balls represent Ce, and O atoms, respectively.

This third atomic layer only contains four fold coordinated oxygen atoms. The seventh bond of a Ce atom in the second layer is with oxygen in the fourth atomic layer. This fourth atomic layer is like the first atomic layer except that it is connected with the top Ce layer and as a result the oxygens are four fold coordinated. The tri-layer O-Ce-O repetition along the (111) direction represents a perfect CeO_2 (111) crystal.

To identify a suitable catalyst model for Pt metal cluster on CeO_2(111) surface, we performed different calculations and the results are the subject of this section and organized as follows: For model development we started with the structure of small Pt clusters on the stoichiometric and partially reduced ceria (111) surface. Next, we applied the constrained *ab initio* thermodynamics method to see how is the nature of the Pt/CeO_2(111) catalytic surface under realistic WGS reaction conditions. For instance, we answered the following questions: (1) Are oxygen vacancies stable under WGS reaction conditions? And how does the presence of Pt clusters help create oxygen vacancies? (2) Are oxygen vacancy clusters stable under WGS reaction conditions? (3) Under what reaction conditions are platinum oxide species stable? (4) What is the effect of H_2 on the Pt/ceria surface? (5) What is the effect of CO coverage on the Pt/ceria surface?

4.1. Structure of Small Platinum Clusters on Ceria (111) Surface

Many experimental studies for the WGS reaction have used ceria nanoparticles as a support for metal nanoparticles where different facets of ceria are available for the metal particles to bind and for reaction to occur [13, 163, 225-227]. However, there are many surface science studies where ceria thin films have been used as a support. Bridging this materials gap is not an easy and straightforward task, and while the interaction of metal nanoparticles with ceria nanoparticles is likely quite sophisticated, ideal surface science

studies are often able to capture key features of the real system [228]. Here, we used the most stable low index ceria surface, ceria (111) [201], for our computational study to get a better understanding of the growth pattern of platinum metal particles on both the stoichiometric and reduced ceria surfaces. On the reduced surface, a single surface oxygen vacancy is considered as the nucleation site for the metal adatoms. It is worth noticing that, by experimentally studying the growth of Pt nanoparticles on ceria (111) thin films, Zhou et al. [229] generally did not observe any preferential nucleation and growth of the metal particles at the step-edges of the surface as observed for palladium or gold particles [230, 231].

Table (4-1) illustrates the computed clustering energies for various Pt clusters (Pt_1 to Pt_{10}) on both the stoichiometric and reduced ceria surfaces. Top and side views of the most stable structures are shown in Figure (4-2a,b) for the stoichiometric and reduced surfaces, respectively. Overall, more than one hundred different initial structures with unbiased pre-assumed packing structure of the Pt atoms have been optimized to make sure that, for each case, we have structures that are close to the lowest energy structures. The procedure we followed has previously been described by Zhang et al. [232] with the difference that we sometimes added two or three Pt atoms to the most stable or the most representative smaller Pt cluster structures in order to obtain an initial guess for the larger clusters.

In agreement with previous studies, we find that a single Pt adatom adsorbs on the stoichiometric ceria (111) surface on the oxygen bridge site [203-205, 233]. We calculate an adsorption energy of -3.14 eV, which is in reasonable agreement to computations from Lu and Yang [204] that predict an adsorption energy of -2.91 eV. The larger unit cell that

has been employed in our work seems to be, at least partly, responsible for the energy difference. A much smaller adsorption energy (-2.60 eV) has recently been reported by Loffreda and Delbecq [233] who used a smaller p(2 × 2) unit cell and employed a GGA functional without Hubbard correction. For Pt_1 on the reduced ceria (111) surface, it is known that the oxygen vacancy is the most preferred site for adsorption of the metal adatom. Yang et al. [203] found for the adsorption of Pt_1 on the reduced surface an adsorption energy of -5.27 eV, which is significantly larger than our calculated adsorption energy of -3.49 eV.

TABLE 4-1. Clustering energies (E^{clu}) of Pt clusters on the stoichiometric and partially reduced CeO_2 (111) surfaces, and effect of Pt clusters on the oxygen vacancy formation energy (E^{vf}) of the CeO_2 surface.

	E^{clu} (eV)		
Cluster size	**on CeO_2**	**on CeO_{2-x}**	**E^{vf} (eV)**
clean	--	--	2.37
Pt_1	-3.14	-3.49	2.03
Pt_2	-3.42	-3.59	2.03
Pt_3	-3.83	-3.92	2.10
Pt_4	-4.17	-4.10	2.64
Pt_5	-4.17	-4.26	1.91
Pt_6	-4.19	-4.31	1.63
Pt_7	-4.31	-4.38	1.87
Pt_8	-4.31	-4.40	1.68
Pt_{10}	-4.35	-4.42	1.59

We note that Yang et al.'s results are based on a p(2 × 2) unit cell with a symmetric slab, and the adsorption of Pt was considered on vacancies symmetrically created on both sides of the slab. In order to test the effect of oxygen vacancy concentration on the Pt adsorption energy, we used our current computational set up and calculated the adsorption of Pt on the oxygen vacancy of a smaller p(2 × 2) unit cell. The calculated

adsorption energy of -3.66 eV is still significantly lower than the value reported by Yang et al. [203], and we can currently not explain this discrepancy.

The structures of Pt clusters on the ceria (111) surface have been reported for Pt_4 [204], Pt_8 [228], and, more recently, Pt_n (n = 2−5, 7) [233].

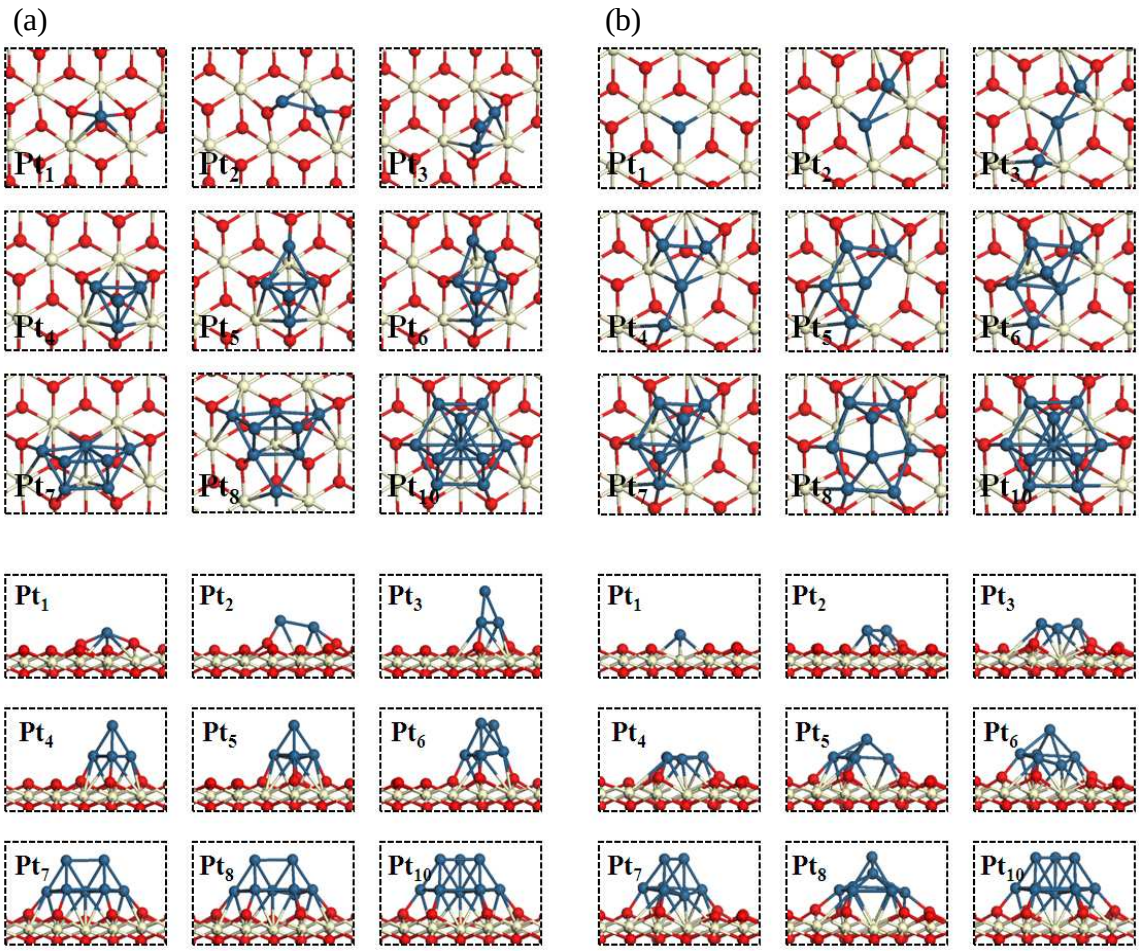

FIGURE 4-2. Top and side views of the lowest energy structures of Pt_n (n=1-10) adsorbed on the (a) stoichiometric and (b) partially reduced CeO_2 (111) surfaces. Cream, red, and navy balls represent Ce, O, and Pt atoms, respectively (this notation is used for all the other reported structures in the next figures while white and gray balls represent H and C atoms).

For Pt_4 on the stoichiometric surface, we found in agreement with Lu and Yang's work [204] the pyramidal structure to be the most stable configuration for Pt atoms. We calculate a clustering energy of -4.17 eV that is 0.11 eV stronger than their reported

value. The most stable structure identified for the $Pt_8/CeO_2(111)$ model is very similar to the structure reported by Vayssilov et al. [228]. Unfortunately, Vayssilov et al. did not report the clustering or adsorption energy for their Pt_8 structure on the ceria surface. The structures reported by Loffreda and Delbecq [233] are quite similar to our most stable structures. However, their reported clustering energies are slightly different from our values since their calculations are based on GGA-DFT without Hubbard correction and a smaller p(2 × 2) unit cell.

Generally, on both the stoichiometric and reduced surfaces, we observe that the metal packing was cubic-closed packed, and starting from metal clusters as small as Pt_{10}, the (111) facet of the metal cluster is clearly recognizable on both the stoichiometric and reduced ceria surfaces. This observation is expected considering that the most stable facet of Pt is also (111) and Pt particles only experience limited strain upon adsorption due to the difference in lattice parameters of Pt and ceria.

Finally, Figures (4-2a) and (4-2b) illustrate the tendency of even very small Pt clusters to form two layered structures on both the stoichiometric and reduced ceria surfaces. Experimental observations from Zhou et al. [229] suggest a mean height of Pt particles on partially reduced ceria thin films of 0.3 nm, while Pt particles on stoichiometric ceria films displayed an average height of about 0.4 nm. Since layers of Pt in Pt (111) surfaces are expected to be ~0.23 nm apart, the height of Pt particles on stoichiometric ceria surfaces suggests that particles with two Pt layers are dominant. We attribute the average height of Pt particles on the reduced surface (almost 1.5 layers of Pt) to the presence of oxygen vacancies under the particles (similar to our Pt_5 and Pt_8 structures in Figure (4-2b)).

4.2. Reducibility of Ceria (111) Surface

Different experiments have suggested the redox mechanism and associative mechanism with hydroxyl group regeneration to be the most important reaction pathways for the WGS reaction mechanism on ceria supported Pt clusters [20, 91, 163, 164, 234-237]. In all of these reaction pathways, the creation of an oxygen vacancy on ceria plays an essential role for water dissociation. In the following, we first show how Pt clusters can facilitate the formation of a single oxygen vacancy on the ceria support. Next, we show the possibility of oxygen vacancy cluster formation under reducing WGS conditions for our Pt_{10}/CeO_2 (111) catalyst model. Finally, we examine the stability of these oxygen vacancy clusters in the presence of hydrogen adatoms on the ceria support created by hydrogen spillover from Pt to the oxide surface.

4.2.1. Single Oxygen Vacancy Formation on Pt_n/CeO_2 (111)

The ceria surface is well-known for its high reducibility. We compute the oxygen vacancy formation energy of CeO_2 (111) as 2.37 eV, which is in close agreement to the 2.25 eV computed by Vayssilov et al. [228]. Next, it has been noticed experimentally that the addition of Pt, Au, etc. clusters increases the reducibility of the ceria surface [238]. To better understand this phenomenon, we computed the oxygen vacancy formation energy in the presence of Pt_n (n = 1−10). Table (4-1) summarizes the results of these calculations. The oxygen vacancy formation energy in the presence of a single Pt atom (2.03 eV) is in reasonable agreement with Yang et al.'s [203] reported value of 1.83 eV. Our calculated oxygen vacancy formation energy in the presence of Pt_8 is 1.68 eV, which is about 0.8 eV less than the reported value by Vayssilov et al. [228] (2.46 eV). We note here that the vacancy formation energy in our current work is calculated using the most stable

structure of Pt_8 cluster on the reduced surface (Figure (4-2b)), which is quite different from the structure used by Vayssilov et al. [228]. For a similar structure, our current model computes a vacancy formation energy of 2.01 eV. The difference of 0.35 eV (2.01 eV versus 2.46 eV) is likely due to a different computational set up, i.e., Vayssilov et al. used the PW91 functional with U = 4 eV, and a p(3 × 4) unit cell. Overall, we find that the reducibility of the CeO_2 (111) surface increases with increasing Pt cluster size and that the vacancy formation energy converges for Pt_{6-10} clusters about 0.8 eV below the bare ceria surface. Only for the Pt_4 cluster do we observe a higher oxygen vacancy formation energy compared to the bare surface. This unusual behavior can be attributed to the highly symmetric Pt_4 structure on the stoichiometric CeO_2(111) surface, as shown in Figure (4-2), where Pt atoms form a tetrahedral cluster with the three base Pt atoms binding to the three adjacent surface oxygen atoms, while the most stable configuration of the Pt_4 cluster on the reduced surface is an open planar structure.

To understand how a gas phase environment affects the reducibility of the ceria surface, we used the constrained *ab initio* thermodynamic approach as described in Section (3-3). Figure (4-3a) illustrates the free energy of formation of an oxygen vacancy on the CeO_2(111), Pt_3/CeO_2(111), and Pt_{10}/CeO_2(111) surfaces as a function of the oxygen chemical potential. Under oxidizing conditions, the presence of a significant number of oxygen vacancies is unlikely except at very high temperatures. Even in the presence of Pt clusters, temperatures of about 1300 K (at an oxygen partial pressure of 1 bar) are required for vacancies to be thermodynamically stable. This observation is qualitatively in agreement with experimental observations where the thermally activated reduction of stoichiometric ceria films requires a temperature treatment above 1000 K [239,

[240]. Also, TPR data [163] show that Pt clusters on the ceria surface promote partial ceria reduction at lower temperatures.

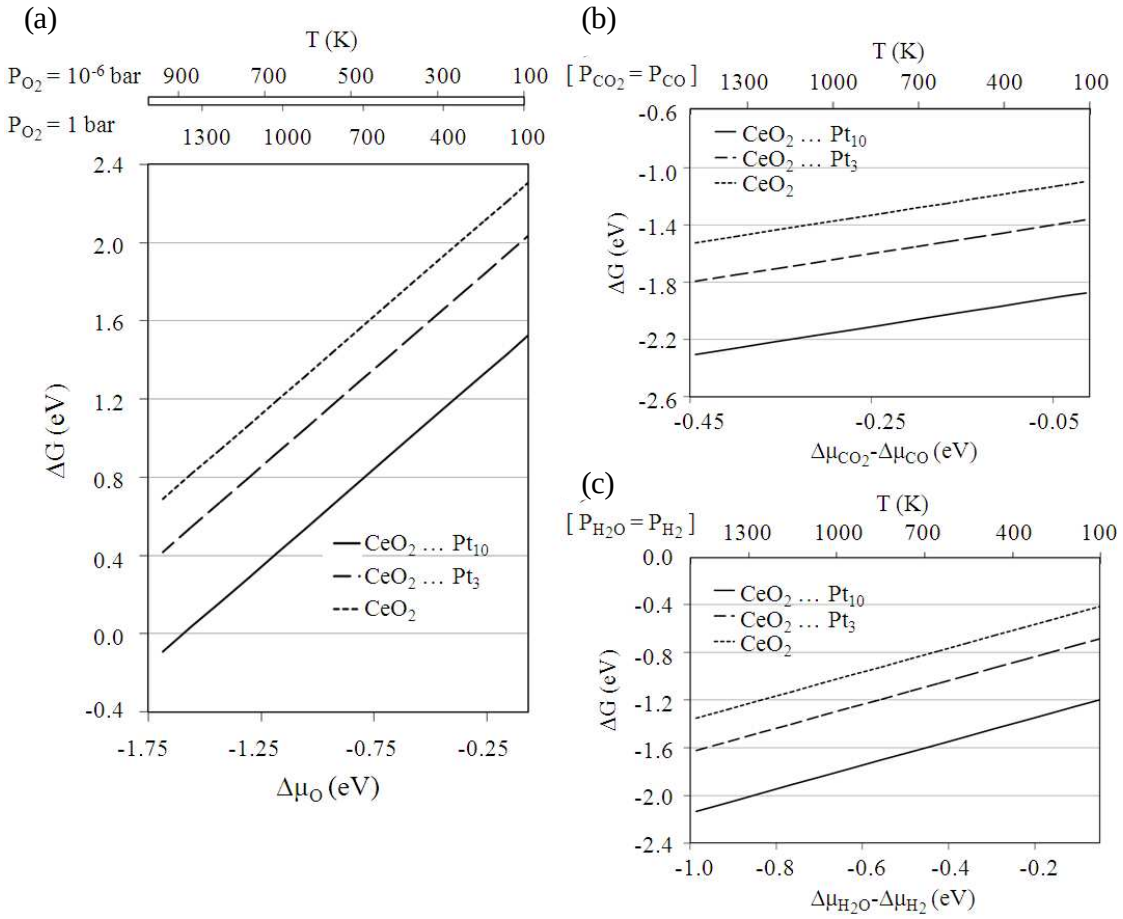

FIGURE 4-3. Gibbs free energy (ΔG) for the formation of an oxygen vacancy on the CeO_2 (111) surface versus: (a) oxygen chemical potential ($\Delta\mu_O$), (b) difference in chemical potentials of CO_2 and CO ($\Delta\mu_{CO2}$ - $\Delta\mu_{CO}$), and (c) difference in chemical potentials of H_2O and H_2 ($\Delta\mu_{H2O}$ - $\Delta\mu_{H2}$).

Figure (4-3b,c) illustrates that, under reducing conditions (assuming a CO/CO_2 and H_2/H_2O atmosphere), similar to WGS reaction or pre-reduction conditions, formation of oxygen vacancies is thermodynamically favorable both on the bare ceria surface and in the presence of Pt clusters. It should be mentioned that Figure (4-3a−c) are theoretically equivalent. Yet, considering that the O_2 partial pressure is very low under reducing conditions and therefore difficult to estimate, we found it more convenient to use the

difference in the chemical potentials of the reducing agents with their oxidized forms (H_2/H_2O or CO/CO_2) to study realistic WGS reaction conditions.

4.2.2. Oxygen Vacancy Cluster Formation on $Pt_{10}/CeO_2(111)$

Considering the reducing conditions during the WGS reaction and the high stability of isolated oxygen vacancies in the presence of Pt clusters, we studied the stability of oxygen vacancy clusters on the catalyst surface. We chose the Pt_{10} cluster model and calculated the energy of removing a second and third oxygen atom from the surface. The optimized structures and their relative vacancy formation energies are summarized in Figure (4-4a). Gibbs free energies of oxygen vacancy cluster formations are illustrated in Figure (4-4b,c) for reducing environments of H_2/H_2O and CO/CO_2, respectively. On our model surface, the first oxygen vacancy formation is 1.59 eV endothermic. The energy for creating the second vacancy is 1.18 eV more endothermic, and the energy for creating the third vacancy is 0.51 eV more endothermic. The third vacancy here is created in such a way that the three vacancy clusters are linearly aligned under three linear Pt atoms, and thus, the structure is more symmetric compared to that of the two vacancy clusters. We also calculated the structure with a nonlinear three vacancy cluster and found that it is less stable than the linear one by less than 0.1 eV. Figure (4-4c) illustrates that, in a CO/CO_2 atmosphere, an oxygen vacancy cluster of 3 vacancies beneath the Pt cluster is stable over the whole temperature range considered. However, in the presence of a H_2/H_2O atmosphere (Figure (4-4b)), only a double oxygen vacancy cluster is stable at relevant temperatures below 800 K. Overall, these findings suggest that vacancies and vacancy clusters might be important to consider while studying the WGS reaction on

ceria supported Pt clusters, e.g., with the third vacancy potentially being an active site for our catalyst model for water dissociation.

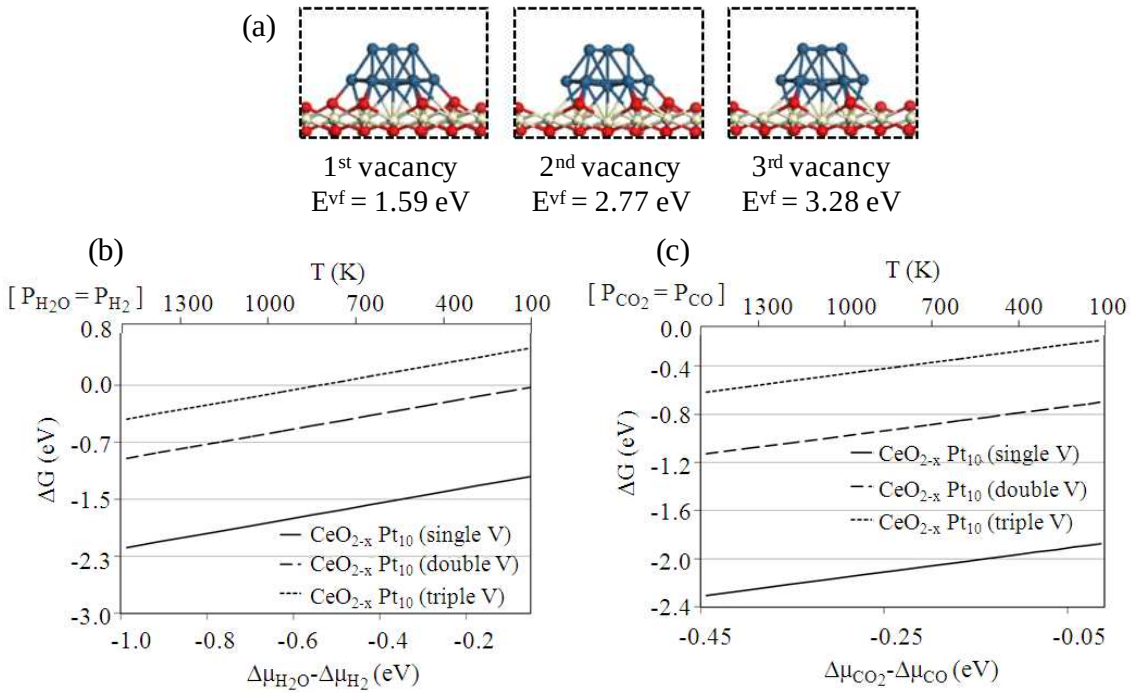

FIGURE 4-4. (a) Optimized structures for a single, double, and triple oxygen vacancy clusters on a Pt_{10}/ceria surface and their relative vacancy formation energies (E^{vf}), (b) and (c) Gibbs free energies (ΔG) for the formation of oxygen vacancy clusters on the CeO_2 (111) surface in H_2O/H_2 and CO_2/CO atmospheres, respectively.

4.2.3. Effect of H_2 on the Stability of Oxygen Vacancy Clusters on $Pt_{10}/CeO_2(111)$

During hydrogen activation of Pt/ceria catalysts, it is possible for H atoms to spillover to the ceria surface [241] or for H_2 to dissociate on ceria [242]. It has been noticed previously that irreversible over-reduction of ceria can render the Pt/ceria catalyst inactive by making the ceria surface unable to exchange its oxygen atoms [225, 243]. To study the effect of H adatoms on the Pt_{10}/CeO_2 catalyst model and its ability to exchange oxygen, we add 6 hydrogen atoms to the unit cell in the form of triangular clusters [162] around the Pt_{10} cluster corresponding to hydrogen coverage of 0.375 ML (based on the surface oxygen

atoms of the bare ceria surface). The H_2 adsorption energy per H_2 is -2.36 eV confirming the possibility of a high H-coverage. To study the oxygen vacancy and vacancy cluster formation on this surface, we followed the same procedure as described for the non-hydroxylated ceria surface. Figure (4-5) summarizes the optimized structures, the energies of the first, second, and third oxygen vacancy formations, and the free energies of single, double, and triple oxygen vacancies for a hydroxylated ceria surface.

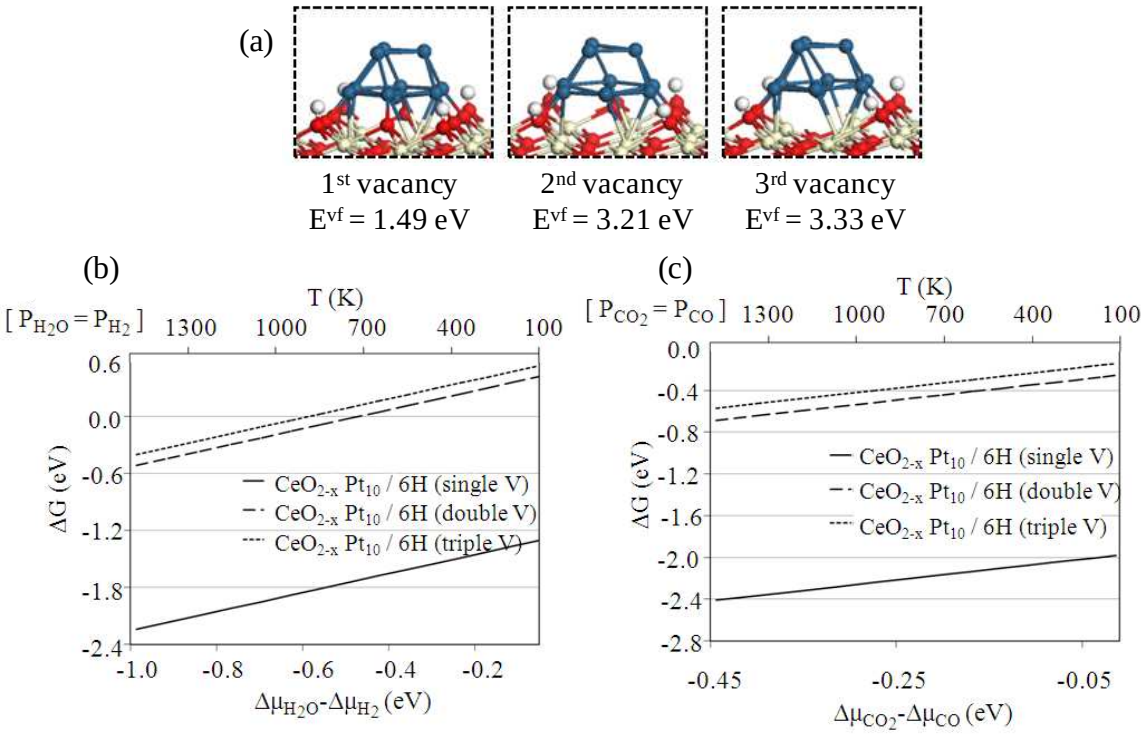

FIGURE 4-5. (a) Optimized structures for a single, double, and triple oxygen vacancy clusters on a Pt_{10}/hydroxylated-ceria surface and their relative vacancy formation energies (E^{vf}), (b) and (c) Gibbs free energies (ΔG) for the formation of oxygen vacancy clusters on the hydroxylated CeO_2 (111) surface in H_2O/H_2 and CO_2/CO atmospheres, respectively.

While the energy of the first and third oxygen vacancy formations do not change considerably compared to the non-hydroxylated surface, the second vacancy formation becomes more endothermic in the case of the hydroxylated surface. As a result, calculations predict that the second and third oxygen vacancies might not form if we

assume conditions equivalent to an equimolar H_2/H_2O gas phase (Figure (4-5b)). In contrast, in an equimolar CO/CO_2 gas phase, stable vacancy clusters are still predicted in the WGS reaction temperature range of 400−600 K (Figure (4-5c)). The relatively large energy difference between the first and second oxygen vacancy formation of 1.72 eV is preventive in thinking about any catalytic redox cycle between these two structures. We will further discuss the possibility of having an active hydroxylated catalyst with oxygen vacancies as active sites in Section (4-4-2).

4.3. Adsorption of Oxygen Atoms on $Pt_{10}/CeO_2(111)$

Calcination of catalytic samples or room temperature air exposure of Pt/ceria surfaces can stabilize PtO_x species. XPS peaks of Pt^{2+} and Pt^{4+} for as-prepared samples have been related to these Pt oxide species, while different peak intensities have been detected for differently prepared samples [225]. Here, we limit our study of oxygen adsorption to adsorption of a single oxygen adatom and its stability in oxidizing and reducing environments.

Figure (4-6a) summarizes the adsorption energies calculated with reference to the experimentally corrected energy of an O_2 molecule and optimized structures of an oxygen adatom at various positions of the $Pt_{10}/CeO_2(111)$ surface. On the basis of our computations, oxygen atoms adsorbing at non-interfacial Pt atop sites have the strongest adsorption energy (-1.76 eV) with a Pt−O bond length of 1.77 Å.

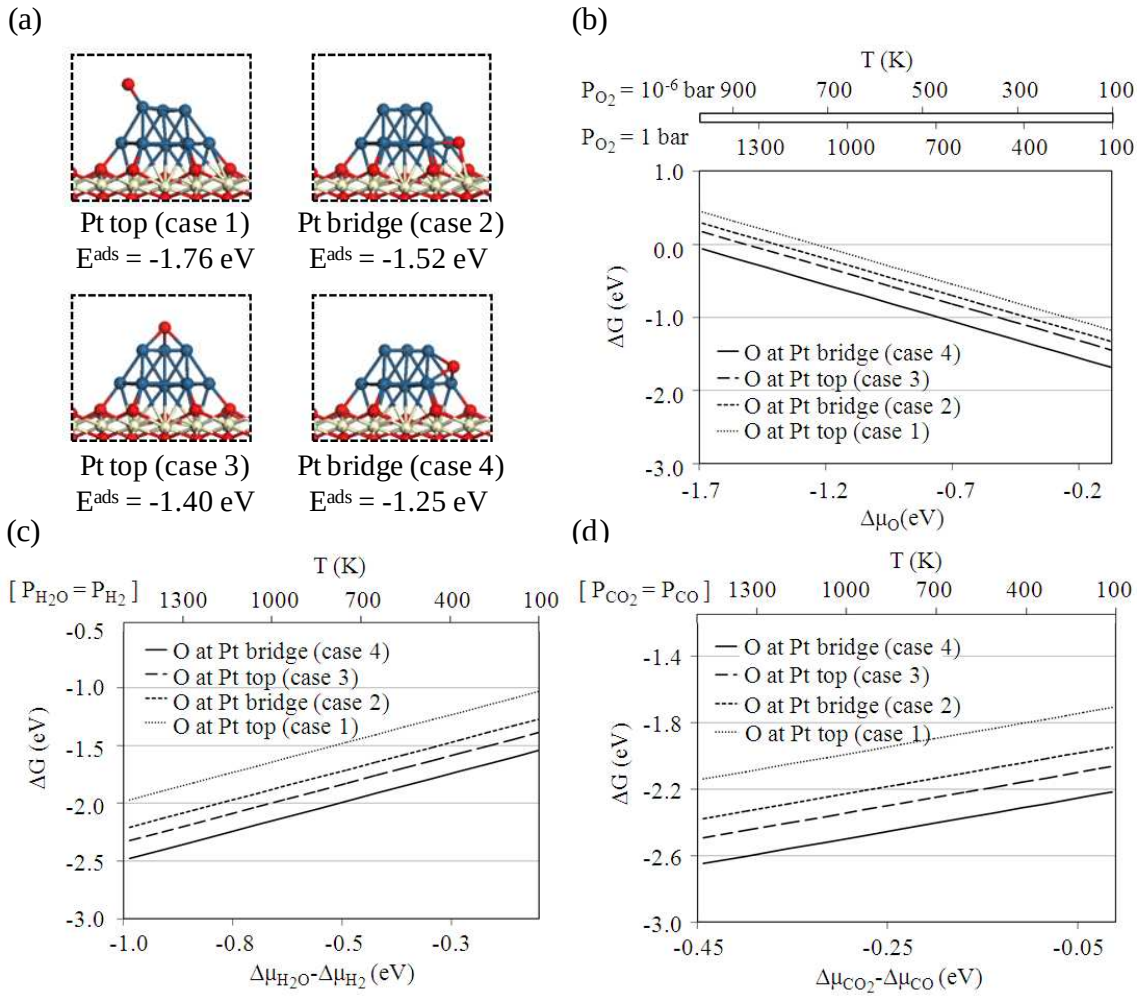

FIGURE 4-6. (a) Adsorption energies (E^{ads}) and optimized structures for the adsorption of one oxygen atom on a Pt_{10}/CeO_2 (111) surface, (b) Gibbs free energy (ΔG) for the adsorption of an oxygen atom on the Pt_{10}/CeO_2 (111) surface versus oxygen chemical potential ($\Delta\mu_O$), (c) and (d) Gibbs free energies (ΔG) for the reduction of the O-Pt_{10}/CeO_2 (111) surface by H_2 and CO, respectively.

Figure (4-6b) illustrates the calculated free energy of oxygen adsorption as a function of the oxygen partial pressure and temperature for the structures shown in Figure (4-6a). Under oxidizing condition, e.g., below 1000 K and an oxygen partial pressure of 1 bar, all top and interface Pt atoms of the Pt_{10} cluster model can exist as Pt−O. In other words, thermal activation of Pt clusters on the ceria surface requires high temperatures and a low oxygen partial pressure. While we did not consider adsorption of multiple

oxygen atoms on the Pt cluster, we expect lateral interaction effects of adsorbed oxygen atoms to be small enough that our conclusion stays unaltered even at higher oxygen coverages (although lower temperatures are expected to be required to reduce non-interfacial Pt sites).

Experimentally, it has both been suggested that PtO_x species are stable and not stable under WGS reaction conditions [175, 243]. Figure (4-6c,d) illustrates the free energies for the reduction of Pt−O species at different sites of the Pt_{10} cluster under WGS reducing conditions (by either CO or H_2). Clearly, under reducing conditions, it is not thermodynamically favorable to have adsorbed oxygen atoms on the Pt cluster even at very low temperatures. In fact, it can be estimated that the oxygen atom adsorption energy had to be stronger than -3.7 eV for observing stable Pt−O species under reducing conditions (which is significantly larger than our computed energies for the $Pt_{10}/CeO_2(111)$ system even when we consider possible modeling errors). This suggests that with time-on-stream Pt oxide species, which are formed during preparation of Pt/ceria catalysts, will react with CO (or H_2) to form CO_2 (or H_2O), and under steady-state WGS reaction conditions, the catalyst will be free of any oxygen adatoms. In fact, H_2-TPR results indicate that oxygen reduction of Pt/ceria catalytic samples generally starts at about 480 K [225, 243], and by heating the samples in H_2 at 500 °C (773 K), Pt atoms will reduce to their metallic forms. A low temperature peak has also been observed at 400 K [99]. The TPR results will be further discussed in Section (4-5).

4.4. Adsorption of CO Molecules on $Pt_{10}/CeO_2(111)$ Catalyst Model

Strongly coverage dependent CO adsorption energies on the Pt(111) surface have been reported [244], and it has also been observed that the interaction of CO is even stronger on isolated [208] and oxide supported Pt clusters [208, 245]. Considering furthermore that a negative reaction order has been observed for the WGS reaction on the Pt(111) surface with respect to CO molecules [246], a good WGS catalyst model ($Pt_{10}/CeO_2(111)$) should probably contain thermodynamically stable CO molecules that facilitate the inclusion of lateral interactions on various reaction pathways. In the following, we first study CO adsorption on the Pt cluster to better understand the lateral interaction of CO molecules on the $Pt_{10}/CeO_2(111)$ system under WGS reaction conditions. Next, we study the effect of CO coverage on the redox properties of the ceria surface for both the clean and hydroxylated surfaces. While CO has been observed to adsorb on the ceria (110) surface, its adsorption on the (111) surface is very weak ($\Delta E_{ads} < 0.2$ eV [247]) and has therefore not been considered here.

4.4.1. CO Adsorption on $Pt_{10}/CeO_2(111)$

Figures (4-7a) and (4-7b) summarize optimized structures of a single CO molecule adsorbed at different sites of the $CeO_2(111)$ supported Pt_{10} cluster, their relevant adsorption energies, and the calculated CO adsorption free energy versus CO chemical potential. On the basis of our calculations, a single CO molecule prefers to linearly adsorb on non-interfacial Pt sites with an adsorption energy of -2.58 eV. This behavior is slightly different to the Pt_4 on $CeO_2(111)$ system where the Pt_4 bridge site has been identified to be the most preferable site for CO adsorption (on the Pt_{10} cluster, adsorption on the bridge site was -2.02 eV) [208]. Linear CO adsorption on the Pt atoms at the TPB is

also strong with an adsorption energy of -2.00 eV. For the linearly adsorbed CO molecule, we compute a C−O bond length of 1.168 Å for the non-interfacial Pt site and 1.164 Å for the TPB Pt site.

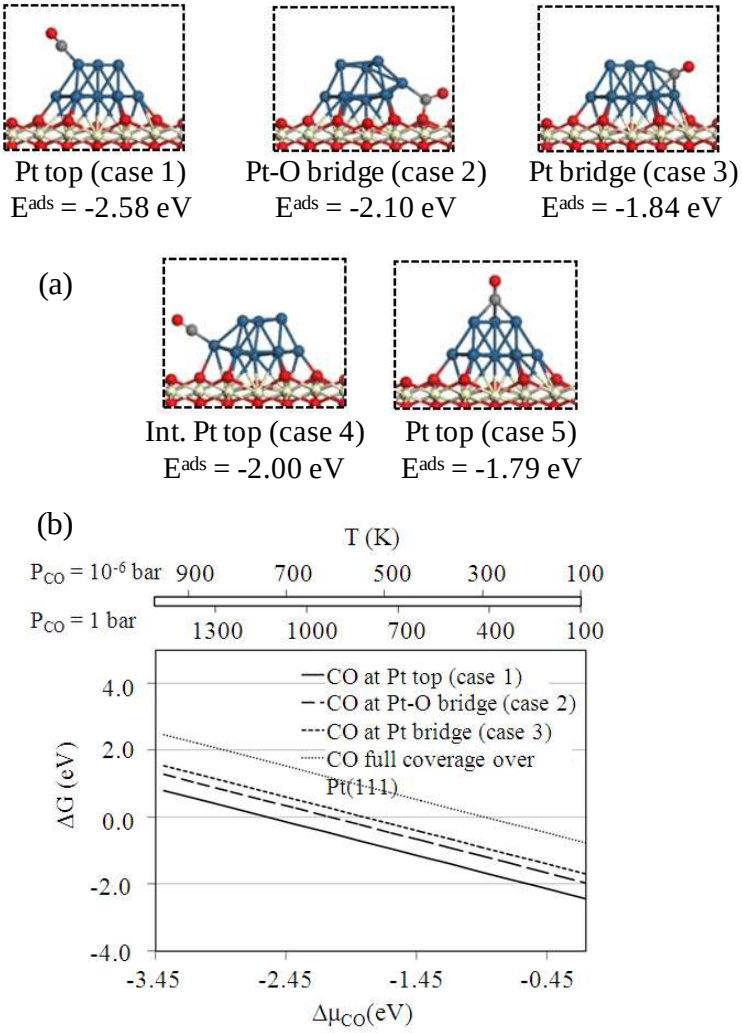

FIGURE 4-7. (a) Optimized structures for an adsorbed CO molecule on a Pt_{10}/CeO_2 (111) surface and their relevant adsorption energies (E^{ads}), (b) Gibbs free energy (ΔG) for the adsorption of a CO molecule on the Pt_{10}/CeO_2 (111) surface versus CO chemical potential ($\Delta\mu_{CO}$).

Furthermore, Figure (4-7b) illustrates that at low CO partial pressures of 10^{-6} bar, linearly adsorbed CO molecules at TPB Pt atoms are not stable above 600 K and linearly adsorbed CO molecules at non-interfacial and under-coordinated Pt sites are not stable

above 700 K. Overall, our computations are in agreement with Kalamaras et al.'s [236] observations obtained from *in situ* DRIFT and TPD. Two high frequency peaks have been observed for their low Pt content catalyst samples that were related to linear CO molecules. While the first peak disappeared above 300 °C (573 K), the second peak showed a higher thermal stability and disappeared above 400 °C (673 K). We are inclined to relate the first peak to adsorbed CO at TPB Pt sites and the second peak to adsorbed CO on the under-coordinated Pt edge sites.

Next, we considered higher coverages of CO by adding three CO molecules to the non-interfacial Pt sites and studying adsorption of a fourth CO at the TPB. The relevant adsorption energies, their optimized structures, and the calculated free energies are illustrated in Figure (4-8). For our small Pt_{10} cluster, the average heat of CO adsorption for having one to three CO molecules at non-interfacial Pt sites does not change significantly (-2.58 eV for a single CO molecule and -2.48 eV per CO for 3 CO molecules). However, the differential CO adsorption energy of a fourth CO molecule at TPB Pt atoms in the presence of 3 CO molecules at non-interfacial Pt sites is reduced by 0.34 and 0.18 eV, for linear CO and Pt−O bridged CO, respectively. The calculated free energies of these structures illustrate that non-interfacial Pt sites of the metal cluster are prone to be poisoned by even small amounts of CO in the WGS reaction feed (10^{-6} bar) specifically at low temperatures (T < 700 K). In other words, under-coordinated edge sites of Pt particles are the most vulnerable sites for CO poisoning under WGS reaction conditions, and only TPB Pt atoms are likely available for the low temperature WGS reaction on small ceria supported Pt clusters.

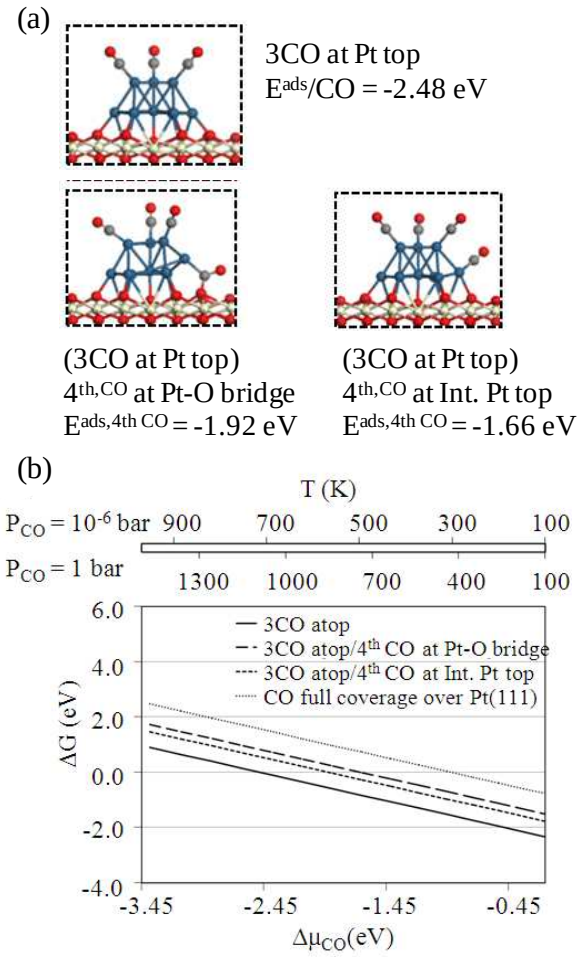

FIGURE 4-8. (a) Optimized structures for the adsorption of three CO and four CO molecules on a Pt_{10}/CeO_2 (111) surface and their relevant average and differential CO adsorption energies (E^{ads}). (b) Gibbs free energy (ΔG) for the adsorption of a 4th CO molecule at the TPB of the Pt_{10}/CeO_2 (111) surface versus CO chemical potential ($\Delta\mu_{CO}$).

4.4.2. Oxygen Vacancy Cluster Formation on Pt_{10}/CeO_2(111) Catalyst Model with CO Covered Atop Sites

Next, we investigated the effect of CO coverage on the stability of oxygen vacancy clusters for both the clean and hydroxylated ceria surfaces. Table (4-2) summarizes the first, second, and third oxygen vacancy formation energies on the clean and hydroxylated ceria surfaces, while non-interfacial Pt sites of the Pt_{10} cluster are covered by CO. With respect to the clean surface, adsorbed CO molecules make the first oxygen vacancy formation more endothermic by 0.52 eV. Similarly, adsorbed CO hinders the creation of

the second vacancy by 0.18 eV and the third vacancy by 0.02 eV. As a result, the presence of adsorbed CO molecules slightly decreases the energy difference (0.51 eV versus 0.35 eV) between the structures with double and triple oxygen vacancy clusters, which might be relevant for the redox mechanism of the WGS reaction (cycle between double and triple vacancy cluster). On the hydroxylated ceria surface, adsorbed CO molecules make the first and third oxygen vacancy formations more endothermic by 0.30 and 0.18 eV, respectively. The second vacancy formation becomes less endothermic by 0.09 eV due to the presence of adsorbed CO molecules. Clearly, also in the presence of H adatoms on the ceria surface and CO molecules on non-interfacial Pt atoms, it is still possible to envision a catalytic redox cycle for the WGS reaction between structures with double and triple oxygen vacancy clusters.

TABLE 4-2. Energies for removal of the 1st, 2nd, and 3rd oxygen atoms from Pt_{10}/ceria surface in the presence of adsorbed CO molecules on non-interfacial Pt sites for both the clean and hydroxylated ceria surface.

	clean ceria	**hydroxylated ceria**
	E^{vf} (eV)	**E^{vf} (eV)**
1st vacancy	2.11	1.79
2nd vacancy	2.95	3.12
3rd vacancy	3.30	3.51

Figure (4-9a,b) illustrates the free energies of the first, second, and third oxygen vacancy formations on the clean ceria surface in H_2/H_2O and CO/CO_2 atmospheres, respectively. Figure (4-9c,d) illustrates the same free energies for the hydroxylated ceria surface. In all of these cases, non-interfacial Pt sites are covered by CO. For both ceria surfaces, the triple oxygen vacancy cluster is stable in the presence of CO/CO_2. In the case of the hydroxylated surface without CO atop sites, double and triple oxygen

vacancies are not stable in a H_2/H_2O environment in the temperature range of 400 to 700 K.

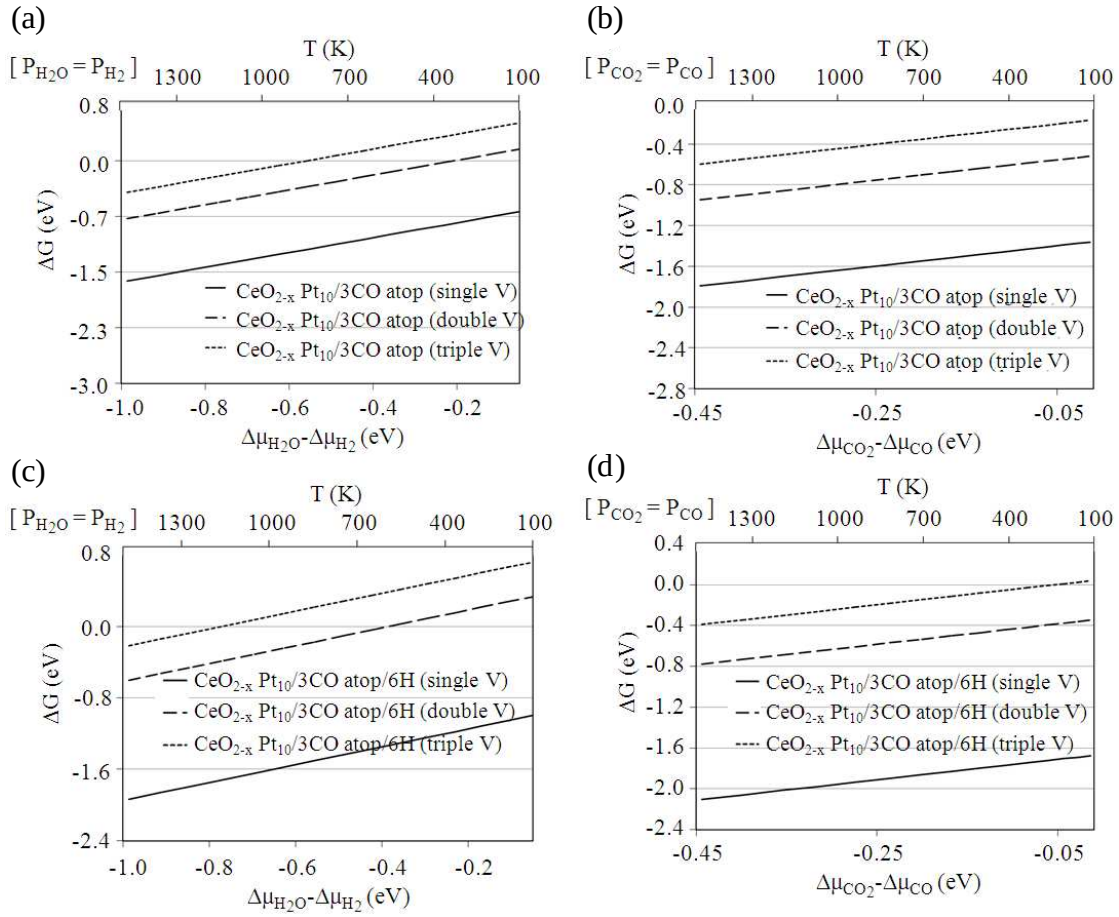

FIGURE 4-9. (a) and (b) Gibbs free energies (ΔG) for the formation of oxygen vacancy clusters on a clean ceria surface in H_2O/H_2 and CO_2/CO atmospheres, respectively; (c) and (d) the same as (a) and (b) but for the hydroxylated ceria surface. In all cases the non-interfacial Pt sites are covered by CO.

For the hydroxylated surface with adsorbed CO and at the lower limit of the aforementioned temperature interval, double and triple oxygen vacancies are not stable. However, at temperatures above 600 K, the double vacancy is stable, and we might be able to assume that a reaction cycle between the double and triple oxygen vacancies is facile since the energy difference between these two structures is small (the third vacancy is in this case the active vacant site). The same conclusions can be made for the non-

hydroxylated surface in the presence of adsorbed CO molecules. In other words, adsorbed CO molecules might have a compensation effect for the over-reduction of the ceria surface and help activate the hydrogen adsorbed ceria surface.

4.5. Adsorption of Hydrogen on $Pt_{10}/CeO_2(111)$ Catalyst Model

Surface reduction of ceria by hydrogen both in the presence and in the absence of metal particles has been reported [241, 242]. In the previous sections, we discussed the possibility of over-reduction of the Pt/ceria catalyst during the WGS reaction and the importance of vacancies and CO molecules for having an active catalyst for redox reactions. To illustrate how ceria reduction by H_2 might occur, we studied hydrogen adsorption and stability at various sites of the $Pt_{10}/CeO_2(111)$ model. Furthermore, similar to CO, a negative reaction order has also been observed for H_2 during the WGS reaction on alumina [246], titania [248], and ceria [249] supported Pt clusters. In the following, we exemplify through our $Pt_{10}/CeO_2(111)$ catalyst model the possible role that the CO coverage plays on competitive CO and H adsorption at TPB Pt atoms that might explain the observed negative H_2 reaction order.

Figure (4-10a) summarizes the hydrogen adsorption energies calculated with reference to the energy of a H_2 molecule and optimized structures of a single H atom at different sites of $Pt_{10}/CeO_2(111)$. Our calculations predict that hydrogen adsorption on ceria is the strongest (-1.32 eV), followed by adsorption on non-interfacial Pt sites (-0.85 eV) and bridge sites on TPB Pt atoms (-0.63 eV). Considering, furthermore, that H_2 easily adsorbs dissociatively on Pt, we might be able to assume that hydrogen spillover is feasible and facile. Figure (4-10b) illustrates the calculated free energies for H adsorption at different sites of the $Pt_{10}/CeO_2(111)$ model. At a high H_2 partial pressure of 1 bar and

low temperatures (T < 800 K), an H adatom is stable on both non-interfacial and TPB Pt atoms. Far from the Pt cluster, H adatoms are stable on the ceria surface even at relatively high temperatures (900 K) and low (10^{-6} bar) H_2 partial pressures. However, H adatoms on the adjacent oxygen atoms to the Pt cluster are only stable at temperatures below 500 K (at P_{H2} = 1 bar).

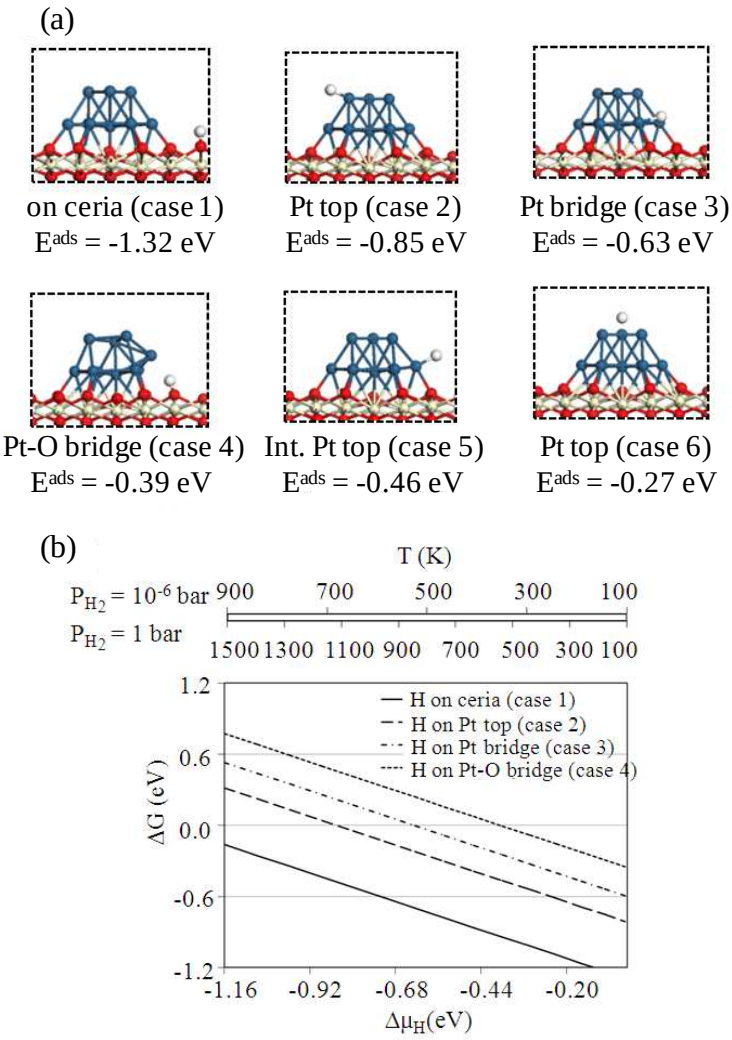

FIGURE 4-10. (a) Adsorption energies (E^{ads}) and optimized structures for the adsorption of a single H atom on a Pt_{10}/CeO_2 (111) surface, (b) Gibbs free energy (ΔG) for the H adsorption on the Pt_{10}/CeO_2 (111) surface versus H chemical potential ($\Delta\mu_H$).

Interestingly, reduction of Pt/ceria catalytic samples by H_2 generally starts at about 480 K [225, 243]; while a lower temperature peak has also been observed at 400 K accompanying

the higher temperature peak [225]. These two peaks are attributed to two different types of surface oxygens [225]. Figure (4-10b) illustrates that at 400 K and P_{H2} = 1 bar, H adatoms are stable at all sites of the $Pt_{10}/CeO_2(111)$ model. However, removal of oxygen-bonded H adjacent to a Pt cluster might be possible at 400 K and might be related to the low temperature H_2−TPR peak (unfortunately, DFT calculations are likely not accurate enough for final peak assignment). At temperatures around 500 K, these H adatoms are no longer stable. However, H adatoms on the Pt cluster can be stable up to 800 K for boundary Pt atoms and up to 1100 K for non-interfacial Pt atoms. Thus, they might further react with oxygen adatoms on the Pt cluster to produce the second peak in the H_2−TPR experiment (high P_{H2}). Furthermore, experimentally, it has been observed that, after H_2 reduction of the ceria surface, it is possible to recover the initial oxidation state by pumping off the samples at 773 K [241]. Through our calculations, we emphasize the importance of the partial pressure of H_2 in the environment for stabilizing or destabilizing H adatoms on ceria. At $P_{H2} = 10^{-6}$ bar, it is still possible to have stable hydrogen atoms on the ceria surface even at 900 K, and computations predict that we need to reduce the pressure to around 5.4×10^{-8} bar to destabilize the adsorbed H atoms on the ceria surface at 773 K.

Comparing the adsorption energies for H atoms and CO molecules at different sites of the Pt_{10} cluster, it might initially seem that CO adsorbs much stronger compared to hydrogen on all sites. However, to more carefully investigate competitive adsorption of H and CO, we computed multi-component Langmuir adsorption isotherms for the $Pt_{10}/CeO_2(111)$ and the CO-covered $Pt_{10}/CeO_2(111)$ structures as described in Section (3-

5). We note that we do not expect oxygen vacancies and H-adsorbed ceria to qualitatively change our conclusions.

Figure (4-11a) illustrates Langmuir adsorption isotherms for competitive hydrogen and CO adsorption on non-interfacial Pt sites (relevant structures in the inset).

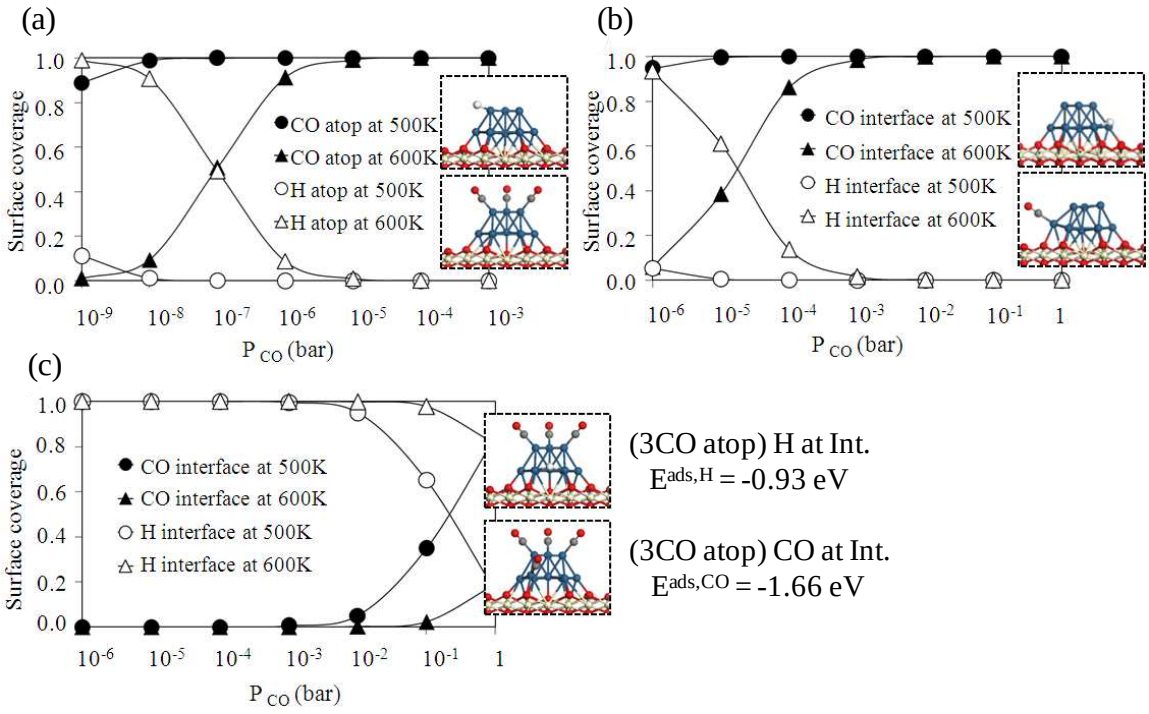

FIGURE 4-11. Equilibrium surface coverage (Langmuir adsorption isotherms) at 500 K and 600 K for H and CO on (a) non-interfacial Pt atoms, (b) TPB Pt atoms, and (c) TPB Pt atoms with non-interfacial Pt sites covered by CO molecules. The H_2 partial pressure is 1 bar.

It is apparent that even at low CO partial pressures ($P_{CO} > 10^{-4}$ bar), the under-coordinated non-interfacial Pt sites are covered by CO and not hydrogen. Figure (4-11b,c) illustrate the Langmuir adsorption isotherms for competitive hydrogen and CO adsorption on TPB Pt atoms for clean and CO covered non-interfacial Pt sites, respectively. For all isotherms, we used a H_2 partial pressure of 1 bar. It is apparent that the presence of co-adsorbed CO molecules has a considerable effect on CO and H

adsorption at TPB Pt sites. Even at low temperatures and relatively high partial pressures of CO, we observe a high coverage of H atoms at TPB Pt sites possibly explaining a negative reaction order with respect to H_2 for the WGS.

4.6. Conclusion

To investigate the nature of small Pt clusters on CeO_2(111) surfaces under WGS-relevant reaction conditions, constrained *ab initio* thermodynamic simulations have been performed. The results are of importance to find a realistic catalyst model for future kinetic studies. We found that the clustering of Pt metal atoms on both stoichiometric and partially reduced ceria follows a closed-packed arrangement, and for clusters as small as Pt_{10}, the (111) facet of the metal cluster is clearly recognizable. In agreement with experimental observations, we found that Pt clusters promote the reducibility of the ceria surface. This effect seems to be converged for clusters as small as Pt_{8-10}. Oxygen vacancies are unlikely to play any role under oxidizing conditions except at very high temperatures or very low oxygen partial pressures. However, under reducing conditions of either CO or H_2, formation of oxygen vacancies and vacancy clusters are thermodynamically favorable. Furthermore, oxygen adatoms are not stable under realistic WGS conditions on ceria supported metal clusters. Instead, non-interfacial Pt sites are prone to be covered by CO molecules. The presence of these coadsorbed CO species does not change the redox behavior of the ceria surface significantly. However, they change the interaction of CO and H species at TPB Pt atoms and favor a high H coverage at the TPB even at low temperatures and relatively high CO partial pressures. Finally, we showed that, during catalyst activation with H_2, it is possible for H atoms to spillover to the ceria surface. These H adatoms change the redox properties of the ceria surface and

make even double vacancy clusters unstable in a H_2/H_2O environment and at relatively low temperatures (400−700 K). However, under WGS reaction conditions, the presence of CO molecules improves the redox cyclability of the hydroxylated ceria surface by stabilizing double vacancy clusters of the Pt_{10}/CeO_2 catalyst model.

5. Mechanistic Study

As discussed in the second chapter, it has been proposed that ceria supported Au and Pt catalysts are bifunctional and the interfacial metal atoms and reducible oxide support atoms at the three-phase boundary (TPB), which is formed by the metal cluster, the oxide support, and the gas phase, are very important for the reaction.[16, 19-23, 72, 81, 93-99, 250] Activity of nearly metal-free ceria catalysts[13, 102] or inversely supported ceria nanoparticles on Au (111) substrate[21, 99] offer some experimental evidence for this hypothesis. Furthermore, it has been noted that for the low temperature WGS reaction the rate scales linearly with the total length of the TPB.[97, 98, 251] The importance of the interfacial sites of the oxide supported Pt catalysts for the low temperature shift reaction has been further manifested by activating the irreducible oxide supported Pt catalysts with small amounts of alkali promoters.[175] The activity has been attributed to the partially oxidized Pt-alkali-$O_x(OH)_y$ species.

Characterization of these multi-phase heterogeneous catalytic surfaces under operating conditions is difficult and interpretation of the results requires meticulosity. For this reason, we aimed to apply appropriate modeling approaches to shed some light on the properties of the TPB under low temperature WGS reaction conditions. In the previous chapter, we studied the nature of the active site of small Pt clusters on the ceria (111) surface.[252] We illustrated the importance of the TPB sites for the reaction and the key role of the lateral interaction of CO molecules for the chosen Pt_{10}/CeO_2 (111) catalyst

model. We also showed the eminence of vacancy clusters at the interface of the Pt cluster and ceria surface due to the presence of both CO and H_2 in the environment and the effect of having a hydroxylated ceria surface. In this chapter, we aim to study the mechanism of the WGS reaction at the TPB for the Pt_{10}/CeO_2 (111) catalyst model.

The dominant reaction pathway for the WGS reaction is still controversial and the general consensus is that the state of the surface and the dominant pathway are strongly dependent on the reaction condition.[86, 105, 235, 250, 253-255] Different pathways have been proposed for the reaction on Pt-ceria catalytic surfaces; for instance, the redox mechanism and the associative mechanism with formate, carbonate, and carboxylate formation as active intermediates. The associative mechanism with redox regeneration (or equivalently, OH group regeneration) has also been proposed. The main difference between the associative mechanism and the associative mechanism with redox regeneration is that the latter one involves the creation of an oxygen vacancy during the cycle. Instead, in the associative mechanism CO would be directly oxidized with the oxygen of water and there is no removal and replacement of the lattice oxygen of the oxide support in this pathway.

Schematic representations of the redox pathway and the associative carboxyl pathway are shown in Figure (5-1). In the redox path, Figure (5-1a), the first step is CO oxidation by the interfacial oxygen of the reducible oxide support, creating an oxygen vacancy. In the second step, water dissociates on the vacancy to produce hydrogen and re-oxidize the surface to close this cycle. The associative carboxyl path, Figure (5-1b), in contrast to the redox pathway does not involve creation of a vacancy during the cycle. While several studies have emphasized that water adsorption is more facile on the

vacancy of the reduced ceria surface, it is possible that water dissociatively adsorbs on the cerium metal of the ceria surface to create one mono-coordinated and one bridging hydroxyl groups on the surface (structure IV). After water dissociation, an adsorbed CO can form a carboxyl group with the mono-coordinated –OH group. The next step is carboxyl dissociation to produce carbon dioxide and hydrogen. The associative carboxyl pathway with redox regeneration would be a combination of these two pathways: creation of vacancy during the cycle and its refilling, association of adsorbed CO and OH group of the support through a carboxyl intermediate.

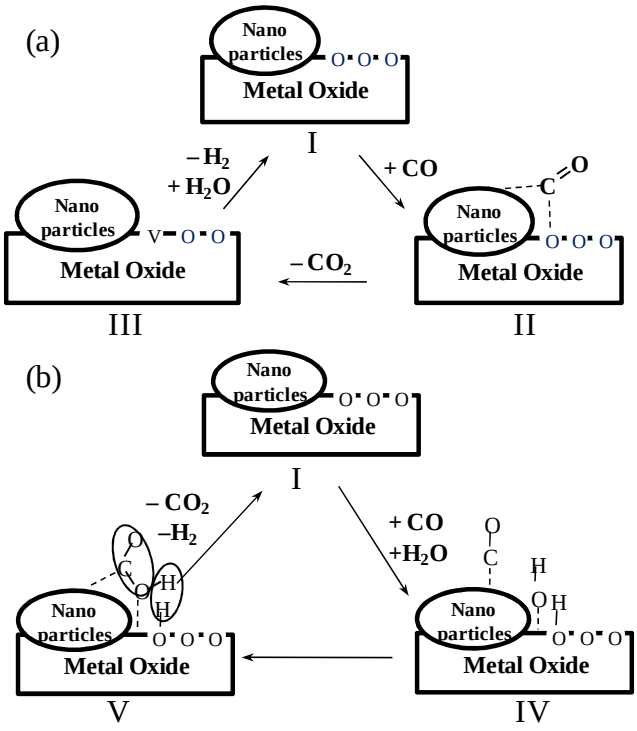

FIGURE 5-1. Schematic representation of the (a) Redox pathway and (b) Associative Carboxyl pathway at the interfacial site of a metal cluster with a reducible metal oxide

For studying the WGS reaction mechanism a different variety of experiments have been done on noble-metal/ceria catalysts. For instance, temperature programmed desorption (TPD) studies[256] have shown that oxygen from ceria can react with the CO

adsorbed on metals and pulse-reactor studies[257] have demonstrated that reduced ceria can be oxidized by CO_2. Presumably the reduced ceria can also be oxidized by H_2O. Hilaire et al.[89] carried out a mechanistic study for the WGS reaction on Pd/ceria catalysts using kinetic rate measurements, pulse studies, and also DRIFTS measurements. They found that the reaction mechanism involves a redox cycle and the ceria was largely reduced and covered by carbonate species, which might have "limited" the reaction rates. In fact, the carbonate mechanism can be considered as a special case of the redox mechanism with different lifetime of the carbonate species and a different extent to which the two steps which involve reduction and re-oxidation of the support are separated in time. Kalamaras et al.[235] recently reported a switch of the WGS reaction mechanism on Pt/CeO_2 from redox to a combination of redox and associative formate with –OH group regeneration occurring after increasing the reaction temperature from 473 to 573 K. They used steady-state isotopic transient kinetic analysis (SSTIKA) experiments coupled with mass spectrometry (MS) and DRIFTS techniques during their studies.

There might be non-traditional pathways dominant during the WGS reaction that would involve transfer of oxygen from the support to the metal particle to facilitate formation and stabilization of the intermediates. Extremely high WGS activity of $Pt/CeO_x/TiO_2$ has been attributed to this kind of reaction mechanism.[258] Since there are limitations on special and temporal resolution of the characterization techniques, it is possible that the most active reaction intermediate not being detected due to its limited lifetime and a narrow zone of formation and decomposition just at the interface of the metal and metal oxide support. For instance, a carboxyl intermediate has been suggested for the WGS yet it has not been observed experimentally.

In our work we target to study the traditional pathways. We applied a pure DFT based microkinetic modeling method to investigate the redox, the associative carboxyl route with redox regeneration, and also the associative carboxyl pathway that has been found to be the dominant path for the Pt (111) and Au/ceria (111) surfaces.[259-262] Our initial model has a Pt_{10} cluster covered by CO molecules on the atop sites and supported on a partially hydroxylated ceria (111) surface in the presence of two vacancies just beneath the Pt cluster. We assumed a 0.375 ML of hydrogen coverage based on the bare ceria surface that corresponds to six hydrogen atoms for our unit cell size. Figure (5-2) depicts this initial catalyst model structure.

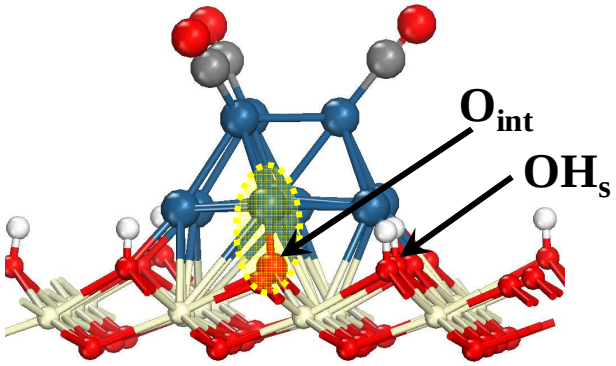

FIGURE 5-2. Initial Pt_{10}/CeO_2 (111) catalyst model used to study the WGS reaction mechanism. Cream, red, and navy balls represent Ce, O, and Pt atoms, respectively; while white and gray balls represent H and C atoms. In our notation, the interfacial oxygens (O_{int}) are those top layer oxygens that are the nearest neighbor to the Pt cluster while surface oxygens (O_s) are the other top layer oxygens. In our notation, OH_s means that hydrogen has made hydroxyl group with the surface oxygen. The highlighted area corresponds to our initial active site ($*_{Pt}$-O_{int}).

This chapter has been organized as follows: The first section is on different redox pathway models that are derived from our initial catalyst model structure. The second section is on the associative carboxyl pathway that is also derived from our initial catalyst model. In the final section, we changed the initial catalyst model structure and designed new redox and associative pathways with and without redox regeneration. By modifying

the catalyst model, we could obtain a good match between the experiments and the associative carboxyl pathway with redox regeneration.

5.1. Redox Pathways

5.1.1. Classical Redox Pathway

This pathway is designed on our initial catalyst model that was depicted in Figure (5-2). The reaction steps that are considered for this pathway are:

(R1) $*_{Pt}\text{-}O_{int} + CO_{(g)} \rightarrow CO_{Pt}\text{-}O_{int}$

(R2) $CO_{Pt}\text{-}O_{int} \rightarrow CO_{2(Pt\text{-}int)}$

(R3) $CO_{2(Pt\text{-}int)} \rightarrow *_{Pt}\text{-}V_{int} + CO_{2(g)}$

(R4) $*_{Pt}\text{-}V_{int} + H_2O_{(g)} \rightarrow H_2O_{(Pt)}\text{-}V_{int}$

(R5) $H_2O_{(Pt)}\text{-}V_{int} \rightarrow H_{Pt}\text{-}OH_{int}$

(R6) $H_{Pt}\text{-}OH_{int} + *_{Pt} \rightarrow 2H_{Pt}\text{-}O_{int}$

(R7) $2H_{Pt}\text{-}O_{int} \rightarrow *_{Pt}\text{-}O_{int} + H_{2(g)} + *_{Pt}$

Figure (5-3) illustrates the energy profile for this path. The intermediate structures are shown in the inset and the transition state structures are provided in the appendix. In this path, CO adsorbs on the empty interfacial Pt site with a binding energy of -1.86 eV (R1) and then spills over to the interfacial oxygen of ceria to create an adsorbed CO_2 structure (R2). The spillover is 0.65 eV endothermic and has an activation barrier of 0.84 eV. In the next step CO_2 desorbs, creating an oxygen vacancy at the interface. The desorption process is 1.16 eV endothermic and has an activation barrier of 1.41 eV (R3).

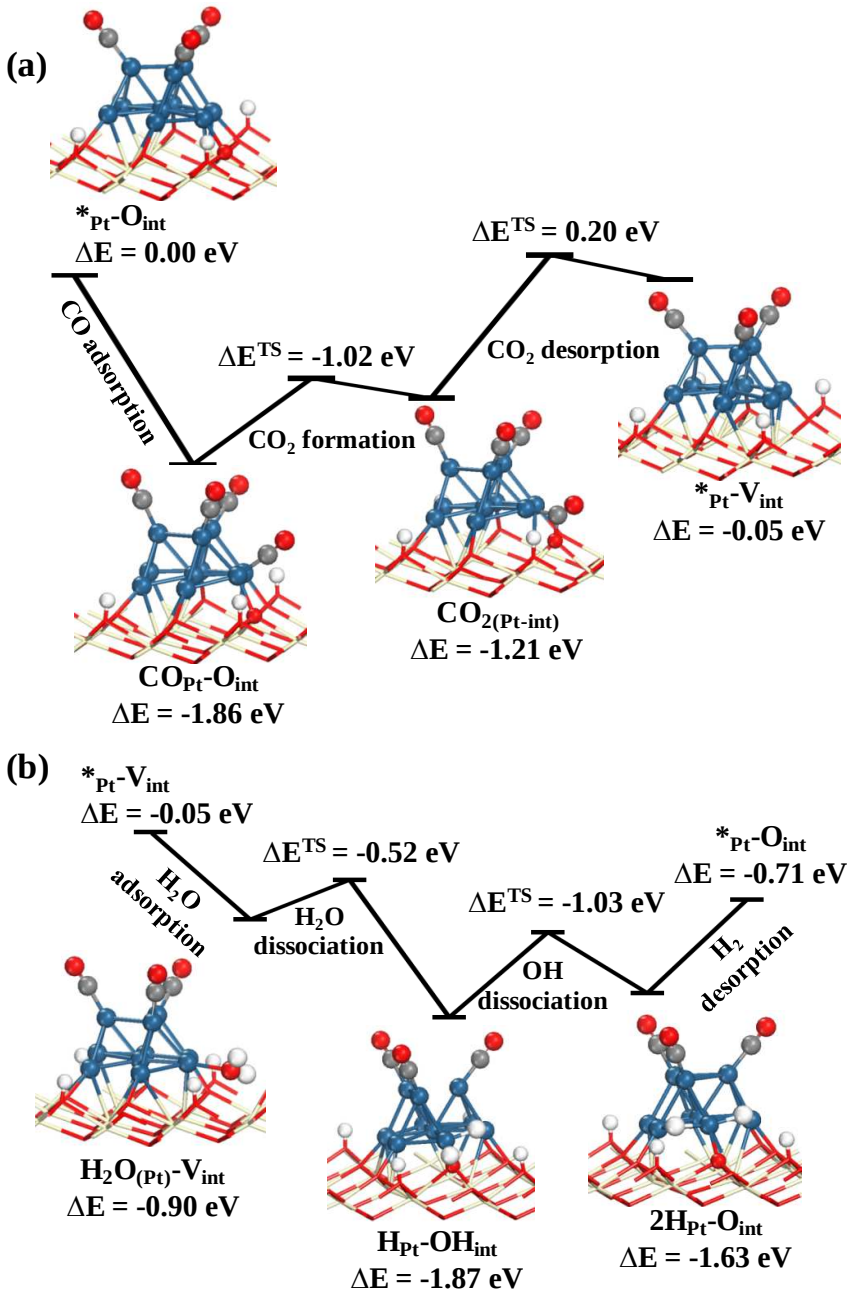

FIGURE 5-3. The energy profile for the classical redox pathway of the WGS reaction at the interface of our initial catalyst model. $*_{Pt}$ and V_{int} denote the empty site on the interfacial Pt atoms and an oxygen vacancy at the interface of Pt cluster and the ceria support, respectively. (a) first part of the redox path that is CO oxidation to CO_2. (b) second part of the redox path that is H_2O reduction to H_2.

Following the CO_2 desorption step, water adsorbs and dissociates at the interface. Our converged adsorbed water structure is not located exactly on the vacancy. Instead, water adsorbs on the interfacial platinum site that is neighboring the oxygen vacancy in a

0.85 eV exothermic process. Next, the adsorbed H_2O dissociates by transferring one H atom to the Pt cluster and forming an interfacial OH group. This process is 0.97 eV exothermic and has an activation barrier of 0.38 eV (R5). The second H transfer from –OH to the Pt cluster takes place in the following step with an activation barrier of 0.84 eV and the process is endothermic by 0.24 eV (R6). The last step is H_2 desorption from the Pt cluster (R7, ΔE = 0.92 eV) that completes the catalytic cycle.

By looking at the energy profile we did not consider entropy effects of the gas phase species which requires calculation of the Gibbs free energy. So we assumed the gas phase species to be at 1 bar and 500 K and Figure (5-4) depicts the calculated free energy profile.

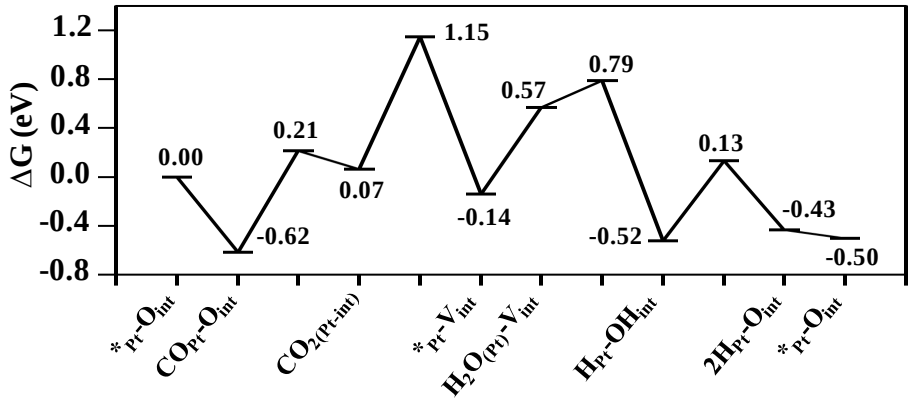

FIGURE 5-4. The Gibbs free energy profile for classical redox pathway of the WGS reaction at the Pt_{10}/CeO_2 (111) TPB (our initial catalyst model) (T = 500 K; P(gas) = 1 atm). All energies are with reference to the sum of the energies of the initial state ($*_{Pt}$-O_{int}) and the reactant gas phase molecules (CO, H_2O). For solid surfaces the zero point energy corrected energies have been considered.

In this way we have considered the rotational and translational energies of the gas phase species that are not negligible compared to their electronic energies. For solid surfaces the zero point corrected energies have been considered. The zero energy state in the profile is the sum of the energies of the initial state ($*_{Pt}$-O_{int}) and the gas phase

reactants. The profile shows CO_2 desorption has the highest barrier in the path (1.15 eV) and the adsorbed CO and dissociated water have the highest stability at the assumed gas phase condition. It is worth mentioning that by considering the gas phase species' free energies, the adsorption of CO is only 0.62 eV exergonic and adsorption of water is 0.71 eV endergonic.

The zero point corrected energies of the reaction steps and their activation barriers along with forward and reverse rate constants at 473 K have been provided in Table (5-1).

TABLE 5-1. The zero point energy corrected reaction energies and activation barriers along with kinetic parameters at 473 K for the elementary steps considered in classical redox pathway of the WGS reaction mechanism.

	ΔE^{zpc} (eV)	$E^{act,zpc}$ (eV)	k_f	k_r
R1	-1.70		1.87×10^{9}	9.91×10^{-2}
R2	0.68	0.83	8.46×10^{3}	2.64×10^{11}
R3	1.14	1.38	1.93×10^{3}	3.71×10^{6}
R4	-0.76		2.34×10^{9}	2.29×10^{9}
R5	-1.09	0.22	1.48×10^{11}	1.92×10^{-1}
R6	0.09	0.66	1.76×10^{6}	1.39×10^{8}
R7	0.80		1.42×10^{7}	7.02×10^{9}

Using the kinetic parameters for this pathway, we developed a microkinetic model as has been described in the computational method section. To compare our results with experiments, we chose two experimental studies by Phatak et al.[263] and Thinon et al.[264] Phatak and coworkers used a 1 wt% Pt/CeO_2 catalyst and the apparent activation energy and the turn over frequency were measured at 200 °C and 7% CO, 8.5% CO_2, 22% H_2O, and 37% H_2 (their assumed standard condition) with 1 atm total pressure. We note that the temperature range of 180-210 °C has been used by the authors to measure the apparent activation energy. For measuring the reaction orders of CO, CO_2, H_2, and H_2O

the standard gas phase composition was varied between 5-25% CO, 5-30% CO_2, 25-60% H_2, and 10-46% H_2O, respectively. The reported reaction orders, apparent activation energy (E^{app}) and the turn-over frequency (TOF) and the results of our redox model are presented in Table (5-2) under the experimental condition #1. Thinon and coworkers used a 1.2 wt% Pt/CeO_2 catalyst and conducted the kinetic study in the temperature range of 150-400 °C and 1 atm total pressure. In their study, the gas composition was varied over the range 1-20% CO, 1-20% CO_2, 5-25% H_2O, and 5-40% H_2. The apparent activation barrier and the turn over frequency have been measured at 300 °C and 10% CO, 10% CO_2, 20% H_2O, and 40% H_2. The results of these studies along with our redox model results are presented in Table (5-2) under the experimental condition #2.

TABLE 5-2. Reaction orders (n_i), apparent activation energies (E^{app}), and turn over frequencies (TOF) from microkinetic model for the classical redox pathway at different experimental conditions.

	Experimental condition #1 (P_{CO}=0.07, P_{CO2}=0.085, P_{H2O}=0.22, P_{H2}=0.37 atm; T = 473 K)		**Experimental condition #2** (P_{CO}=0.1, P_{CO2}=0.1, P_{H2O}=0.2, P_{H2}=0.4 atm; T = 573 K)	
	Model	**Experiment** [a]	**Model**	**Experiment** [b]
$\mathbf{n_{CO}}$	0.00	-0.03	0.00	0.14
$\mathbf{n_{H2O}}$	0.00	0.44	0.00	0.66
$\mathbf{n_{CO2}}$	0.00	-0.09	0.00	-0.08
$\mathbf{n_{H2}}$	0.00	-0.38	0.00	-0.54
TOF (s^{-1})	6.18×10^{-5}	4.14×10^{-2}	0.36	0.2
E^{app} (eV)[c]	2.04	0.78	2.02	0.94

[a] see reference (263)
[b] see reference (264)
[c] Apparent activation energies are calculated in the temperature ranges of 373-573 K and 423-673 K for the experimental condition #1 and the experimental condition #2, respectively.

It is clear that this model for the Redox path does not provide a good match with the experimental results. After analyzing the path with Campbell's degree of rate control and the degree of thermodynamic rate control, CO_2 desorption was the rate limiting step

and adsorbed CO had the highest coverage of almost one. Motivated by the high coverage of adsorbed CO we studied "CO-promoted" pathways starting from the adsorbed CO structure and considering the second CO adsorption on the same site. Our aim is basically to see if the CO_2 desorption transition state would be stabilized or not to improve the rate.

5.1.2. Redox Pathways with CO-Promotion and H_2O-Dissociation On Pt

In this section we discuss three possible pathways. The first one is a CO promoted redox pathway and the other two are the associative carboxyl and formate routes with redox regeneration that have been suggested for the WGS reaction at the three-phase boundary of metal-reducible oxide catalysts.[235, 236] Here, the interfacial OH group can be activated by an adsorbed CO to create carboxyl and formate species. The first part of these pathways is the same that is CO-assisted CO_2 desorption and water adsorption and dissociation at the interface. Our aim for considering CO-assistance is, as mentioned before, to stabilize the CO_2 desorption transition state of the simple redox pathway that had a very high energy in the path (see Figure (5-4)) to see if we would get a better rate or not. The energy and free energy profiles for this first part have been shown in Figure (5-5) and the reaction steps are as follows. After first CO spill over (R2),

(R8) $CO_{2(Pt\text{-}int)} + *_{Pt} + CO_{(g)} \rightarrow CO_{Pt}\text{-}CO_{2(Pt\text{-}int)}$

(R9) $CO_{Pt}\text{-}CO_{2(Pt\text{-}int)} \rightarrow CO_{Pt}\text{-}V_{(int)} + *_{Pt} + CO_{2(g)}$

(R10) $CO_{Pt}\text{-}V_{int} + H_2O_{(g)} \rightarrow CO_{Pt}\text{-}H_2O_{(int)}$

(R11) $CO_{Pt}\text{-}H_2O_{(int)} + *_{Pt} \rightarrow CO_{Pt}\text{-}H_{Pt}\text{-}OH_{int}$

A second CO adsorbs in a 2.22 eV exothermic process (R8) that is stronger than the first CO adsorption (1.86 eV). The next step is CO_2 desorption that is 0.52 eV endothermic and has an activation barrier of 1.32 eV (R9). Comparing the free energies of the redox path (Figure 5-4) and the CO-assisted CO_2 desorption path (Figure 5-5a), CO_2 desorption is exergonic by 0.88 eV in the latter one while it is 0.21 eV exergonic in the former path. The transition state for CO_2 desorption has been stabilized in the presence of the additional CO at the interface compared to the starting structure of each pathway as we initially aimed to. However, at the same time the second CO adsorption is very strong that we would expect to lower the rate. After the creation of the vacancy at the interface in the presence of the promotional CO, water adsorbs there and dissociates. The adsorption of water is 0.54 eV exothermic (R10) and when we consider the Gibbs free energies the adsorption is 1.00 eV endergonic; compared to the redox pathway the adsorption is by 0.29 eV more endergonic. After water adsorption, it dissociates to the interfacial platinum in a 0.62 eV exergonic process and a free energy barrier of 0.19 eV. Presence of the promotional CO has almost no effect on the barrier for water dissociation. However, due to CO promotion, the free energy gain of the reaction step has been reduced by 0.47 eV.

In the CO promoted redox pathway the interfacial –OH group directly dissociates to the Pt cluster and the next step is dihydrogen desorption. In the associative carboxyl and formate routes with redox regeneration the interfacial –OH group activates with the promotional CO to create carboxyl or formate species. Figure (5-5b) depicts the Gibbs free energy of the CO promoted redox pathway from water dissociation to H_2 desorption (red line). The energy profiles for the activation of the interfacial OH group with the

adsorbed CO for carboxyl and formate formation have also been provided (blue and green lines, respectively).

The reaction steps that have been considered are as follows:

(R12) $CO_{Pt}\text{-}H_{Pt}\text{-}OH_{int} + *_{Pt} \rightarrow CO_{Pt}\text{-}2H_{Pt}\text{-}O_{int}$

(R13) $CO_{Pt}\text{-}2H_{Pt}\text{-}O_{int} \rightarrow CO_{Pt}\text{-}O_{int} + H_{2(g)} + 2*_{Pt}$

(R14) $CO_{Pt}\text{-}H_{Pt}\text{-}OH_{int} \rightarrow COOH_{(Pt\text{-}int)}\text{-}H_{Pt}$

(R15) $CO_{Pt}\text{-}H_{Pt}\text{-}OH_{int} \rightarrow CHO_{(vert,Pt)}\text{-}O_{int}\text{-}H_{Pt}$

(R16) $CHO_{(vert,Pt)}\text{-}O_{int}\text{-}H_{Pt} \rightarrow CHO_{(horiz,Pt)}\text{-}O_{int}\text{-}H_{Pt}$

(R17) $CHO_{(horiz,Pt)}\text{-}O_{int}\text{-}H_{Pt} \rightarrow HCOO_{(Pt,int)}\text{-}H_{Pt}$

Figure (5-5b) clearly illustrates that creation of both carboxyl and formate have high barriers of 1.79 and 1.65 eV, respectively. For creating formate first we need to produce a formyl intermediate by dissociating the interfacial OH group to the carbon of the adsorbed CO. Due to higher barriers of carboxyl and formate formation compared to direct dissociation of the interfacial OH group to the Pt cluster, we did not close these cycles since the rate of these pathways would be much lower compared to the CO-promoted redox route.

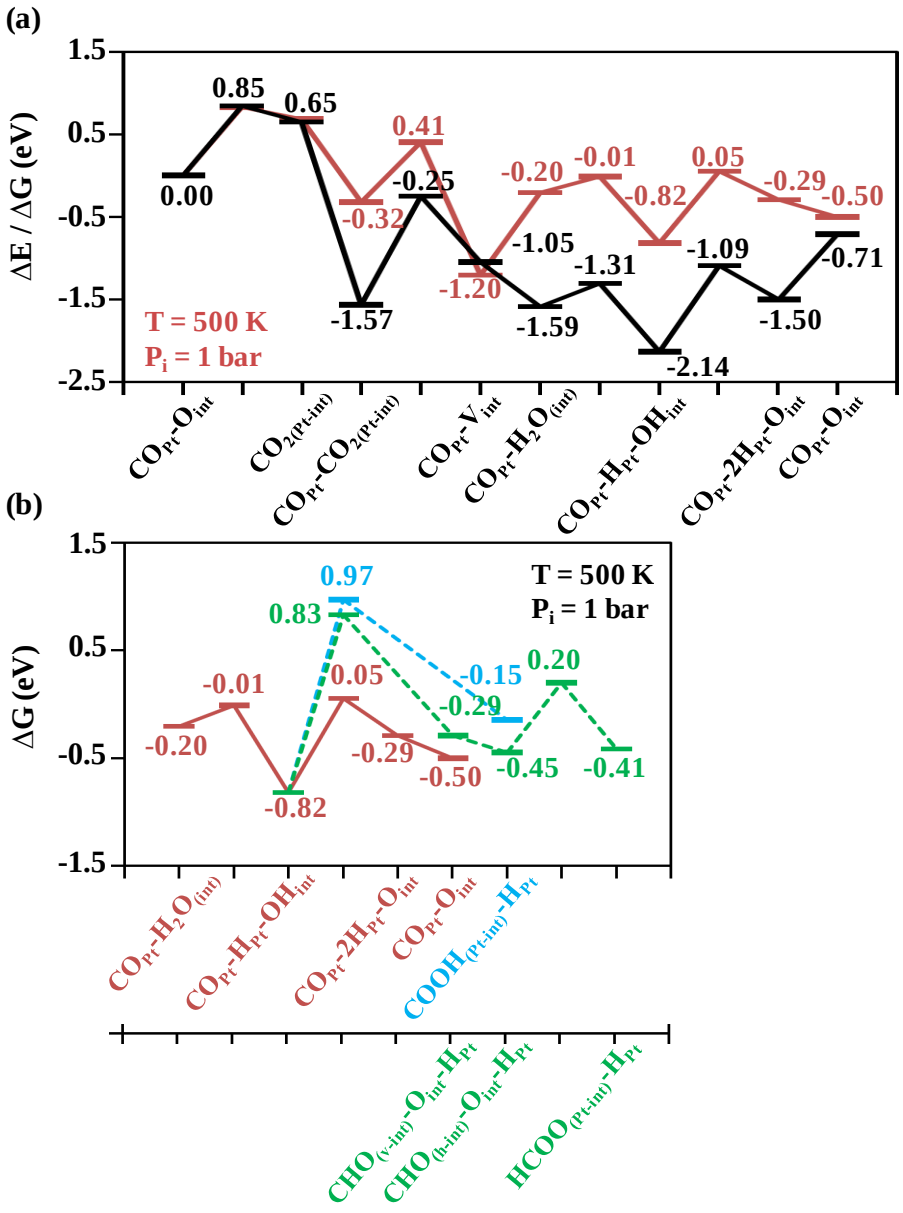

FIGURE 5-5. (a) The (free) energy profile for the CO-promoted redox pathway with water dissociation to Pt, (b) the free energy profile for H_2O dissociation and reduction to H_2 in the redox path compared to formate and carboxyl formation from CO_{Pt}-H_{Pt}-OH_{int} (red, green, and blue lines, respectively) (T = 500 K, P_i = 1 atm).

For the CO-promoted redox route (red line), the interfacial –OH group dissociates to Pt that is 0.53 eV endergonic and has a free energy barrier of 0.87 eV (R12). For this reaction step, the barrier has increased by 0.22 eV due to the presence of the co-adsorbed CO at the interface and the reaction step is more endergonic by 0.44 eV. The final step to

close this cycle is H_2 desorption and this process is 0.21 eV exergonic (R13). Comparing this reaction step with the similar step in the redox path, H_2 desorption from the Pt cluster is more exergonic in the presence of the co-adsorbed CO at the interface by 0.14 eV. The structures for the intermediates of the described pathways have been provided in Figure (5-6). The transition state structures are provided in the appendix.

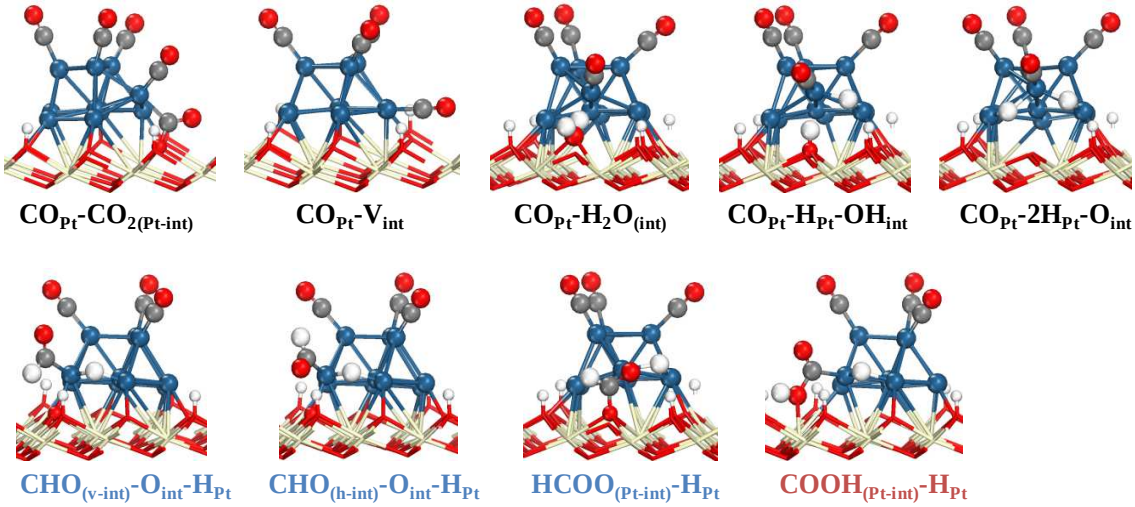

FIGURE 5-6. The new intermediates structures for the CO promoted pathways

The results of our microkinetic model for the CO promoted redox route have been provided in Table (5-3) along with the previously described Redox route. The kinetic parameters for this pathway have been provided in Table (5-4). The microkinetic result for the redox path has already been discussed. For the CO promoted redox pathway, our calculated CO reaction order is 1, the H_2 reaction order is -1, and the H_2O and CO_2 reaction orders are zero. Compared to the redox pathway and the experimental results, we could get a negative reaction order for H_2 by considering the lateral interaction of the promotional CO at the interface. However, the calculated apparent activation barrier is 1.92 eV which is 1.14 eV larger compared to the experimental result and the turn over frequency is 4 orders of magnitude slower. Consequently, this model pathway, like the

redox pathway, is not a good model. We also calculated the degree of thermodynamics rate control for this pathway. The result shows that the dissociated water is the most important reaction intermediate. Next, Campbell's degree of rate control showed that the second CO adsorption is the rate limiting step in this CO promoted pathway.

TABLE 5-3. Reaction orders (n_i), apparent activation energy (E^{app}), turn over frequency (TOF) for classical redox and CO-promoted redox in the experimental condition #1.

	n_{H2O}	n_{CO}	n_{H2}	n_{CO2}	E^{app} (eV)	TOF (1/s)
Experiment	0.44	-0.03	-0.38	-0.09	0.78	4.14×10^{-2}
Classical Redox	0	0	0	0	2.04	6.18×10^{-5}
CO Promoted Redox Pathway	0	1	-1	0	1.92	2.33×10^{-6}

TABLE 5-4. The zero point corrected reaction energies and activation barriers along with kinetic parameters at 473 K for the elementary steps considered in the CO-promoted redox pathway of the WGS reaction mechanism.

	ΔE^{zpc} (eV)	$E^{act,zpc}$ (eV)	k_f	k_r
R12	-2.09		1.87×10^{9}	3.59×10^{-5}
R13	0.46	1.26	4.15×10^{4}	4.38×10^{0}
R14	-0.46		2.34×10^{9}	1.86×10^{12}
R15	-0.62	0.19	3.80×10^{10}	2.44×10^{4}
R16	0.53	0.87	6.29×10^{3}	3.78×10^{9}
R17	0.65		8.69×10^{8}	7.02×10^{9}

5.1.3. Redox Pathways with CO-Promotion and H_2O-Dissociation on O_s

In this pathway, after the creation of an oxygen vacancy at the interface in the presence of the promotional CO, water adsorbs and dissociates on the vacancy to give one hydrogen to the nearby surface oxygen and an –OH group to the interfacial oxygen vacant site. For transferring the hydrogen atoms back to the metal, first we dissociated the interfacial OH group to the Pt. Next, we noticed that the diffusion of hydrogen from surface oxygen to the interfacial oxygen is a difficult process. So, we investigated a water assisted hydrogen

transfer. The phenomenon of water-mediated proton hopping has been studied experimentally on iron oxide surface.[265] The reactions that have been considered are as follows:

(R18) $CO_{Pt}\text{-}H_2O_{(int)} + O_s \rightarrow CO_{Pt}\text{-}OH_s\text{-}OH_{int}$

(R19) $CO_{Pt}\text{-}OH_s\text{-}OH_{int} + *_{Pt} \rightarrow CO_{Pt}\text{-}H_{Pt}\text{-}O_{int}\text{-}OH_s$

(R20) $CO_{Pt}\text{-}H_{Pt}\text{-}O_{int}\text{-}OH_s + *_{Ce} + H_2O_{(g)} \rightarrow CO_{Pt}\text{-}H_{Pt}\text{-}O_{int}\text{-}H_2O_{(Ce)}\text{-}OH_s$

(R21) $CO_{Pt}\text{-}H_{Pt}\text{-}O_{int}\text{-}H_2O_{(Ce)}\text{-}OH_s \rightarrow CO_{Pt}\text{-}H_{Pt}\text{-}OH_{int}\text{-}OH_{Ce}\text{-}OH_s$

(R22) $CO_{Pt}\text{-}H_{Pt}\text{-}OH_{int}\text{-}OH_{Ce}\text{-}OH_s \rightarrow CO_{Pt}\text{-}H_{Pt}\text{-}OH_{int}\text{-}H_2O_{(Ce)}\text{-}O_s$

(R23) $CO_{Pt}\text{-}H_{Pt}\text{-}OH_{int}\text{-}H_2O_{(Ce)}\text{-}O_s \rightarrow CO_{Pt}\text{-}H_{Pt}\text{-}OH_{int} + O_s + *_{Ce} + H_2O_{(g)}$

The energy and free energy profiles for these reaction steps are provided in Figure (5-7). The structures of reaction intermediates have been provided in Figure (5-8) and the transition state structures are provided in the appendix. Here, water dissociation at the surface-interface has an activation barrier of 0.27 eV which is almost the same as for water directly dissociating on the Pt site. However, water dissociation to the surface oxygen is more exothermic by 0.5 eV. Since during microkinetic analysis of the previous CO-promoted pathway, dissociated water to Pt ($CO_{Pt}\text{-}OH_{int}\text{-}H_{Pt}$) was the most important reaction intermediate with a coverage of almost one, we might expect that with water dissociation to the surface-interface and creation of a more stable $CO_{Pt}\text{-}OH_{int}\text{-}OH_s$ intermediate we obtain a lower rate than 10^{-6}. Consequently, this model pathway would also not play any role during the WGS reaction. After water dissociation to the surface-interface, dissociation of the interfacial OH group to the Pt is endothermic by 0.41 eV

and has a 0.89 eV activation barrier. Next, for water assisted hydrogen transfer, the adsorption of water is very weak on ceria surface with a binding energy of 0.11 eV. However, when water dissociates it creates a more stable species: one extra mono-coordinated OH group is located on the Ce atom and the hydrogen of water that is dissociated to the interfacial oxygen (CO_{Pt}-H_{Pt}-OH_{int}-OH_{Ce}-OH_s). This reaction is 0.52 eV exothermic and has a barrier of 0.27 eV. After that, water forms from the extra mono-coordinated –OH group on Ce and the hydrogen of the surface –OH group. This process is almost thermo-neutral, ΔE = -0.10 eV, and has a barrier of 0.19 eV. Next, water desorbs that is 0.82 eV endothermic which closes the process of hydrogen transfer from surface oxygen to the interface oxygen.

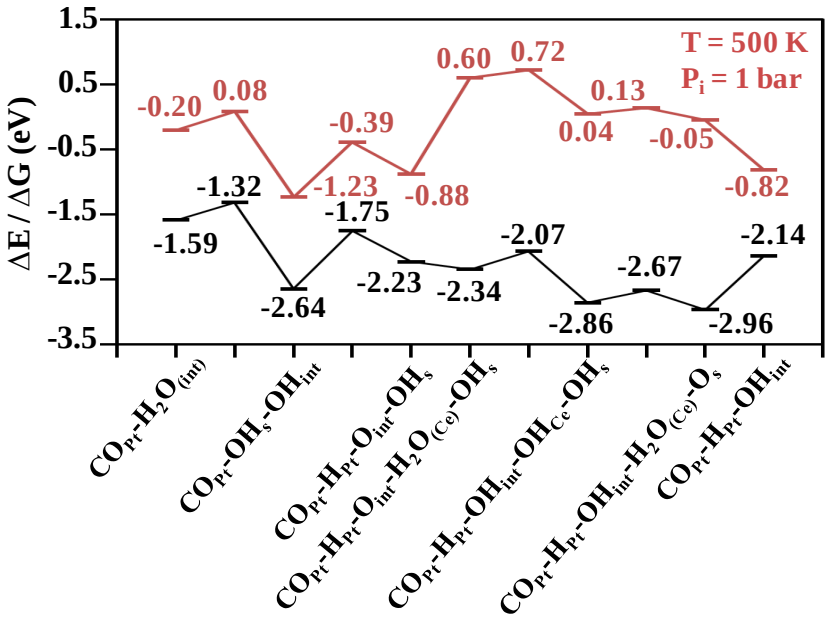

FIGURE 5-7. The (free) energy profile for bringing hydrogens from surface and interface oxygens to the interface and Pt in the CO-promoted pathway with water dissociation to O_s, using water assisted hydrogen transfer. All the energies are with reference to the sum of the energies of (CO_{Pt}-O_{int}) and (CO,H_2O) gas phase molecules (see Figure (5-5)).

Analyzing the free energy profile, water adsorption is 1.48 eV endergonic and water desorption is 0.77 eV exergonic. For all other reaction steps the difference between the energy and free energy profile is negligible.

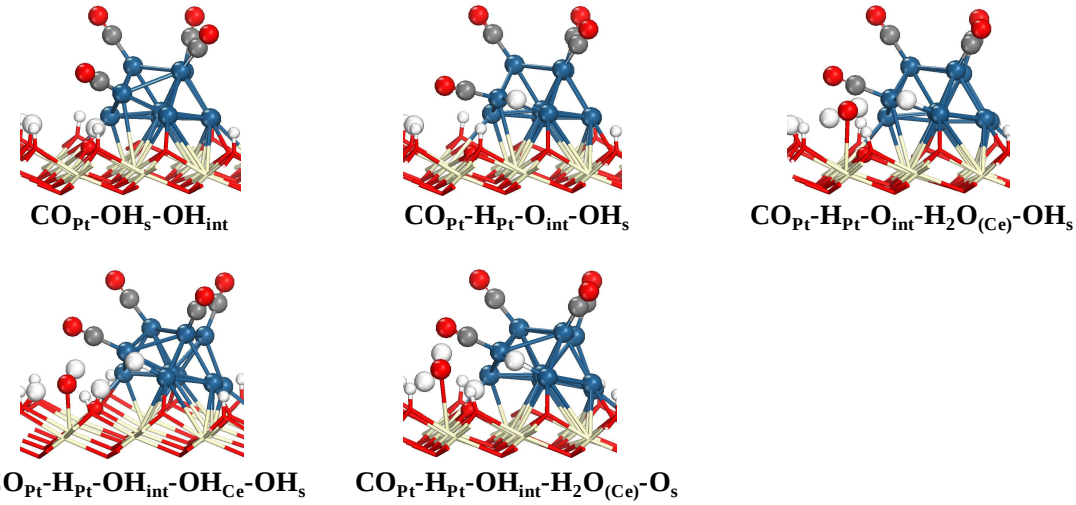

FIGURE 5-8. The intermediate structures for water dissociation to the surface-interface and bringing hydrogens from surface and interface oxygens to the interface oxygen and Pt in the CO-promoted pathway with water dissociation to O_s, using water assisted hydrogen transfer

The kinetic parameters for the explained reaction steps have been provided in Table (5-5).

TABLE 5-5. The zero point corrected reaction energies and activation barriers along with kinetic parameters at 473 K for the new elementary steps considered for CO-promoted redox pathway with water dissociation to the surface-interface.

	ΔE^{zpc} (eV)	$E^{act,zpc}$ (eV)	k_f	k_r
R18	-1.03	0.28	1.22×10^{10}	1.22×10^{-2}
R19	0.35	0.85	4.07×10^{3}	4.05×10^{7}
R20	0.02		2.34×10^{9}	3.23×10^{17}
R21	-0.56	0.12	6.10×10^{11}	7.38×10^{5}
R22	-0.09	0.09	8.19×10^{11}	6.87×10^{10}
R23	0.69		5.07×10^{8}	2.34×10^{9}

The microkinetic model suggests, in agreement with our prediction based on relative stability of CO_{Pt}-OH_{int}-OH_s and CO_{Pt}-H_{Pt}-OH_{int}, a very low rate, 3.64×10^{-12} 1/s,

and high activation barrier of 2.24 eV for this pathway while the reaction rate orders remained unchanged to the previous mechanism. Consequently, this model pathway is not able to explain the experimental observations.

5.2. CO-Promoted Associative Carboxyl Pathway

Theoretical investigations suggested the occurrence of the associative carboxyl pathway on Pt and Cu metal sites and also at the interface of Au cluster on ceria (111) surfaces. As discussed before, this pathway, in contrast to the redox pathways, does not involve the creation of an oxygen vacancy during the catalytic cycle and CO is oxidized directly with the oxygen of water. Since in the CO promoted model pathways we observed a strong CO adsorption at the metal-oxide interface we studied the associative carboxyl pathway in the presence of a promotional (interfacial) CO molecule.

The new reaction steps that we have considered for this pathway are depicted in equations (R24) to (R29):

(R24) $CO_{Pt}\text{-}O_{int} + H_2O_{(g)} + *_{Ce} \rightarrow CO_{Pt}\text{-}H_2O_{(Ce)}\text{-}O_{int}$

(R25) $CO_{Pt}\text{-}H_2O_{(Ce)}\text{-}O_{int} + O_s \rightarrow CO_{Pt}\text{-}OH_{Ce}\text{-}O_{int}\text{-}OH_s$

(R26) $CO_{Pt}\text{-}OH_{Ce}\text{-}O_{int}\text{-}OH_s \rightarrow COOH_{Pt}\text{-}O_{int}\text{-}OH_s + *_{Ce}$

(R27) $COOH_{Pt}\text{-}O_{int}\text{-}OH_s \rightarrow CO_{2(Pt)}\text{-}OH_{int}\text{-}OH_s$

(R28) $CO_{2(Pt)}\text{-}OH_{int}\text{-}OH_s \rightarrow *_{Pt}\text{-}OH_{int}\text{-}OH_s + CO_{2(g)}$

(R29) $*_{Pt}\text{-}OH_{int}\text{-}OH_s + CO_{(g)} \rightarrow CO_{Pt}\text{-}OH_{int}\text{-}OH_s$

Reactions (R19-23) and (R12-13) are also needed to close the WGS cycle. Figure (5-9) depicts the energy and free energy profile for these reaction steps. Figure (5-10) depicts the new intermediate structures.

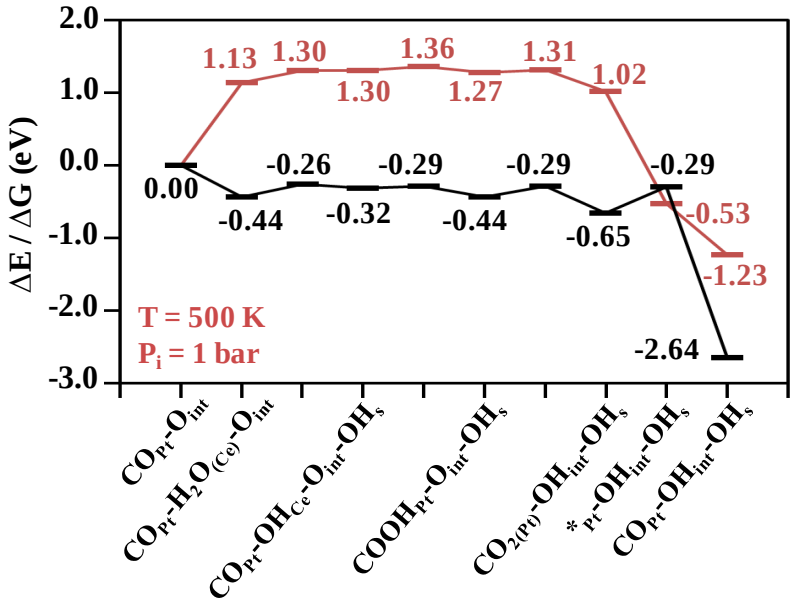

FIGURE 5-9. The (free) energy profile for the new reaction steps that we have been considered for the CO-promoted associative carboxyl pathway

After water adsorption on Ce (R24) which is exothermic by 0.44 eV (ΔG^{ads} = 1.13 eV), water dissociates on the surface oxygen (O_s). This process is 0.12 eV endothermic with a 0.18 eV activation barrier. The next step is carboxyl formation that is 0.12 eV exothermic and has an activation barrier of only 0.03 eV. After *cis*- to *trans*-transformation of the carboxyl species, the transformed carboxyl species dissociates to the interfacial oxygen. This process is 0.21 eV exothermic and has a 0.15 eV activation barrier. The next step is CO_2 desorption that is 0.36 eV endothermic (ΔG^{des} = -1.55 eV); followed by CO adsorption with a 2.35 eV binding energy (ΔG^{ads} = -0.70 eV). To complete the cycle surface, the interface hydrogen atoms should be transferred to Pt and

desorb as H_2. The energetics of these reaction steps have already been explained in the previous sections (see Figures (5-7) and (5-5)).

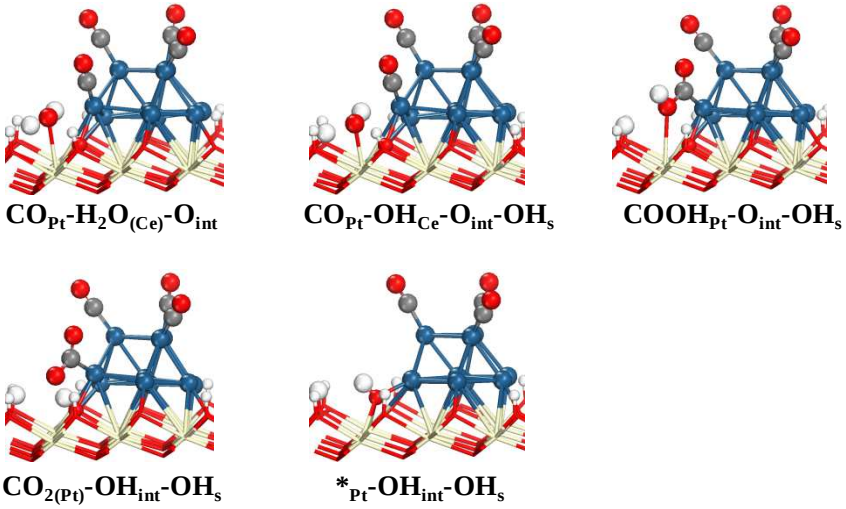

FIGURE 5-10. The new intermediates structures for the CO-promoted associative carboxyl pathway

The zero point corrected reaction energies of the described elementary steps and their activation barriers along with their forward and reverse rate constants at 473 K have been provided in Table (5-6). The results of a microkinetic modeling study at experimental conditions #1 have been provided in Table (5-7).

TABLE 5-6. The zero point corrected reaction energies and activation barriers along with kinetic parameters at 473 K for the new elementary steps considered for CO-promoted associative carboxyl pathway

	ΔE^{zpc} (eV)	$E^{act,zpc}$ (eV)	k_f	k_r
R24	-0.33		2.34×10^{9}	3.90×10^{13}
R25	0.17	0.16	1.92×10^{11}	4.02×10^{12}
R26	-0.03	0.06	5.79×10^{11}	7.20×10^{11}
R27	-0.25	0.04	2.57×10^{12}	4.91×10^{9}
R28	-0.20		3.05×10^{22}	1.50×10^{9}
R29	-1.79		1.87×10^{9}	2.31×10^{0}

TABLE 5-7. Reaction orders (n_i), apparent activation energies (E^{app}), and turn over frequencies (TOF) from microkinetic model for the CO-promoted associative carboxyl pathway at experimental condition #1

	Experimental condition #1 (P_{CO}=0.07, P_{CO2}=0.085, P_{H2O}=0.22, P_{H2}=0.37 atm; T = 473 K)	
	Model	**Experiment** [a]
$\mathbf{n_{CO}}$	0.00	-0.03
$\mathbf{n_{H2O}}$	1.00	0.44
$\mathbf{n_{CO2}}$	0.00	-0.09
$\mathbf{n_{H2}}$	-1.00	-0.38
TOF (s^{-1})	2.21×10^{-7}	4.14×10^{-2}
$\mathbf{E^{app}}$ **(eV)**[b]	1.49	0.78

[a] see reference (263)
[b] Apparent activation energy is calculated in the temperature ranges of 423-523 K.

Generally, no considerable improvement can be observed compared to the previous model pathways except that the reaction orders all display correct trends: positive reaction order for H_2O, negative reaction order for H_2, and zero reaction orders for CO and CO_2. The apparent activation barrier is still too high and the rate is too low.

Next, we calculated Campbell's degree of rate and thermodynamic control. The carboxyl formation degree of rate control was 0.69 while carboxyl dissociation and water dissociation appeared next with 0.19 and 0.10 degrees of rate control, respectively. Intermediate CO_{Pt}-OH_{int}-OH_s was the most important reaction intermediate with Campbell's degree of thermodynamics rate control of -1.00.

All these results clearly indicate the presence of strongly adsorbed CO at the interfacial Pt site under all experimental conditions considered here. The low rates and high apparent activation barriers predicted by our microkinetic model of all possible pathways suggest that not all CO molecules adsorbed at the interfacial sites are reactive,

especially in the low temperature range, 423 K-673 K, considered here. However, the presence of CO at one interfacial site could assist the WGS reaction at the neighboring interface site by reducing the CO adsorption strength. Thus, we considered a new model with a CO molecule adsorbed at the bridging site of the interfacial Pt atoms and investigated the CO-assisted reaction pathways at the neighboring site in the following section. The structure of this new model ($*_{Pt}$-CO_{Pt}-O_{int}) is provided in Figure (5-11). We note here that the CO adsorption at this bridging site is about 0.4 eV stronger than at the linear position we considered earlier which again confirms that the interfacial CO in this new model (Figure 5-11) will not be reactive at low temperatures.

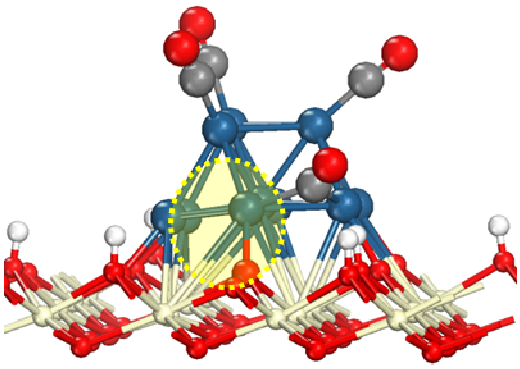

FIGURE 5-11. Modified Pt_{10}/CeO_2 (111) catalyst model for studying the WGS reaction mechanisms that involve creation of vacancy during the cycle. In this model $*_{Pt}$-CO_{Pt}-O_{int} is the active site while $*_{Pt}$ refers to the interfacial bridging site of Pt cluster.

5.3. New Pathways based on Modified Model Catalyst

5.3.1. Redox Pathway – Model II

The following reaction steps have been considered for the redox pathway on our new model:

(R30) $*_{Pt}$-CO_{Pt}-O_{int} + $CO_{(g)}$ → $2CO_{Pt}$-O_{int}

(R31) $2CO_{Pt}$-O_{int} → $CO_{2(Pt\text{-}int)}$-CO_{Pt}

(R32) $CO_{2(Pt\text{-}int)}\text{-}CO_{Pt} \rightarrow *_{Pt}\text{-}CO_{Pt}\text{-}V_{int} + CO_{2(g)}$

(R33) $*_{Pt}\text{-}CO_{Pt}\text{-}V_{int} + H_2O_{(g)} \rightarrow *_{Pt}\text{-}CO_{Pt}\text{-}H_2O_{(int)}$

(R34) $*_{Pt}\text{-}CO_{Pt}\text{-}H_2O_{(int)} \rightarrow CO_{Pt}\text{-}H_{Pt}\text{-}OH_{int}$

(R35) $CO_{Pt}\text{-}H_{Pt}\text{-}OH_{int} + *_{Pt} \rightarrow CO_{Pt}\text{-}2H_{Pt}\text{-}O_{int}$

(R36) $CO_{Pt}\text{-}2H_{Pt}\text{-}O_{int} \rightarrow *_{Pt}\text{-}CO_{Pt}\text{-}O_{int} + H_{2(g)} + *_{Pt}$

The energy profile for this pathway has been provided in Figure (5-12) starting from our new catalyst model. The first step for this cycle is CO adsorption on the neighboring bridge site with a binding energy of -1.20 eV (R30). Then, CO spills over to the interfacial oxygen of ceria and creates an adsorbed CO_2 structure (R31). The spillover is 0.23 eV exothermic and has an activation barrier of 0.54 eV. In the next step, CO_2 desorbs to create an oxygen vacancy at the interface. The desorption process is 0.95 eV endothermic and has an activation barrier of 1.19 eV (R32).

After creation of an oxygen vacancy at the interface water adsorbs and dissociates at the vacant site. Both reactions are exothermic by 0.57 eV and 0.50 eV, respectively. The barrier for water dissociation is 0.51 eV (R34). The following step is the second H transfer from the interfacial –OH to the Pt with an activation barrier of 1.07 eV. This process is endothermic by 0.42 eV (R35). The final step to close the cycle is desorption of H_2 from the Pt cluster (R36) that is 0.42 eV endothermic.

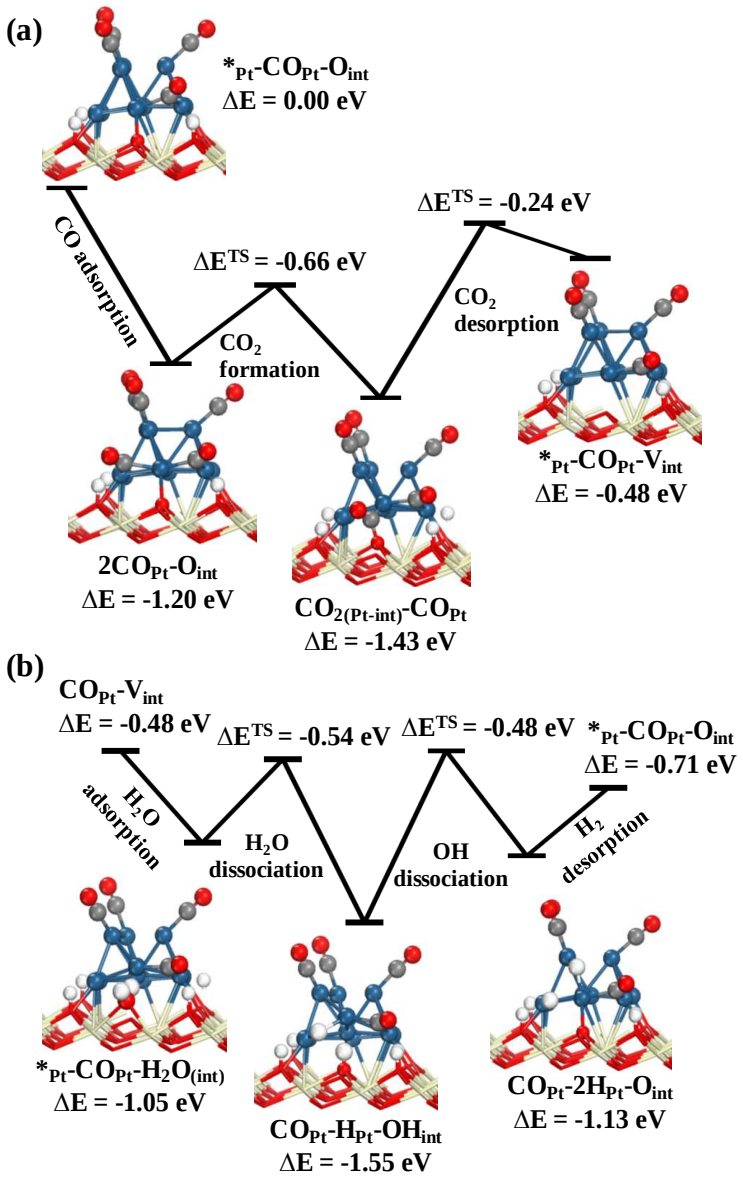

FIGURE 5-12. The energy profile for the redox pathway of the WGS reaction at the interface of our modified catalyst model (redox pathway (I) – model II) (a) first part of the path that is CO oxidation to CO_2. (b) second part of the path that is H_2O reduction to H_2. The zero energy state in the profile is the sum of the energies of the initial state ($*_{Pt}$-CO_{Pt}-O_{int}) and the gas phase reactants.

Comparison of this redox pathway energy profile (Figure 5-12) with that of our earlier model with one linear CO (Figure 5-3) suggests that the CO adsorption is reduced by about 0.6 eV (-1.20 eV Vs -1.86 eV) and the oxygen vacancy formation is more exothermic by about 0.4 eV (-0.48 eV Vs -0.05 eV) in the presence of an additional CO

molecule. The water dissociation process seems to have similar energetics with both models, but the second H-transfer from the interface –OH to Pt (R35) seems to have a high activation barrier of more than 1 eV in the presence of an additional CO molecule. Although, this model seems to take care of some of the difficulties associated with our earlier model, we will show below that some very stable intermediate structures are not included in this redox pathway that decrease its activity. Since all our earlier calculations predicted that the CO adsorption on the interfacial Pt atoms is very strong under many different environments, in the following section we have considered the possibility of adding another CO molecule whenever the active site becomes empty.

5.3.2. Second Possibility in Redox Pathway – Model II

In the redox cycle explained in the previous section (Figure 5-12), the CO_2 desorption process creates an oxygen vacancy at the interface as well as an empty Pt site. A direct H_2O dissociation at the oxygen vacancy followed by H-transfer to this empty site were considered in this process. However, the presence of an oxygen vacancy at the interface could also promote a strong adsorption of CO at the neighboring Pt atoms. Thus, we considered the adsorption of another CO molecule at this empty Pt site ($*_{Pt}$-CO_{Pt}-V_{int}) in this section prior to H_2O adsorption and dissociation. The reaction steps considered in this section (redox pathway (II) – model II) are as follows:

(R37) $*_{Pt}\text{-}CO_{Pt}\text{-}V_{int} + CO_{(g)} \rightarrow 2CO_{Pt}\text{-}V_{int}$

(R38) $2CO_{Pt}\text{-}V_{int} + H_2O_{(g)} \rightarrow 2CO_{Pt}\text{-}H_2O_{(int)}$

(R39) $2CO_{Pt}\text{-}H_2O_{(int)} + *_{Pt} \rightarrow 2CO_{Pt}\text{-}H_{Pt}\text{-}OH_{int}$

(R40) $2CO_{Pt}\text{-}H_{Pt}\text{-}OH_{int} + *_{Pt} \rightarrow 2CO_{Pt}\text{-}2H_{Pt}\text{-}O_{int}$

(R41) $2CO_{Pt}\text{-}2H_{Pt}\text{-}O_{int} \rightarrow 2CO_{Pt}\text{-}O_{int} + H_{2(g)} + 2*_{Pt}$

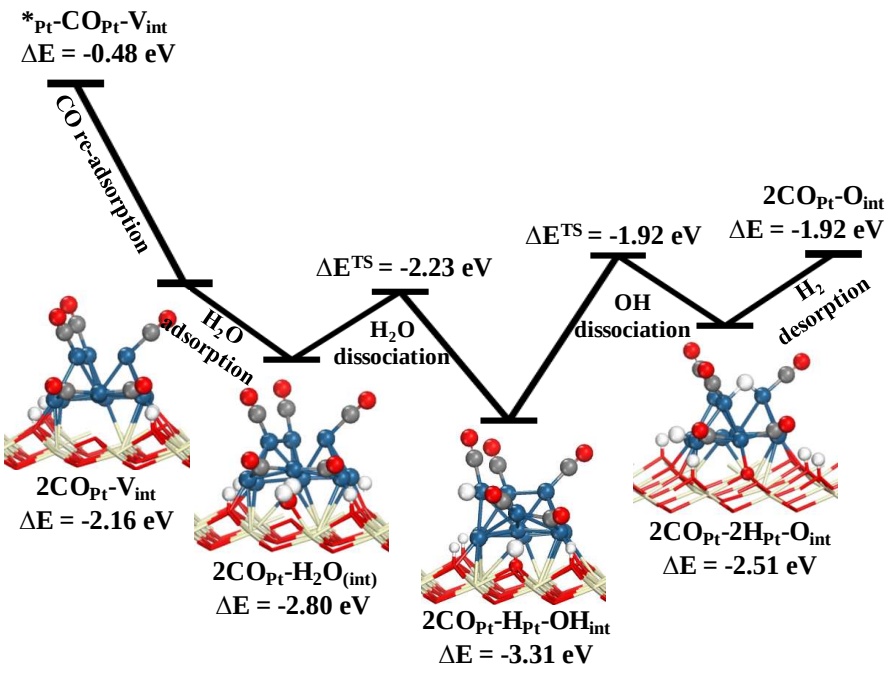

FIGURE 5-13. The energy profile for the second possibility in the classical redox pathway of the WGS reaction derived from modified catalyst model (redox pathway (II) – model II). The zero energy state in the profile is the sum of the energies of the initial state ($*_{Pt}$-CO_{Pt}-O_{int}) and (CO,H_2O) in the gas phase.

Figure (5-13) depicts the energy profile for these steps. As expected, CO adsorbs strongly at the empty interfacial Pt site in the presence of an oxygen vacancy with an adsorption energy of -1.68 eV (R37). Then, water adsorbs on the vacancy and dissociates in 0.64 and 0.51 eV exothermic processes, respectively. The barrier for water dissociation is 0.57 eV (R39). Following water dissociation, the interfacial –OH group dissociates which is a 0.80 eV endothermic process that has a barrier of 1.39 eV (R40). The final step to close the cycle is H_2 desorption which is 0.59 eV endothermic (R41).

Here again, the transfer of hydrogen from the interface oxygen to the Pt cluster (R40) seems to be a difficult process. The energy profile clearly indicates that the reaction might proceed through second CO adsorption (downhill) at the empty Pt site

(R37) instead of direct H_2O dissociation (R33-R36). On the other hand, the presence of an additional CO molecule at the interface Pt prohibits the transfer of H-atoms from the interface oxygen to the Pt cluster. In order to overcome this difficulty, we considered the possibility of transferring the H atom through the formation of an associative carboxyl intermediate in the following section.

5.3.3. Associative Carboxyl Pathway with Redox Regeneration – Model II

In the redox pathway (II) – model II, it is possible for the adsorbed water at the interface ($2CO_{Pt}$-$H_2O_{(int)}$) to dissociate to the surface oxygen to create ($2CO_{Pt}$-OH_{int}-OH_s).

(R42) $2CO_{Pt}\text{-}H_2O_{(int)} + O_s \rightarrow 2CO_{Pt}\text{-}OH_{int}\text{-}OH_s$

This process is 1.13 eV exothermic and has a barrier of 0.19 eV. Compared to water dissociation to Pt (R39), water dissociation to O_s is more exothermic by 0.62 eV and has a smaller activation barrier by 0.38 eV. Thus, we can expect that this process would have a higher rate. As a result, we designed an associative carboxyl pathway with redox regeneration starting from $2CO_{Pt}$-OH_{int}-OH_s:

(R43) $2CO_{Pt}\text{-}OH_{int}\text{-}OH_s \rightarrow COOH_{(Pt\text{-}int\text{-}I)}\text{-}CO_{Pt}\text{-}OH_s$

(R44) $COOH_{(Pt\text{-}int\text{-}I)}\text{-}CO_{Pt}\text{-}OH_s \rightarrow CO_{2(Pt\text{-}int)}\text{-}CO_{Pt}\text{-}OHH_s$

(R45) $CO_{2(Pt\text{-}int)}\text{-}CO_{Pt}\text{-}OHH_s \rightarrow COOH_{(Pt\text{-}int\text{-}II)}\text{-}CO_{Pt}\text{-}OH_s$

(R46) $COOH_{(Pt\text{-}int\text{-}II)}\text{-}CO_{Pt}\text{-}OH_s + *_{Pt} \rightarrow CO_{2(Pt\text{-}int)}\text{-}CO_{Pt}\text{-}H_{Pt}\text{-}OH_s$

(R47) $CO_{2(Pt\text{-}int)}\text{-}CO_{Pt}\text{-}H_{Pt}\text{-}OH_s \rightarrow *_{Pt}\text{-}V_{int}\text{-}CO_{Pt}\text{-}H_{Pt}\text{-}OH_s + CO_{2(g)}$

(R48) $*_{Pt}\text{-}V_{int}\text{-}CO_{Pt}\text{-}H_{Pt}\text{-}OH_s + CO_{(g)} \rightarrow 2CO_{Pt}\text{-}V_{int}\text{-}H_{Pt}\text{-}OH_s$

(R49) $2CO_{Pt}\text{-}V_{int}\text{-}H_{Pt}\text{-}OH_s + H_2O_{(g)} \rightarrow 2CO_{Pt}\text{-}H_2O_{(int)}\text{-}H_{Pt}\text{-}OH_s$

(R50) $2CO_{Pt}\text{-}H_2O_{(int)}\text{-}H_{Pt}\text{-}OH_s + *_{Pt} \rightarrow 2CO_{Pt}\text{-}2H_{Pt}\text{-}OH_{int}\text{-}OH_s$

(R51) $2CO_{Pt}\text{-}2H_{Pt}\text{-}OH_{int}\text{-}OH_s \rightarrow 2CO_{Pt}\text{-}OH_{int}\text{-}OH_s + 2*_{Pt} + H_{2(g)}$

Figure (5-14) depicts the energy and free energy profiles for this cycle and the intermediate structures are shown in Figure (5-15). The first step in this cycle is carboxyl formation from the interfacial –OH group and the adsorbed CO at the interface (R43). It is worth noticing that by water dissociation, one of the bridging adsorbed CO molecules has moved to the linear position on Pt ($2CO_{Pt}\text{-}OH_{int}\text{-}OH_s$). The process for carboxyl formation is 0.50 eV endothermic and has a 0.74 eV activation barrier. Next, $COOH_{(Pt\text{-}int\text{-}I)}$ dissociates to the nearby surface –OH to create $–OHH_s$ (adsorbed water at the surface oxygen vacancy) and an adsorbed CO_2 species at the interface (R44). Subsequently, the H in $–OHH_s$ is transferred back to the free oxygen of the CO_2 to form a more stable $COOH_{(Pt\text{-}int\text{-}II)}$ (R45). We note here that this step also involves the –OH rotation (not shown here) that corresponds to the *cis-trans* isomerization of the adsorbed COOH intermediate. Reaction steps (R44) and (R45) basically represent the H-transfer between the two oxygen atoms within the –COOH species which leads to the formation of a more stable intermediate and permits at the same time the dissociation of COOH directly to the metal cluster. NEB calculations suggested that the direct transfer of the H atom between these two oxygen atoms has a barrier of more than 1 eV. However, the presence of a nearby surface –OH group facilitates this H-transfer with barriers of less than 0.2 eV.

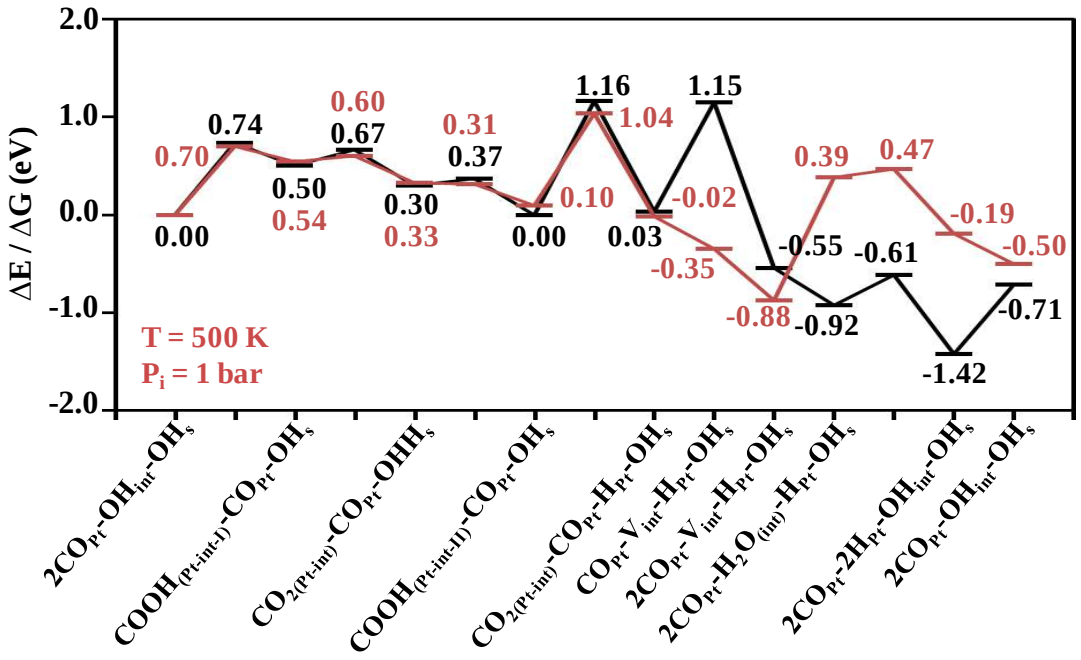

FIGURE 5-14. The (free) energy profile for the associative carboxyl pathway with redox regeneration – model II starting from dissociated water at the interface to O_s ($2CO_{Pt}$-OH_{int}-OH_s)

The *trans*-COOH intermediate then dissociates to Pt in a thermo neutral process (0.03 eV exothermic) and an activation barrier of 1.16 eV. The next steps are CO_2 desorption and CO adsorption that are 1.12 eV endothermic and 1.70 eV exothermic, respectively. Free energy wise, CO_2 desorption and CO adsorption are both exergonic by 0.33 and 0.53 eV, respectively. After CO adsorption, H_2O adsorbs at the interfacial oxygen vacancy in a 0.37 eV exothermic process (ΔG^{ads} = 1.27 eV). Next, water dissociates to create a $2CO_{Pt}$-$2H_{Pt}$-OH_{int}-OH_s site. This process is 0.50 eV exothermic and has a 0.31 eV activation barrier. The final step for this cycle is H_2 desorption that is 0.71 eV endothermic (ΔG^{des} = -0.31 eV).

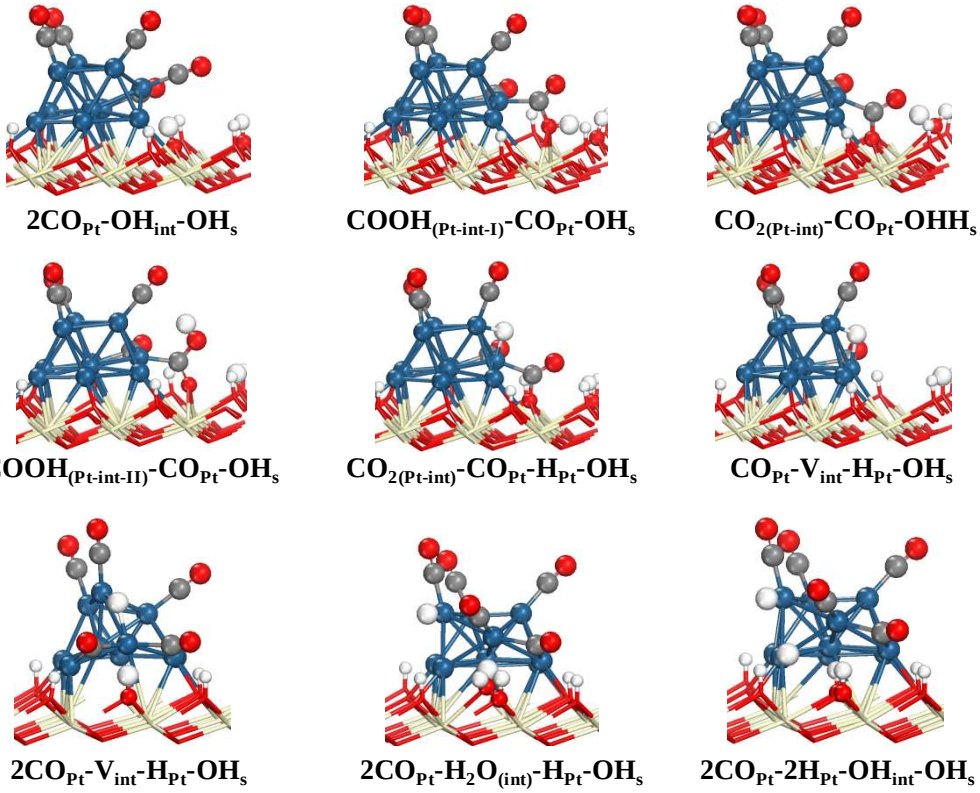

FIGURE 5-15. The intermediates structures for the associative carboxyl pathway with redox regeneration – model II starting from dissociated water at the interface to O_s ($2CO_{Pt}$-OH_{int}-OH_s)

The zero point corrected energies of the reaction steps and their activation barriers along with the forward and reverse rate constants at 473 K for this pathway have been provided in Table (5-8). The results of this microkinetic model at experimental reaction condition #1 have been provided in Table (5-9). At experimental condition #2 the results were quite similar. For this microkinetic model we combined the Redox pathways (I) and (II) and the associative carboxyl pathway with redox regeneration.

TABLE 5-8. The zero point corrected reaction energies and activation barriers along with kinetic parameters at 473 K for the elementary steps considered for the associative carboxyl pathway with redox regeneration – model II and also R42 for creation of the starting structure ($2CO_{Pt}$-OH_{int}-OH_s).

	ΔE^{zpc} (eV)	$E^{act,zpc}$ (eV)	k_f	k_r
R42	-1.04	0.14	5.17×10^{10}	1.88×10^{0}
R43	0.54	0.70	4.62×10^{5}	3.41×10^{11}
R44	-0.22	0.06	1.18×10^{12}	7.04×10^{9}
R45	-0.23	-0.02	8.22×10^{12}	5.86×10^{10}
R46	-0.12	0.94	1.80×10^{3}	7.37×10^{1}
R47	1.02	1.47	7.49×10^{2}	2.20×10^{4}
R48	-1.61		1.87×10^{9}	2.07×10^{0}
R49	-0.20		2.34×10^{9}	2.29×10^{15}
R50	-0.58	0.08	2.69×10^{12}	3.06×10^{6}
R51	0.56		4.10×10^{9}	7.02×10^{9}

TABLE 5-9. Reaction orders (n_i), apparent activation energies (E^{app}), and turn over frequencies (TOF) from microkinetic model for the combined pathways Redox (I) and (II), and the Associative carboxyl with redox regeneration, all derived from the modified catalyst model, with the individual pathways' contribution in the rate at experimental condition #1.

	Experimental condition #1 (P_{CO}=0.07, P_{CO2}=0.085, P_{H2O}=0.22, P_{H2}=0.37 atm; T = 473 K)	
	Model	**Experiment** [a]
$\mathbf{n_{CO}}$	0.00	-0.03
$\mathbf{n_{H2O}}$	0.74	0.44
$\mathbf{n_{CO2}}$	0.00	-0.09
$\mathbf{n_{H2}}$	-0.69	-0.38
TOF (s^{-1})	1.06×10^{1}	4.14×10^{-2}
Redox I	1.32×10^{-11}	
Redox II	3.14×10^{-7}	
Associative carboxyl pathway with redox regeneration	1.06×10^{1}	
$\mathbf{E^{app}}$ **(eV)**	0.98 [b]	0.78

[a] see reference (263)
[b] Apparent activation energy is calculated in the temperature ranges of 423-673 K.

The calculated TOF at 473 K is about 3 orders of magnitude higher than the experimental TOF. Considering that the experimental TOFs are normalized by the total

number of Pt atoms while our TOFs are based on interfacial Pt atoms, it is encouraging that our computed TOFs are larger than the experimental ones. The dominant path is the associative carboxyl pathway with redox regeneration. The pathway has the highest rate and predicts the lowest apparent activation barrier compared to our other redox models of 0.98 eV. The reaction orders are also displaying correct trends: zero reaction orders for CO and CO_2, positive reaction order for water and negative reaction order for hydrogen. Campbell's degree of rate control analysis at 473 K suggests that the COOH dissociation process (R46, $X_{RC} = 0.77$) together with the CO_2 desorption process (R47, $X_{RC} = 0.23$) are the most important steps that affect the overall rate of the reaction. The surface coverages of all intermediates obtained from our microkinetic modeling and Campbell's degree of thermodynamic rate control analysis suggest that the oxygen vacancy structure ($2CO_{Pt}$-V_{int}-H_{Pt}-OH_s) is the dominant species throughout the temperature range considered here and the stability of this intermediate has a significant effect on the overall rate of reaction. It has to be noted here that we also created oxygen vacancies at different steps of the redox pathways, but only this particular intermediate ($2CO_{Pt}$-V_{int}-H_{Pt}-OH_s) that is created during the associative pathway with redox regeneration becomes the dominant intermediate. The structure of this intermediate (Figure 5-15) suggests that it is possible to form multiple oxygen vacancies at the Pt/CeO_2 interface and that all the Pt sites neighboring the vacancy will be covered by CO and all the surface oxygen atoms adjacent to the vacancy will be covered by hydrogen under WGS reaction conditions. Only after including these stable structures in the pathway was our model able to predict the experimentally observed activation barriers, reaction orders, and rate determining steps.

5.3.4. Associative Carboxyl Pathways – Model II

In the previous section, we have shown that our new model with additional CO at the interfacial Pt could predict experimental observations for the associative carboxyl pathway with redox regeneration. In this section, we used the same model to investigate the associative carboxyl pathway at the Pt/CeO_2 interface that does not include the formation of oxygen vacancies. We note here that our Model I with only one linear CO adsorbed at the interface predicted a very high apparent activation energy and a low rate (section 5.2). The reaction steps that have been considered for the first cycle after reaction step (R30) (CO adsorption) are as follows:

(R52) $2CO_{Pt}\text{-}O_{int} + *_{Ce} + H_2O_{(g)} \rightarrow 2CO_{Pt}\text{-}H_2O_{(Ce)}\text{-}O_{int}$

(R53) $2CO_{Pt}\text{-}H_2O_{(Ce)}\text{-}O_{int} + *_{Pt} \rightarrow 2CO_{Pt}\text{-}OH_{(Ce\text{-}Pt)}\text{-}OH_{int}$

(R54) $2CO_{Pt}\text{-}OH_{(Ce\text{-}Pt)}\text{-}OH_{int} \rightarrow CO_{Pt}\text{-}COOH_{Pt}\text{-}OH_{int} + *_{Ce}$

(R55) $CO_{Pt}\text{-}COOH_{Pt}\text{-}OH_{int} + *_{Pt} \rightarrow CO_{Pt}\text{-}CO_{2(Pt)}\text{-}H_{Pt}\text{-}OH_{int}$

(R56) $CO_{Pt}\text{-}CO_{2(Pt)}\text{-}H_{Pt}\text{-}OH_{int} \rightarrow *_{Pt}\text{-}CO_{Pt}\text{-}H_{Pt}\text{-}OH_{int} + CO_{2(g)}$

Reaction steps (R35) and (R36) are also needed to close this cycle. Since the active site becomes empty after CO_2 desorption in reaction step (R56), we have also considered the possibility of another CO adsorption at the active site before H-transfer. The reaction steps considered are as follows:

(R57) $*_{Pt}\text{-}CO_{Pt}\text{-}H_{Pt}\text{-}OH_{int} + CO_{(g)} \rightarrow 2CO_{Pt}\text{-}H_{Pt}\text{-}OH_{int}$

(R58) $2CO_{Pt}\text{-}H_{Pt}\text{-}OH_{int} + *_{Pt} \rightarrow 2CO_{Pt}\text{-}2H_{Pt}\text{-}O_{int}$

(R59) $2CO_{Pt}\text{-}2H_{Pt}\text{-}O_{int} \rightarrow 2CO_{Pt}\text{-}O_{int} + 2*_{Pt} + H_{2(g)}$

Figure (5-16) depicts the energy and free energy profiles for these cycles and the new intermediate structures are shown in Figure (5-17).

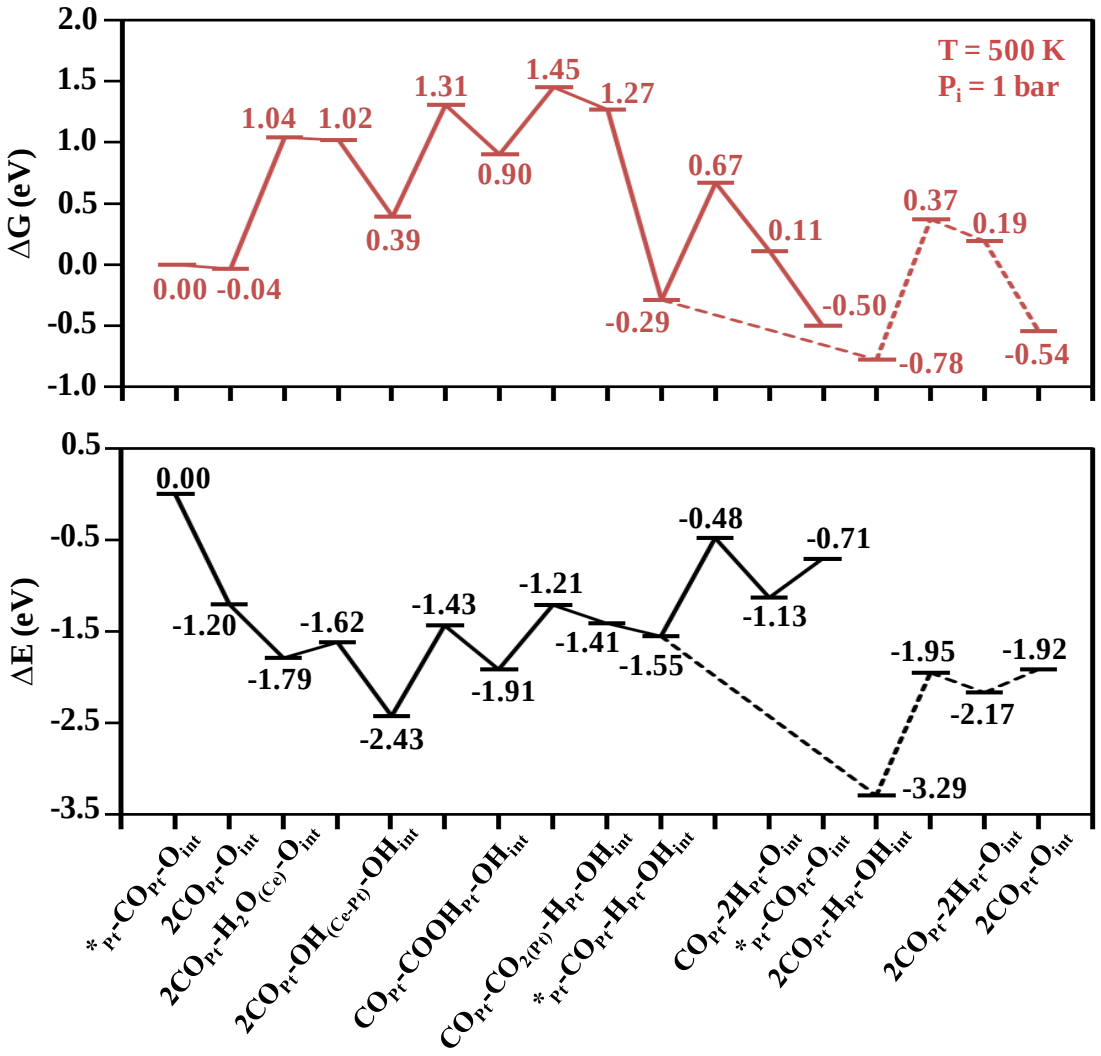

FIGURE 5-16. The energy and free energy profiles for the associative carboxyl pathways – model II, derived from the modified catalyst model (the dashed line shows the extra steps that are needed to close the CO-promoted associative carboxyl pathway – model II)

For the first cycle, after initial CO adsorption (R30), water adsorbs on the Ce metal of the ceria surface in a 0.59 eV exothermic process (R52: ΔG^{ads} = 1.08 eV). Next, it dissociates to the interfacial oxygen. Due to the orientation of adsorbed water, the OH

group of the dissociated water can make bonds with both Ce and Pt ($2CO_{Pt}$-$OH_{(Ce-Pt)}$-OH_{int}). The dissociation process is 0.64 eV exothermic with an activation barrier of 0.17 eV. The next step is carboxyl formation that is 0.52 eV endothermic and has an activation barrier of 1.00 eV. After *cis*- and *trans*- transformation of the carboxyl species, it dissociates to the Pt cluster in a 0.50 eV endothermic process with a 0.70 eV activation barrier. Next, CO_2 desorbs which is 0.14 eV exothermic (ΔG^{des} = -1.56 eV). After CO_2 desorption the interfacial –OH dissociates to the Pt cluster and finally H_2 desorbs. These reactions are (R35) and (R36) and have previously already been explained.

In a second cycle (CO-promoted path) after CO_2 desorption, CO adsorbs which is 1.74 eV exothermic (ΔG^{ads} = -0.49 eV). Next, the interfacial –OH group dissociates which is 1.12 eV endothermic and has a 1.34 eV activation barrier. The final step to close this catalytic cycle and to get back to its initial structure ($2CO_{Pt}$-O_{int}), H_2 desorbs which is 0.25 eV endothermic (ΔG^{des} = -0.73 eV).

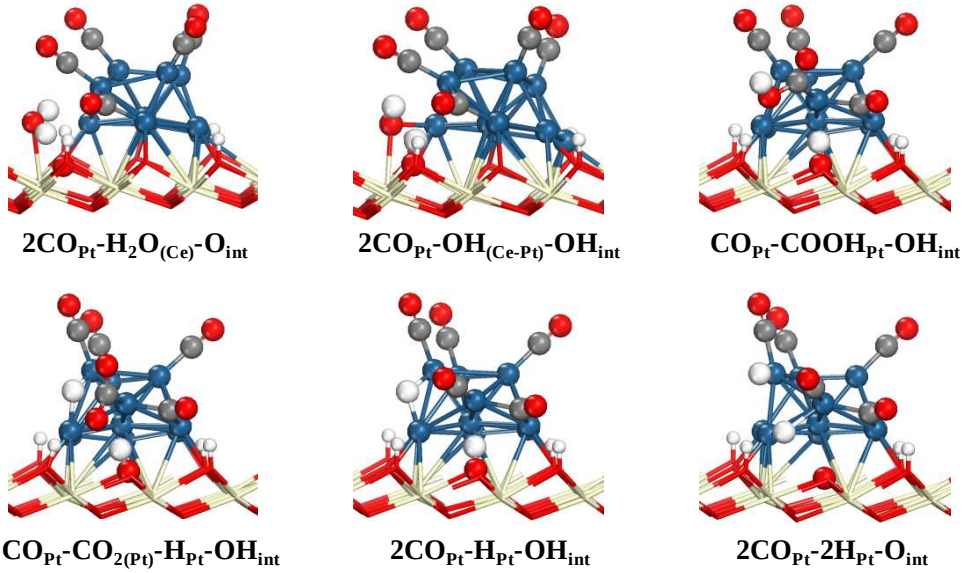

FIGURE 5-17. The new intermediate structures for the associative carboxyl pathways – model II

The energetic and kinetic parameters for the explained reaction steps are provided in Table (5-10). The microkinetic modeling's results at experimental reaction condition #1 are provided in Table (5-11).

TABLE 5-10. The zero point corrected reaction energies and activation barriers along with kinetic parameters at 473 K for the new elementary steps considered for the associative carboxyl pathways – model II, derived from the modified catalyst model

	ΔE^{zpc} (eV)	$E^{act,zpc}$ (eV)	k_f	k_r
R52	-0.41		2.34×10^{9}	1.93×10^{13}
R53	-0.65	-0.02	4.89×10^{13}	5.99×10^{6}
R54	0.43	0.92	2.65×10^{3}	7.80×10^{7}
R55	0.44	0.63	1.22×10^{6}	2.97×10^{10}
R56	-0.17		2.87×10^{19}	1.50×10^{9}
R57	-1.61		1.87×10^{9}	2.73×10^{0}
R58	0.98	1.15	7.44×10^{0}	2.80×10^{10}
R59	0.15		1.83×10^{13}	7.02×10^{9}

TABLE 5-11. Reaction orders (n_i), apparent activation energies (E^{app}), and turn over frequencies (TOF) from microkinetic model for the associative carboxyl pathways – model II at experimental condition #1

	Experimental condition #1 (P_{CO}=0.07, P_{CO2}=0.085, P_{H2O}=0.22, P_{H2}=0.37 atm; T = 473 K)	
	Model	**Experiment** [a]
$\mathbf{n_{CO}}$	0.00	-0.03
$\mathbf{n_{H2O}}$	1.00	0.44
$\mathbf{n_{CO2}}$	0.00	-0.09
$\mathbf{n_{H2}}$	-1.00	-0.38
TOF (s^{-1})	1.66×10^{-2}	4.14×10^{-2}
$\mathbf{E^{app}}$ **(eV)**[b]	1.18	0.78

[a] see reference (263)
[b] Apparent activation energy is calculated in the temperature ranges of 423-673 K.

Although the calculated TOF is in close agreement to the experimental value, it is about 3 orders of magnitude smaller than the TOF calculated for the "associative carboxyl pathway with redox regeneration" (10.6 s^{-1}). Also, we note that the modeling

TOFs are computed based on interface sites while experimental TOFs are normalized by the total number of Pt surface sites. In the associative pathway the reaction proceeds as expected through the lowest energy pathway which involves a second CO adsorption after CO_2 desorption (R57). The apparent activation barrier is still high compared to experiment observations as well as the "associative carboxyl pathway with redox regeneration". However, compared to the previous model for the associative carboxyl pathway (CO-promoted associative carboxyl pathway: E^{app} = 1.49 eV) the barrier of the new model has improved by 0.31 eV. Next, the reaction rate orders of the new model can predict the correct trends of the experimental observations: positive order for H_2O, negative order for H_2, and zero orders for CO and CO_2.

By calculating the degree of rate control, carboxyl dissociation is found to be the most important reaction step (R55) with a degree of rate control of 0.93 followed by carboxyl formation (R54) with 0.07 degree of rate control. The degree of thermodynamic rate control of -1.00 is found for $2CO_{Pt}$-H_{Pt}-OH_{int} which shows that this species is the most important reaction intermediate.

5.4. Conclusion

We investigated the activity of small Pt clusters supported on a CeO_2 (111) surface for the low temperature WGS reaction. The challenges we faced in choosing an appropriate catalyst model for this study are evident from the results presented in sections 5.1-5.2. Although our initial thermodynamic analysis suggested an appropriate model for the mechanistic study, further microkinetic modeling using Model I suggested the possibility of the presence of more CO molecules at the interfacial Pt atoms. Meaningful results could be obtained only after including additional CO at the interface (Model II). It is

generally believed that the strong adsorption of CO could poison the metal surface (blocking of active sites) which consequently reduces the rate of reaction. However, our results suggest that these strongly adsorbed CO molecules could assist the WGS reaction at neighboring sites by reducing the CO adsorption strength. Combined microkinetic modeling of the "Redox" and "Associative carboxyl with redox regeneration" pathways suggest that the latter is the most dominant pathway. This pathway predicted the highest rate and lowest activation barrier compared to the redox pathway. Since CO adsorbs strongly on the interfacial Pt atom, especially in the presence of an oxygen vacancy, the traditional redox pathway does not operate at the Pt/CeO_2 interface. H_2O prefers to dissociate at the vacancy by transferring an H atom to neighboring surface oxygen rather than transferring the H atom to Pt. Only when all the neighboring surface oxygens are already covered by hydrogen can H_2O dissociation occur at the metal-oxide interface. Because of the strong adsorption of H on the surface oxygen atoms, a direct H transfer from interface –OH to Pt becomes energetically unfavorable, especially in the presence of CO on Pt (Redox II). Thus, the reaction proceeds through the formation of a carboxyl (COOH) intermediate. The dissociation of this intermediate is facilitated by the presence of neighboring surface –OH groups.

The "Associative carboxyl" pathway (section 5.3.5) which does not involve the formation of oxygen vacancies also predicted non-negligible rates compared to the "Associative carboxyl pathway with redox regeneration". The higher rates obtained for the latter pathway manifests the importance of the oxygen vacancy for the low-temperature WGS reaction. Our results also suggested the vacancy structure to be the dominant intermediate in this process which facilitates H_2O activation and dissociation.

The lower rates obtained for the WGS reaction on the Pt (111) surface and Pt on irreducible oxide supports can be explained by the difficulty in dissociating H_2O on these surfaces. Our calculations show that compared to the Pt (111) surface, the improved WGS activity of the TPB can be explained by an increased number of oxygen vacancies at the TPB, and a significantly facilitated water activation and dissociation.

References

1. Azadi, P.; Otomo, J.; Hatano, H.; Oshima, Y.; Farnood, R., Hydrogen production by catalytic near-critical water gasification and steam reforming of glucose. *International Journal of Hydrogen Energy* **2010,** *35* (8), 3406-3414.

2. Ishida, Y.; Kumabe, K.; Hata, K.; Tanifuji, K.; Hasegawa, T.; Kitagawa, K.; Isu, N.; Funahashi, Y.; Asai, T., Selective hydrogen generation from real biomass through hydrothermal reaction at relatively low temperatures. *Biomass & Bioenergy* **2009,** *33* (1), 8-13.

3. Wang, W. B.; Cao, X. B.; Gao, W. J.; Zhang, F.; Wang, H. T.; Ma, G. L., Ammonia synthesis at atmospheric pressure using a reactor with thin solid electrolyte BaCe0.85Y0.15O3-alpha membrane. *Journal of Membrane Science* **2010,** *360* (1-2), 397-403.

4. Cwalina, J.; Gregor, M.; Pohorecki, R., Production of ammonia synthesis gas. Technological evolution of CO2 removal from process gas with potassium carbonate solution. *Przemysl Chemiczny* **2009,** *88* (12), 1268-1272.

5. Dukowicz, J. W.; Stryjek, R.; Mozenska, B.; Gregor, M., Process thermodynamics models in simulation program sets of the technology for ammonia synthesis. *Przemysl Chemiczny* **2009,** *88* (12), 1274-1278.

6. Truszkiewicz, E.; Rarog-Pilecka, W.; Schmidt-Szatowski, K.; Jodzis, S.; Wilczkowska, E.; Lomot, D.; Kaszkur, Z.; Karpinski, Z.; Kowalczyk, Z., Barium-promoted Ru/carbon catalyst for ammonia synthesis: State of the system when operating. *Journal of Catalysis* **2009,** *265* (2), 181-190.

7. Bermudez, J. M.; Fidalgo, B.; Arenillas, A.; Menendez, J. A., Dry reforming of coke oven gases over activated carbon to produce syngas for methanol synthesis. *Fuel* **2010,** *89* (10), 2897-2902.

8. Chiavassa, D. L.; Collins, S. E.; Bonivardi, A. L.; Baltanas, M. A., Methanol synthesis from CO2/H-2 using Ga2O3-Pd/silica catalysts: Kinetic modeling. *Chemical Engineering Journal* **2009,** *150* (1), 204-212.

9. Lin, Y. C.; Fan, L. T.; Shafie, S.; Bertok, B.; Friedler, F., Generation of light hydrocarbons through Fischer-Tropsch synthesis: Identification of potentially dominant catalytic pathways via the graph-theoretic method and energetic analysis. *Comput. Chem. Eng.* **2009,** *33* (6), 1182-1186.

10. Kim, C. U.; Kim, Y. S.; Chae, H. J.; Jeong, K. E.; Jeong, S. Y.; Jun, K. W.; Lee, K. Y., Effect of cobalt catalyst type and reaction medium on Fischer-Tropsch synthesis. *Korean Journal of Chemical Engineering* **2010,** *27* (3), 777-784.

11. Ratnasamy, C.; Wagner, J. P., Water Gas Shift Catalysis. *Catalysis Reviews-Science and Engineering* **2009,** *51* (3), 325-440.

12. Zalc, J. M.; Sokolovskii, V.; Loffler, D. G., Are noble metal-based water-gas shift catalysts practical for automotive fuel processing? *Journal of Catalysis* **2002,** *206* (1), 169-171.

13. Fu, Q.; Saltsburg, H.; Flytzani-Stephanopoulos, M., Active nonmetallic Au and Pt species on ceria-based water-gas shift catalysts. *Science* **2003,** *301* (5635), 935-938.

14. Iida, H.; Yamamoto, T.; Inagaki, M.; Igarashi, A., Derivation of Initial Rate Equations for Low-temperature Water Gas Shift Reaction over Pt-Re/ZrO2 Catalysts. *Chem. Lett.* **2010,** *39* (2), 144-145.

15. Gayen, A.; Boaro, M.; de Leitenburg, C.; Llorca, J.; Trovarelli, A., Activity, durability and microstructural characterization of ex-nitrate and ex-chloride Pt/Ce0.56Zr0.44O2 catalysts for low temperature water gas shift reaction. *Journal of Catalysis* **2010,** *270* (2), 285-298.

16. Deshpande, P. A.; Madras, G., Support-Dependent Activity of Noble Metal Substituted Oxide Catalysts for the Water Gas Shift Reaction. *Aiche J.* **2010,** *56* (10), 2662-2676.

17. Gonzalez, I. D.; Navarro, R. M.; Wen, W.; Marinkovic, N.; Rodriguez, J. A.; Rosa, F.; Fierro, J. L. G., A comparative study of the water gas shift reaction over platinum catalysts supported on CeO2, TiO2 and Ce-modified TiO2. *Catalysis Today* **2010,** *149* (3-4), 372-379.

18. Shelef, M.; McCabe, R. W., Twenty-five years after introduction of automotive catalysts: what next? *Catalysis Today* **2000,** *62* (1), 35-50.

19. Ribeiro, M. C.; Jacobs, G.; Graham, U. M.; Azzam, K. G.; Linganiso, L.; Davis, B. H., Low temperature water-gas shift: Differences in oxidation states observed with partially reduced Pt/MnOX and Pt/CeOX catalysts yield differences in OH group reactivity. *Catal. Commun.* **2010,** *11* (15), 1193-1199.

20. Jacobs, G.; Davis, B. H., Surface interfaces in low temperature water-gas shift: The metal oxide synergy, the assistance of co-adsorbed water, and alkali doping. *International Journal of Hydrogen Energy* **2010,** *35* (8), 3522-3536.

21. Senanayake, S. D.; Stacchiola, D.; Evans, J.; Estrella, M.; Barrio, L.; Perez, M.; Hrbek, J.; Rodriguez, J. A., Probing the reaction intermediates for the water-gas shift over inverse CeOx/Au(111) catalysts. *Journal of Catalysis* **2010,** *271* (2), 392-400.

22. Boaro, M.; Vicario, M.; Llorca, J.; de Leitenburg, C.; Dolcetti, G.; Trovarelli, A., A comparative study of water gas shift reaction over gold and platinum supported on ZrO2 and CeO2-ZrO2. *Applied Catalysis B-Environmental* **2009,** *88* (3-4), 272-282.

23. Park, J. B.; Graciani, J.; Evans, J.; Stacchiola, D.; Senanayake, S. D.; Barrio, L.; Liu, P.; Sanz, J. F.; Hrbek, J.; Rodriguez, J. A., Gold, Copper, and Platinum Nanoparticles Dispersed on CeOx/TiO2(110) Surfaces: High Water-Gas Shift Activity and the Nature of the Mixed-Metal Oxide at the Nanometer Level. *Journal of the American Chemical Society* **2010,** *132* (1), 356-363.

24. Mond, L.; Langer, C., Improvements in Obtaining Hydrogen *British Patent 12608* **1888**.

25. Bosch, C.; Wild, W., *Canadian Patent 153379* **1914**.

26. Chiavassa, D. L.; Barrandeguy, J.; Bonivardi, A. L.; Baltanas, M. A., Methanol synthesis from CO2/H-2 using Ga2O3-Pd/silica catalysts: Impact of reaction products. *Catalysis Today* **2008,** *133*, 780-786.

27. Setinc, M.; Levec, J., On the kinetics of liquid-phase methanol synthesis over commercial Cu/ZnO/Al2O3 catalyst. *Chemical Engineering Science* **1999,** *54* (15-16), 3577-3586.

28. Florin, N. H.; Harris, A. T., Preparation and characterization of a tailored carbon dioxide sorbent for enhanced hydrogen synthesis in biomass gasifiers. *Industrial & Engineering Chemistry Research* **2008,** *47* (7), 2191-2202.

29. Galvita, V.; Schroder, T.; Munder, B.; Sundmacher, K., Production of hydrogen with low COx-content for PEM fuel cells by cyclic water gas shift reactor. *International Journal of Hydrogen Energy* **2008,** *33* (4), 1354-1360.

30. Lattin, W. C.; Utgikar, V. P., Transition to hydrogen economy in the United States: A 2006 status report. *International Journal of Hydrogen Energy* **2007,** *32* (15), 3230-3237.

31. Kapdan, I. K.; Kargi, F., Bio-hydrogen production from waste materials. *Enzyme and Microbial Technology* **2006,** *38* (5), 569-582.

32. Lattner, J. R.; Harold, M. P., Comparison of conventional and membrane reactor fuel processors for hydrocarbon-based PEM fuel cell systems. *International Journal of Hydrogen Energy* **2004,** *29* (4), 393-417.

33. Velu, S.; Suzuki, K.; Kapoor, M. P.; Ohashi, F.; Osaki, T., Selective production of hydrogen for fuel cells via oxidative steam reforming of methanol over CuZnAl(Zr)-oxide catalysts. *Applied Catalysis a-General* **2001,** *213* (1), 47-63.

34. Geissler, K.; Newson, E.; Vogel, F.; Truong, T. B.; Hottinger, P.; Wokaun, A., Autothermal methanol reforming for hydrogen production in fuel cell applications. *Physical Chemistry Chemical Physics* **2001,** *3* (3), 289-293.

35. Choi, Y.; Stenger, H. G., Fuel cell grade hydrogen from methanol on a commercial Cu/ZnO/Al2O3 catalyst. *Applied Catalysis B-Environmental* **2002,** *38* (4), 259-269.

36. Ritter, J. A.; Ebner, A. D., State-of-the-art adsorption and membrane separation processes for hydrogen production in the chemical and petrochemical industries. *Sep. Sci. Technol.* **2007,** *42* (6), 1123-1193.

37. Hinchiranan, S.; Zhang, Y.; Nagamori, S.; Vitidsant, T.; Tsubaki, N., TiO2 promoted Co/SiO2 catalysts for Fischer-Tropsch synthesis. *Fuel Processing Technology* **2008,** *89* (4), 455-459.

38. Demirbas, A., Converting Biomass derived synthetic gas to fuels via fisher-tropsch synthesis. *Energy Sources Part A-Recovery Util. Environ. Eff.* **2007,** *29* (16), 1507-1512.

39. Wilhelm, D. J.; Simbeck, D. R.; Karp, A. D.; Dickenson, R. L., Syngas production for gas-to-liquids applications: technologies, issues and outlook. *Fuel Processing Technology* **2001,** *71* (1-3), 139-148.

40. Van der Laan, G. P.; Beenackers, A., Kinetics and selectivity of the Fischer-Tropsch synthesis: A literature review. *Catalysis Reviews-Science and Engineering* **1999,** *41* (3-4), 255-318.

41. Murakami, T.; Nishimura, T.; Kasai, E., Lowering Reduction Temperature of Iron Ore and Carbon Composite by Using Ores with High Combined Water Content. *Isij International* **2009,** *49* (11), 1686-1693.

42. Tateo, U.; Tsunehisa, N.; Hideki, O.; Hirokazu, K.; Hirotoshi, K., Effective Use of Hydrogen in Gaseous Reduction of Iron Ore Agglomerates With H-2-CO. *Journal of Iron and Steel Research International* **2009,** *16*, 1179-1184.

43. Mendes, D.; Mendes, A.; Madeira, L. M.; Iulianelli, A.; Sousa, J. M.; Basile, A., The water-gas shift reaction: from conventional catalytic systems to Pd-based membrane reactors - a review. *Asia-Pacific Journal of Chemical Engineering* **2010,** *5* (1), 111-137.

44. Quirk, R. P., *Kirk-Othmer Encyclopedia of Chemical Engineering Technology* **1963,** *Vol. 2*.

45. Ladebeck, J. R.; Wang, J. P., *Handbook of Fuel Cells, Fuel Cell Technology and Applications* **2003,** *3*, 190-201.
46. Ruettinger, W. F.; Ilinich, O., *Encyclopedia of Chemical Processing* **2006**, 3205-3215.

47. O'Brien, R. J.; Davis, B. H., Impact of copper on an alkali promoted iron Fischer-Tropsch catalyst. *Catalysis Letters* **2004,** *94* (1-2), 1-6.

48. Lei, Y.; Cant, N. W.; Trimm, D. L., The origin of rhodium promotion of Fe3O4-Cr2O3 catalysts for the high-temperature water-gas shift reaction. *Journal of Catalysis* **2006,** *239* (1), 227-236.

49. Popa, T.; Xu, G. Q.; Barton, T. F.; Argyle, M. D., High temperature water gas shift catalysts with alumina. *Applied Catalysis a-General* **2010,** *379* (1-2), 15-23.

50. Chang, F. W.; Ou, T. C.; Roselin, L. S.; Chen, W. S.; Lai, S. C.; Wu, H. M., Production of hydrogen by partial oxidation of methanol over bimetallic Au-Cu/TiO2-Fe2O3 catalysts. *J. Mol. Catal. A-Chem.* **2009,** *313* (1-2), 55-64.

51. Hua, J. M.; Zheng, Q.; Zheng, Y. H.; Wei, K. M.; Lin, X. Y., Influence of modifying additives on the catalytic activity and stability of Au/Fe2O3-MOx catalysts for the WGS reaction. *Catalysis Letters* **2005,** *102* (1-2), 99-108.

52. Newsome, D. S., The Water-Gas Shift Reaction. *Catalysis Reviews-Science and Engineering* **1980,** *21* (2), 275-318.

53. Lloyd, L.; Ridler, D. E.; Twigg, M. V., The water gas shift reaction. *Catalyst Handbook* **1996**, 283-338.

54. Thurgood, C. P.; Amphlett, J. C.; Mann, R. F.; Peppley, B. A., Deactivation of Cu/ZnO/Al2O3 catalyst: evolution of site concentrations with time. *Topics in Catalysis* **2003,** *22* (3-4), 253-259.

55. Twigg, M. V.; Spencer, M. S., Deactivation of supported copper metal catalysts for hydrogenation reactions. *Applied Catalysis a-General* **2001,** *212* (1-2), 161-174.

56. Guo, P. J.; Chen, L. F.; Yu, G. B.; Zhu, Y.; Qiao, M. H.; Xu, H. L.; Fan, K. N., Cu/ZnO-based water-gas shift catalysts in shut-down/start-up operation. *Catal. Commun.* **2009,** *10* (8), 1252-1256.

57. Tohji, K.; Udagawa, Y.; Hizushima, T.; Vino, A., The structure of the Cu-ZnO catalysts by an in-situ EXAFS study. *Physical Chemistry* **1985,** *89* (26), 5671-5676.

58. Hansen, P. L.; Wagner, J. B.; Helveg, S.; Rostrup-Nielsen, J. R.; Clausen, B. S.; Topsoe, H., Atom-resolved imaging of dynamic shape changes in supported copper nanocrystals. *Science* **2002,** *295* (5562), 2053-2055.

59. Spencer, M. S., The role of zinc oxide in Cu ZnO catalysts for methanol synthesis and the water-gas shift reaction. *Topics in Catalysis* **1999,** *8* (3-4), 259-266.

60. Rodriguez, J. A.; Hrbek, J., Interaction of sulfur with well-defined metal and oxide surfaces: Unraveling the mysteries behind catalyst poisoning and desulfurization. *Accounts of Chemical Research* **1999,** *32* (9), 719-728.

61. Zhang, L. Z.; Millet, J. M. M.; Ozkan, U. S., Deactivation characteristics of Fe-Al-Cu water-gas shift catalysts in the presence of H2S. *J. Mol. Catal. A-Chem.* **2009,** *309* (1-2), 63-70.

62. Stanislaus, A.; Marafi, A.; Rana, M. S., Recent advances in the science and technology of ultra low sulfur diesel (ULSD) production. *Catalysis Today* **2010,** *153* (1-2), 1-68.

63. Eijsbouts, S.; van den Oetelaar, L. C. A.; Louwen, J. N.; van Puijenbroek, R. R.; van Leerdam, K. G. C., Changes of MoS2 morphology and the degree of Co segregation during the sulfidation and deactivation of commercial Co-Mo/Al2O3 hydroprocessing catalysts. *Industrial & Engineering Chemistry Research* **2007,** *46* (12), 3945-3954.

64. Eijsbouts, S., On the flexibility of the active phase in hydrotreating catalysts. *Applied Catalysis a-General* **1997,** *158* (1-2), 53-92.

65. Pashigreva, A. V.; Klimov, O. V.; Bukhtiyarova, G. A.; Kochubey, D. I.; Prosvirin, I. P.; Chesalov, Y. A.; Zaikovskii, V. I.; Noskov, A. S., High-active hydrotreating catalysts for heavy petroleum feeds: Intentional synthesis of CoMo sulfide particles with optimal localization on the support surface. *Catalysis Today* **2010,** *150* (3-4), 164-170.

66. Wang, H. F.; Lian, Y. X.; Li, Y. N.; Fang, W. P.; Yang, Y. Q., W-promoted Co-Mo-K/gamma-Al2O3 catalysts for water-gas shift reaction. *Catal. Commun.* **2009,** *10* (14), 1864-1867.

67. Aldridge, C. L.; Kalina, T., *U.K. Patent 1325172* **1969**.

68. Aldridge, C. L., *U.S. Patent 3615216* **1968**.

69. Koh, J. H.; Lee, J. J.; Kim, H.; Cho, A.; Moon, S. H., Correlation of the deactivation of CoMo/Al2O3 in hydrodesulfurization with surface carbon species. *Applied Catalysis B-Environmental* **2009,** *86* (3-4), 176-181.

70. Abdollahi, M.; Yu, J. A.; Hwang, H. T.; Liu, P. K. T.; Ciora, R.; Sahimi, M.; Tsotsis, T. T., Process Intensification in Hydrogen Production from Biomass-Derived Syngas. *Industrial & Engineering Chemistry Research* **2010,** *49* (21), 10986-10993.

71. Eijsbouts, S.; Battiston, A. A.; van Leerdam, G. C., Life cycle of hydroprocessing catalysts and total catalyst management. *Catalysis Today* **2008,** *130* (2-4), 361-373.

72. Grenoble, D. C.; Estadt, M. M.; Ollis, D. F., The Chemistry and Catalysis of the Water Gas Shift Reaction .1. The Kinetics over Supported Metal-Catalysts. *Journal of Catalysis* **1981,** *67* (1), 90-102.

73. Ozawa, M., Thermal stabilization of catalytic compositions for automobile exhaust treatment through rare earth modification of alumina nanoparticle support. *Journal of Alloys and Compounds* **2006,** *408*, 1090-1095.

74. Skoglundh, M.; Johansson, H.; Lowendahl, L.; Jansson, K.; Dahl, L.; Hirschauer, B., Cobalt-promoted palladium as a three-way catalyst. *Applied Catalysis B-Environmental* **1996,** *7* (3-4), 299-319.

75. Gonzalezvelasco, J. R.; Entrena, J.; Gonzalezmarcos, J. A.; Gutierrezortiz, J. I.; Gutierrezortiz, M. A., PREPARATION, ACTIVITY AND DURABILITY OF PROMOTED PLATINUM CATALYSTS FOR AUTOMOTIVE EXHAUST CONTROL. *Applied Catalysis B-Environmental* **1994,** *3* (2-3), 191-204.

76. Martin, L.; Arranz, J. L.; Prieto, O.; Trujillano, R.; Holgado, M. J.; Galan, M. A.; Rives, V., Simulation three-way catalyst ageing - Analysis of two conventional catalyst. *Applied Catalysis B-Environmental* **2003,** *44* (1), 41-52.

77. Solov'ev, S. A.; Orlik, S. N., Structural and Functional Design of Catalytic Converters for Emissions from Internal Combustion Engines. *Kinetics and Catalysis* **2009,** *50* (5), 705-714.

78. Kim, C. H.; Thompson, L. T., Deactivation of Au/CeOx water gas shift catalysts. *Journal of Catalysis* **2005,** *230* (1), 66-74.

79. Andreeva, D.; Idakiev, V.; Tabakova, T.; Ilieva, L.; Falaras, P.; Bourlinos, A.; Travlos, A., Low-temperature water-gas shift reaction over Au/CeO2 catalysts. *Catalysis Today* **2002,** *72* (1-2), 51-57.

80. Bunluesin, T.; Gorte, R. J.; Graham, G. W., Studies of the water-gas-shift reaction on ceria-supported Pt, Pd, and Rh: implications for oxygen-storage properties. *Applied Catalysis B-Environmental* **1998,** *15* (1-2), 107-114.

81. Thinon, O.; Diehl, F.; Avenier, P.; Schuurman, Y., Screening of bifunctional water-gas shift catalysts. *Catalysis Today* **2008,** *137* (1), 29-35.

82. Luengnaruemitchai, A.; Osuwan, S.; Gulari, E., Comparative studies of low-temperature water-gas shift reaction over Pt/CeO2, Au/CeO2, and Au/Fe2O3 catalysts. *Catal. Commun.* **2003,** *4* (5), 215-221.

83. Boccuzzi, F.; Chiorino, A.; Manzoli, M.; Andreeva, D.; Tabakova, T.; Ilieva, L.; Iadakiev, V., Gold, silver and copper catalysts supported on TiO2 for pure hydrogen production. *Catalysis Today* **2002,** *75* (1-4), 169-175.

84. Panagiotopoulou, P.; Papavasiliou, J.; Avgouropoulos, G.; Ioannides, T.; Kondarides, D. I., Water-gas shift activity of doped Pt/CeO2 catalysts. *Chemical Engineering Journal* **2007,** *134* (1-3), 16-22.

85. Goguet, A.; Meunier, F.; Breen, J. P.; Burch, R.; Petch, M. I.; Ghenciu, A. F., Study of the origin of the deactivation of a Pt/CeO2 catalyst during reverse water gas shift (RWGS) reaction. *Journal of Catalysis* **2004,** *226* (2), 382-392.

86. Germani, G.; Schuurman, Y., Water-gas shift reaction kinetics over mu-structured Pt/CeO2/Al2O3 catalysts. *Aiche Journal* **2006,** *52* (5), 1806-1813.

87. Panagiotopoulou, P.; Kondarides, D. I., Effect of morphological characteristics of TiO2-supported noble metal catalysts on their activity for the water-gas shift reaction. *Journal of Catalysis* **2004,** *225* (2), 327-336.

88. Xue, E.; OKeeffe, M.; Ross, J. R. H., Water-gas shift conversion using a feed with a low steam to carbon monoxide ratio and containing sulphur. *Catalysis Today* **1996,** *30* (1-3), 107-118.

89. Hilaire, S.; Wang, X.; Luo, T.; Gorte, R. J.; Wagner, J., A comparative study of water-gas-shift reaction over ceria supported metallic catalysts. *Applied Catalysis a-General* **2001,** *215* (1-2), 271-278.

90. Liu, X. S.; Ruettinger, W.; Xu, X. M.; Farrauto, R., Deactivation of Pt/CeO2 water-gas shift catalysts due to shutdown/startup modes for fuel cell applications. *Applied Catalysis B-Environmental* **2005,** *56* (1-2), 69-75.

91. Jacobs, G.; Williams, L.; Graham, U.; Sparks, D.; Davis, B. H., Low-temperature water-gas shift: In-situ DRIFTS - Reaction study of a Pt/CeO2 catalyst for fuel cell reformer applications. *Journal of Physical Chemistry B* **2003,** *107* (38), 10398-10404.

92. Gorte, R. J.; Zhao, S., Studies of the water-gas-shift reaction with ceria-supported precious metals. *Catalysis Today* **2005,** *104* (1), 18-24.

93. Ishida, T.; Kinoshita, N.; Okatsu, H.; Akita, T.; Takei, T.; Haruta, M., Influence of the Support and the Size of Gold Clusters on Catalytic Activity for Glucose Oxidation. *Angewandte Chemie-International Edition* **2008,** *47* (48), 9265-9268.

94. Panagiotopoulou, P.; Kondarides, D. I., Effect of the nature of the support on the catalytic performance of noble metal catalysts for the water-gas shift reaction. *Catalysis Today* **2006,** *112* (1-4), 49-52.

95. Liu, P.; Rodriguez, J. A., Water-gas-shift reaction on metal nanoparticles and surfaces. *Journal of Chemical Physics* **2007,** *126* (16), 164705.

96. Azzam, K. G.; Babich, I. V.; Seshan, K.; Lefferts, L., A bifunctional catalyst for the single-stage water-gas shift reaction in fuel cell applications. Part 2. Roles of the support and promoter on catalyst activity and stability. *Journal of Catalysis* **2007,** *251* (1), 163-171.

97. Haruta, M., Gold as a novel catalyst in the 21st century: Preparation, working mechanism and applications. *Gold Bulletin* **2004,** *37* (1-2), 27-36.

98. Zhou, Z.; Kooi, S.; Flytzani-Stephanopoulos, M.; Saltsburg, H., The Role of the Interface in CO Oxidation on Au/CeO2 Multilayer Nanotowers. *Advanced Functional Materials* **2008,** *18* (18), 2801-2807.

99. Rodriguez, J. A.; Ma, S.; Liu, P.; Hrbek, J.; Evans, J.; Perez, M., Activity of CeOx and TiOx nanoparticles grown on Au(111) in the water-gas shift reaction. *Science* **2007,** *318* (5857), 1757-1760.

100. El-Moemen, A. A.; Kucerova, G.; Behm, R. J., Influence of H-2, CO2 and H2O on the activity and deactivation behavior of Au/CeO2 catalysts in the water gas shift reaction at 300 degrees C. *Applied Catalysis B-Environmental* **2010,** *95* (1-2), 57-70.

101. Quiney, A. S.; Schuurman, Y., Kinetic modelling of CO conversion over a Cu/ceria catalyst. *Chemical Engineering Science* **2007,** *62* (18-20), 5026-5032.

102. Fu, Q.; Deng, W. L.; Saltsburg, H.; Flytzani-Stephanopoulos, M., Activity and stability of low-content gold-cerium oxide catalysts for the water-gas shift reaction. *Applied Catalysis B-Environmental* **2005,** *56* (1-2), 57-68.

103. Koryabkina, N. A.; Phatak, A. A.; Ruettinger, W. F.; Farrauto, R. J.; Ribeiro, F. H., Determination of kinetic parameters for the water-gas shift reaction on copper catalysts under realistic conditions for fuel cell applications. *Journal of Catalysis* **2003,** *217* (1), 233-239.

104. Tibiletti, D.; Amieiro-Fonseca, A.; Burch, R.; Chen, Y.; Fisher, J. M.; Goguet, A.; Hardacre, C.; Hu, P.; Thompsett, A., DFT and in situ EXAFS investigation of gold/ceria-zirconia low-temperature water gas shift catalysts: Identification of the nature of the active form of gold. *Journal of Physical Chemistry B* **2005,** *109* (47), 22553-22559.

105. Burch, R., Gold catalysts for pure hydrogen production in the water-gas shift reaction: activity, structure and reaction mechanism. *Physical Chemistry Chemical Physics* **2006,** *8* (47), 5483-5500.

106. Grunwaldt, J. D.; Kiener, C.; Wogerbauer, C.; Baiker, A., Preparation of supported gold catalysts for low-temperature CO oxidation via "size-controlled" gold colloids. *Journal of Catalysis* **1999,** *181* (2), 223-232.

107. Gottfried, J. M.; Schmidt, K. J.; Schroeder, S. L. M.; Christmann, K., Adsorption of carbon monoxide on Au(110)-(1 x 2). *Surface Science* **2003,** *536* (1-3), 206-224.

108. Gluhoi, A. C.; Bogdanchikova, N.; Nieuwenhuys, B. E., Alkali (earth)-doped Au/Al2O3 catalysts for the total oxidation of propene. *Journal of Catalysis* **2005,** *232* (1), 96-101.

109. Janssens, T. V. W.; Clausen, B. S.; Hvolbaek, B.; Falsig, H.; Christensen, C. H.; Bligaard, T.; Norskov, J. K., Insights into the reactivity of supported Au nanoparticles: combining theory and experiments. *Topics in Catalysis* **2007,** *44* (1-2), 15-26.

110. Chen, M. S.; Goodman, D. W., The structure of catalytically active gold on titania. *Science* **2004,** *306* (5694), 252-255.

111. Haruta, M., Size- and support-dependency in the catalysis of gold. *Catalysis Today* **1997,** *36* (1), 153-166.

112. Mavrikakis, M.; Stoltze, P.; Norskov, J. K., Making gold less noble. *Catalysis Letters* **2000,** *64* (2-4), 101-106.

113. Gottfried, J. M.; Schmidt, K. J.; Schroeder, S. L. M.; Christmann, K., Spontaneous and electron-induced adsorption of oxygen on Au(110)-(1 x 2). *Surface Science* **2002,** *511* (1-3), 65-82.

114. Gottfried, J. M.; Christmann, K., Oxidation of carbon monoxide over Au(110)-(1 x 2). *Surface Science* **2004,** *566*, 1112-1117.

115. Grisel, R. J. H.; Weststrate, C. J.; Goossens, A.; Craje, M. W. J.; van der Kraan, A. M.; Nieuwenhuys, B. E., Oxidation of CO over Au/MOx/Al2O3 multi-component catalysts in a hydrogen-rich environment. *Catalysis Today* **2002,** *72* (1-2), 123-132.

116. Guzman, J.; Gates, B. C., Catalysis by supported gold: Correlation between catalytic activity for CO oxidation and oxidation states of gold. *Journal of the American Chemical Society* **2004,** *126* (9), 2672-2673.

117. Tabakova, T.; Boccuzzi, F. B.; Manzoli, M.; Andreeva, D., FTIR study of low-temperature water-gas shift reaction on gold/ceria catalyst. *Applied Catalysis a-General* **2003,** *252* (2), 385-397.

118. Daly, H.; Goguet, A.; Hardacre, C.; Meunier, F. C.; Pilasombat, R.; Thompsett, D., The effect of reaction conditions on the stability of Au/CeZrO4 catalysts in the low-temperature water-gas shift reaction. *Journal of Catalysis* **2010,** *273* (2), 257-265.

119. Lopez, N.; Janssens, T. V. W.; Clausen, B. S.; Xu, Y.; Mavrikakis, M.; Bligaard, T.; Norskov, J. K., On the origin of the catalytic activity of gold nanoparticles for low-temperature CO oxidation. *Journal of Catalysis* **2004,** *223* (1), 232-235.

120. Han, M. M.; Wang, X. J.; Shen, Y. N. A.; Tang, C. H.; Li, G. S.; Smith, R. L., Preparation of Highly Active, Low Au-Loaded, Au/CeO2 Nanoparticle Catalysts That Promote CO Oxidation at Ambient Temperatures. *Journal of Physical Chemistry C* **2010,** *114* (2), 793-798.

121. Lopez-Haro, M.; Delgado, J. J.; Cies, J. M.; del Rio, E.; Bernal, S.; Burch, R.; Cauqui, M. A.; Trasobares, S.; Perez-Omil, J. A.; Bayle-Guillemaud, P.; Calvino, J. J., Bridging the Gap between CO Adsorption Studies on Gold Model Surfaces and Supported Nanoparticles. *Angewandte Chemie-International Edition* **2010,** *49* (11), 1981-1985.

122. Hammer, B.; Norskov, J. K., Why Gold Is the Noblest of All the Metals. *Nature* **1995,** *376* (6537), 238-240.

123. Yoon, B.; Hakkinen, H.; Landman, U., Interaction of O-2 with gold clusters: Molecular and dissociative adsorption. *Journal of Physical Chemistry A* **2003,** *107* (20), 4066-4071.

124. Azzam, K. G.; Babich, I. V.; Seshan, K.; Lefferts, L., Single stage water gas shift conversion over Pt/TiO2 - Problem of catalyst deactivation. *Applied Catalysis a-General* **2008,** *338* (1-2), 66-71.

125. Ruettinger, W.; Liu, X. S.; Farrauto, R. J., Mechanism of aging for a Pt/CeO2-ZrO2 water gas shift catalyst. *Applied Catalysis B-Environmental* **2006,** *65* (1-2), 135-141.

126. Wang, X.; Gorte, R. J.; Wagner, J. P., Deactivation Mechanisms for Pd/Ceria during the Water-Gas-Shift Reaction. *Journal of Catalysis* **2002,** *212* (2), 225-230.

127. Iida, H.; Igarashi, A., Difference in the reaction behavior between Pt-Re/TiO2 (Rutile) and Pt-Re/ZrO2 catalysts for low-temperature water gas shift reactions. *Applied Catalysis a-General* **2006,** *303* (1), 48-55.

128. Yeung, C. M. Y.; Tsang, S. C., Some optimization in preparing core-shell Pt-ceria catalysts for water gas shift reaction. *J. Mol. Catal. A-Chem.* **2010,** *322* (1-2), 17-25.

129. Ma, Z.; Yin, H. F.; Dai, S., Performance of Au/MxOy/TiO2 Catalysts in Water-Gas Shift Reaction. *Catalysis Letters* **2010,** *136* (1-2), 83-91.

130. Wang, Y. A.; Liang, S. A.; Cao, A. M.; Thompson, R. L.; Veser, G., Au-mixed lanthanum/cerium oxide catalysts for water gas shift. *Applied Catalysis B-Environmental* **2010,** *99* (1-2), 89-95.

131. Gupta, A.; Hegde, M. S., Ce0.78Sn0.2Pt0.02O2-delta: A new non-deactivating catalyst for hydrogen production via water-gas shift reaction. *Applied Catalysis B-Environmental* **2010,** *99* (1-2), 279-288.

132. Cargnello, M.; Montini, T.; Polizzi, S.; Wieder, N. L.; Gorte, R. J.; Graziani, M.; Fornasiero, P., Novel embedded Pd@CeO2 catalysts: a way to active and stable catalysts. *Dalton Transactions* **2010,** *39* (8), 2122-2127.

133. Pierre, D.; Deng, W.; Flytzani-Stephanopoulos, M., The Importance of Strongly Bound Pt–CeO x; Species for the Water-gas Shift Reaction: Catalyst Activity and Stability Evaluation
Topics in Catalysis **2007,** *46* (3), 363-373.

134. Bera, P.; Malwadkar, S.; Gayen, A.; Satyanarayana, C. V. V.; Rao, B. S.; Hegde, M. S., Low-temperature water gas shift reaction on combustion synthesized Ce1-xPtxO2-delta catalyst. *Catalysis Letters* **2004,** *96* (3-4), 213-219.

135. Zhou, Y. H.; Zhou, J., Growth and Sintering of Au-Pt Nanoparticles on Oxidized and Reduced CeOx(111) Thin Films by Scanning Tunneling Microscopy. *Journal of Physical Chemistry Letters* **2010,** *1* (3), 609-615.

136. Hurtado-Juan, M. A.; Yeung, C. M. Y.; Tsang, S. C., A study of co-precipitated bimetallic gold catalysts for water-gas shift reaction. *Catal. Commun.* **2008,** *9* (7), 1551-1557.

137. Andreeva, D.; Ivanov, I.; Ilieva, L.; Sobczak, J. W.; Avdeev, G.; Petrov, K., Gold based catalysts on ceria and ceria-alumina for WGS reaction (WGS Gold catalysts). *Topics in Catalysis* **2007,** *44* (1-2), 173-182.

138. Zhou, H. P.; Wu, H. S.; Shen, J.; Yin, A. X.; Sun, L. D.; Yan, C. H., Thermally Stable Pt/CeO2 Hetero-Nanocomposites with High Catalytic Activity. *Journal of the American Chemical Society* **2010,** *132* (14), 4998.

139. Gorte, R. J., Ceria in Catalysis: From Automotive Applications to the Water Gas Shift Reaction. *Aiche J.* **2010,** *56* (5), 1126-1135.

140. Flytzani-Stephanopoulos, M.; Voecks, G. E.; Charng, T., Modelling of heat transfer in non-adiabatic monolith reactors and experimental comparisons of metal monoliths with packed beds. *Chemical Engineering Science* **1986,** *41* (5), 1203-1212.

141. Kwon, H. J.; Baik, J. H.; Kang, S. B.; Nam, I.-S.; Yoon, B. J.; Oh, S. H., Simulation of a Nonisothermal Modern Three-Way Catalyst Converter. *Industrial & Engineering Chemistry Research* **2010,** *49* (15), 7039-7051.

142. Kim, J.; Reitz, R. D.; Park, S. W.; Sung, K., Reduction in NOX and CO Emissions in Stoichiometric Diesel Combustion Using a Three-Way Catalyst. *Journal of*

Engineering for Gas Turbines and Power-Transactions of the Asme **2010,** *132* (7), 072803.

143. Wang, Q. Y.; Zhao, B.; Li, G. F.; Zhou, R. X., Application of Rare Earth Modified Zr-based Ceria-Zirconia Solid Solution in Three-Way Catalyst for Automotive Emission Control. *Environmental Science & Technology* **2010,** *44* (10), 3870-3875.

144. Li, G. F.; Zhao, B.; Wang, Q. Y.; Zhou, R. X., The effect of Ni on the structure and catalytic behavior of model Pd/Ce0.67Zr0.33O2 three-way catalyst before and after aging. *Applied Catalysis B-Environmental* **2010,** *97* (1-2), 41-48.

145. Li, G. F.; Wang, Q. Y.; Zhao, B.; Zhou, R. X., Modification of Ce0.67Zr0.33O2 mixed oxides by coprecipitated/impregnated Co: Effect on the surface and catalytic behavior of Pd only three-way catalyst. *J. Mol. Catal. A-Chem.* **2010,** *326* (1-2), 69-74.

146. Bartley, G. J. J.; Shady, P. J.; D'Aniello, M. J.; Chandler, G. R.; Brisley, R. J.; Webster, D. E., *Society of Automotive Engineers Paper No. 930076* **1993**.

147. Funabiki, M.; Yamada, T., *Society of Automotive Engineers Paper No. 881684* **1988**.

148. Cuif, J. P.; Deutsch, S.; Marczi, M.; Jen, H. W.; Graham, G. W.; Chun, W.; McCabe, R. W., *Society of Automotive Engineers Paper No. 980668* **1998**.

149. Jen, H. W.; Graham, G. W.; Chun, W.; McCabe, R. W.; Cuif, J. P.; Deutsch, S. E.; Touret, O., Characterization of model automotive exhaust catalysts: Pd on ceria and ceria-zirconia supports. *Catalysis Today* **1999,** *50* (2), 309-328.

150. Avgouropoulos, G.; Papavasiliou, J.; Ioannides, T., Hydrogen production from methanol over combustion-synthesized noble metal/ceria catalysts. *Chemical Engineering Journal* **2009,** *154* (1-3), 274-280.

151. Romero-Sarria, F.; Vargas, J. C.; Roger, A. C.; Kiennemann, A., Hydrogen production by steam reforming of ethanol Study of mixed oxide catalysts Ce2Zr1.5Me0.5O8: Comparison of Ni/Co and effect of Rh. *Catalysis Today* **2008,** *133*, 149-153.

152. Fajardo, H. V.; Probst, L. F. D.; Carreno, N. L. V.; Garcia, I. T. S.; Valentini, A., Hydrogen production from ethanol steam reforming over Ni/CeO2 nanocomposite catalysts. *Catalysis Letters* **2007,** *119* (3-4), 228-236.

153. Jalowiecki-Duhamel, L.; Pirez, C.; Capron, M.; Dumeignil, F.; Payen, E., Hydrogen production from ethanol in presence of water over cerium and nickel mixed oxides. In *6th World Congress on Oxidation Catalysis Lille, France, 5-10 July 2009 Towards an integrated approach in innovation and development*, 2010; Vol. 157, pp 456-461.

154. Zhou, G.; Barrio, L.; Agnoli, S.; Senanayake, S. D.; Evans, J.; Kubacka, A.; Estrella, M.; Hanson, J. C.; Martínez-Arias, A.; Fernández-García, M.; Rodriguez, J. A., High Activity of Ce1−xNixO2−y for H2 Production through Ethanol Steam Reforming: Tuning Catalytic Performance through Metal–Oxide Interactions. *Angewandte Chemie International Edition* **2010**, 9680-9684.

155. Karatzas, X.; Creaser, D.; Grant, A.; Dawody, J.; Pettersson, L. J., Hydrogen generation from n-tetradecane, low-sulfur and Fischer-Tropsch diesel over Rh supported on alumina doped with ceria/lanthana. *Catalysis Today* **2010,** *In Press, Corrected Proof*.

156. Torres Sanchez, R. M.; Ueda, A.; Tanaka, K.; Haruta, M., Selective Oxidation of CO in Hydrogen over Gold Supported on Manganese Oxides. *Journal of Catalysis* **1997,** *168* (1), 125-127.

157. Ilieva, L.; Pantaleo, G.; Ivanov, I.; Maximova, A.; Zanella, R.; Kaszkur, Z.; Venezia, A. M.; Andreeva, D., Preferential oxidation of CO in H2 rich stream (PROX) over gold catalysts supported on doped ceria: Effect of preparation method and nature of dopant. *Catalysis Today* **2010,** *158* (1-2), 44-55.

158. Haruta, M.; Tsubota, S.; Kobayashi, T.; Kageyama, H.; Genet, M. J.; Delmon, B., Low-Temperature Oxidation of Co over Gold Supported on Tio2, Alpha-Fe2o3, and Co3o4. *Journal of Catalysis* **1993,** *144* (1), 175-192.

159. Grisel, R. J. H.; Nieuwenhuys, B. E., Selective oxidation of CO over supported Au catalysts. *Journal of Catalysis* **2001,** *199* (1), 48-59.

160. Gnanamani, M. K.; Ribeiro, M. C.; Ma, W.; Shafer, W. D.; Jacobs, G.; Graham, U. M.; Davis, B. H., Fischer Tropsch synthesis: metal-support interfacial contact governs oxygenates selectivity over CeO2 supported Pt-Co catalysts. *Applied Catalysis A: General* **2010,** *In Press, Accepted Manuscript*.

161. Ganduglia-Pirovano, M. V.; Hofmann, A.; Sauer, J., Oxygen vacancies in transition metal and rare earth oxides: Current state of understanding and remaining challenges. *Surface Science Reports* **2007,** *62* (6), 219-270.

162. Gritschneder, S.; Reichling, M., Structural elements of CeO 2 (111) surfaces. *Nanotechnology* **2007,** *18* (4), 044024.

163. Jacobs, G.; Graham, U. M.; Chenu, E.; Patterson, P. M.; Dozier, A.; Davis, B. H., Low-temperature water-gas shift: impact of Pt promoter loading on the partial reduction of ceria and consequences for catalyst design. *Journal of Catalysis* **2005,** *229* (2), 499-512.

164. Jacobs, G.; Crawford, A.; Williams, L.; Patterson, P. M.; Davis, B. H., Low temperature water-gas shift: comparison of thoria and ceria catalysts. *Applied Catalysis a-General* **2004,** *267* (1-2), 27-33.

165. Esch, F.; Fabris, S.; Zhou, L.; Montini, T.; Africh, C.; Fornasiero, P.; Comelli, G.; Rosei, R., Electron localization determines defect formation on ceria substrates. *Science* **2005,** *309* (5735), 752-755.

166. Torbrugge, S.; Reichling, M.; Ishiyama, A.; Morita, S.; Custance, O., Evidence of subsurface oxygen vacancy ordering on reduced CeO2(111). *Physical Review Letters* **2007,** *99* (5), 056101.

167. Baidya, T.; Gayen, A.; Hegde, M. S.; Ravishankar, N.; Dupont, L., Enhanced reducibility of Ce1-xTixO2 compared to that of CeO2 and higher redox catalytic activity of Ce1-x-yTixPtyO2-delta compared to that of Ce1-xPtxO2-delta. *Journal of Physical Chemistry B* **2006,** *110* (11), 5262-5272.

168. Colón, G.; Valdivieso, F.; Pijolat, M.; Baker, R. T.; Calvino, J. J.; Bernal, S., Textural and phase stability of CexZr1-xO2 mixed oxides under high temperature oxidising conditions. *Catalysis Today* **1999,** *50* (2), 271-284.

169. Fornasiero, P.; Balducci, G.; Di Monte, R.; Kaspar, J.; Sergo, V.; Gubitosa, G.; Ferrero, A.; Graziani, M., Modification of the Redox Behaviour of CeO2Induced by Structural Doping with ZrO2. *Journal of Catalysis* **1996,** *164* (1), 173-183.

170. Campbell, C. T.; Peden, C. H. F., Oxygen vacancies and catalysis on ceria surfaces. *Science* **2005,** *309* (5735), 713-714.

171. Martin, D.; Duprez, D., Mobility of surface species on oxides .1. Isotopic exchange O-18(2) with O-16 of SiO2, Al2O3, ZrO2, MgO, CeO2, and CeO2-Al2O3. Activation by noble metals. Correlation with oxide basicity. *Journal of Physical Chemistry* **1996,** *100* (22), 9429-9438.

172. Zhang, C. J.; Michaelides, A.; King, D. A.; Jenkins, S. J., Anchoring Sites for Initial Au Nucleation on CeO2{111}: O Vacancy versus Ce Vacancy. *Journal of Physical Chemistry C* **2009,** *113* (16), 6411-6417.

173. Chen, Y.; Hu, P.; Lee, M. H.; Wang, H. F., Au on (111) and (110) surfaces of CeO2: A density-functional theory study. *Surface Science* **2008,** *602* (10), 1736-1741.

174. Sanchez, M. G.; Gazquez, J. L., Oxygen vacancy model in strong metal-support interaction. *Journal of Catalysis* **1987,** *104* (1), 120-135.

175. Zhai, Y.; Pierre, D.; Si, R.; Deng, W.; Ferrin, P.; Nilekar, A. U.; Peng, G.; Herron, J. A.; Bell, D. C.; Saltsburg, H.; Mavrikakis, M.; Flytzani-Stephanopoulos, M., Alkali-Stabilized Pt-OHx Species Catalyze Low-Temperature Water-Gas Shift Reactions. *Science* **2010,** *329* (5999), 1633-1636.

176. Kwak, J. H.; Hu, J.; Mei, D.; Yi, C.-W.; Kim, D. H.; Peden, C. H. F.; Allard, L. F.; Szanyi, J., Coordinatively Unsaturated Al3+ Centers as Binding Sites for Active Catalyst Phases of Platinum on Î³-Al2O3. *Science* **2009,** *325* (5948), 1670-1673.

177. Rodriguez, J. A.; Wang, X.; Liu, P.; Wen, W.; Hanson, J. C.; Hrbek, J.; Perez, M.; Evans, J., Gold nanoparticles on ceria: importance of O vacancies in the activation of gold. *Topics in Catalysis* **2007,** *44* (1-2), 73-81.

178. Norskov, J. K.; Bligaard, T.; Hvolbaek, B.; Abild-Pedersen, F.; Chorkendorff, I.; Christensen, C. H., The nature of the active site in heterogeneous metal catalysis. *Chemical Society Reviews* **2008,** *37* (10), 2163-2171.

179. Somorjai, G. A.; Li, Y. M., Major Successes of Theory-and-Experiment-Combined Studies in Surface Chemistry and Heterogeneous Catalysis. *Topics in Catalysis* **2010,** *53* (5-6), 311-325.

180. Cheng, J.; Hu, P., Utilization of the three-dimensional volcano surface to understand the chemistry of multiphase systems in heterogeneous catalysis. *Journal of the American Chemical Society* **2008,** *130* (33), 10868-10869.

181. Tauster, S. J.; Fung, S. C.; Garten, R. L., Strong metal-support interactions. Group 8 noble metals supported on titanium dioxide. *Journal of the American Chemical Society* **1978,** *100* (1), 170-175.

182. Tauster, S. J., Strong metal-support interactions. *Accounts of Chemical Research* **1987,** *20* (11), 389-394.

183. Cohen, A. J.; Mori-Sanchez, P.; Yang, W., Insights into Current Limitations of Density Functional Theory. *Science* **2008,** *321* (5890), 792-794.

184. Kullgren, J.; Castleton, C. W. M.; Muller, C.; Ramo, D. M.; Hermansson, K., B3LYP calculations of cerium oxides. *Journal of Chemical Physics* **2010,** *132* (5), 054110.

185. Lee, Y.-L.; Kleis, J.; Rossmeisl, J.; Morgan, D., Ab initio energetics of LaBO_{3}(001) (B=Mn , Fe, Co, and Ni) for solid oxide fuel cell cathodes. *Physical Review B* **2009,** *80* (22), 224101.

186. Wang, L.; Maxisch, T.; Ceder, G., Oxidation energies of transition metal oxides within the GGA+U framework. *Physical Review B* **2006,** *73* (19), 195107.

187. Barcaro, G.; Thomas, I. O.; Fortunelli, A., Validation of density-functional versus density-functional plus U approaches for oxide ultrathin films. *Journal of Chemical Physics* **2010,** *132* (12), 124703.

188. Ricardo, G.-C.; et al., Vacancy ordering and electronic structure of Î³ - Fe 2 O 3 (maghemite): a theoretical investigation. *Journal of Physics: Condensed Matter* **2010,** *22* (25), 255401.

189. Devey, A. J.; Grau-Crespo, R.; de Leeuw, N. H., Electronic and magnetic structure of Fe3S4: GGA+U investigation. *Physical Review B* **2009,** *79* (19), 195126.

190. Da Silva, J. L. F.; Ganduglia-Pirovano, M. V.; Sauer, J.; Bayer, V.; Kresse, G., Hybrid functionals applied to rare-earth oxides: The example of ceria. *Physical Review B* **2007,** *75* (4), 045121.

191. Herschend, B.; Baudin, M.; Hermansson, K., CO adsorption on CeO2(110) using hybrid-DFT embedded-cluster calculations. *Chemical Physics* **2006,** *328* (1-3), 345-353.

192. Ammal, S. C.; Heyden, A., Modeling the noble metal/TiO2 (110) interface with hybrid DFT functionals: A periodic electrostatic embedded cluster model study. *Journal of Chemical Physics* **2010,** *133* (16), 164703.

193. Burow, A. M.; Sierka, M.; Dobler, J.; Sauer, J., Point defects in CaF2 and CeO2 investigated by the periodic electrostatic embedded cluster method. *Journal of Chemical Physics* **2009,** *130* (17), 174710.

194. Muller, C.; Freysoldt, C.; Baudin, M.; Hermansson, K., An ab initio study of CO adsorption on ceria(110). *Chemical Physics* **2005,** *318* (3), 180-190.

195. Endou, A.; Onuma, H.; Jung, S. H.; Ishimoto, R.; Tsuboi, H.; Koyama, M.; Takaba, H.; Kubo, M.; Del Carpio, C. A.; Miyamoto, A., Development of constraint algorithm for the number of electrons in molecular orbitals consisting mainly 4f atomic orbitals of rare-earth elements and its introduction to tight-binding quantum chemical molecular dynamics method. *Japanese Journal of Applied Physics Part 1-Regular Papers Brief Communications & Review Papers* **2007,** *46* (4B), 2505-2509.

196. Jung, S.; Suzuki, A.; Tsuboi, H.; Hatakeyama, N.; Endou, A.; Takaba, H.; Kubo, M.; Miyamoto, A., An Elucidation of the Interaction Between Pt Particles and CeO2 Surfaces Using Tight-Binding Quantum Chemistry Method. *Topics in Catalysis* **2010,** *53* (7-10), 700-706.

197. Ishimoto, R.; Jung, C. H.; Tsuboi, H.; Koyama, M.; Endou, A.; Kubo, M.; Del Carpio, C. A.; Miyamoto, A., Periodic density functional and tight-binding quantum chemical molecular dynamics study of catalytic properties on gamma-Al2O3 supported Pt catalysts. *Applied Catalysis a-General* **2006,** *305* (1), 64-69.

198. Herschend, B.; Baudin, M.; Hermansson, K., A combined molecular dynamics plus quantum mechanics method for investigation of dynamic effects on local surface structures. *Journal of Chemical Physics* **2004,** *120* (10), 4939-4948.

199. Ganduglia-Pirovano, M. V.; Da Silva, J. L. F.; Sauer, J., Density-Functional Calculations of the Structure of Near-Surface Oxygen Vacancies and Electron Localization on CeO2(111). *Physical Review Letters* **2009,** *102* (2), 026101.

200. Nolan, M., Hybrid density functional theory description of oxygen vacancies in the CeO2 (110) and (100) surfaces. *Chemical Physics Letters* **2010,** *499* (1-3), 126-130.

201. Nolan, M.; Grigoleit, S.; Sayle, D. C.; Parker, S. C.; Watson, G. W., Density functional theory studies of the structure and electronic structure of pure and defective low index surfaces of ceria. *Surface Science* **2005,** *576* (1-3), 217-229.

202. Yang, Z. X.; Woo, T. K.; Hermansson, K., Strong and weak adsorption of CO on CeO2 surfaces from first principles calculations. *Chemical Physics Letters* **2004,** *396* (4-6), 384-392.

203. Yang, Z. X.; Lu, Z. S.; Luo, G. X., First-principles study of the Pt/CeO2(111) interface. *Physical Review B* **2007,** *76* (7), 075421.

204. Lu, Z. S.; Yang, Z. X., Interfacial properties of NM/CeO2(111) (NM = noble metal atoms or clusters of Pd, Pt and Rh): a first principles study. *Journal of Physics-Condensed Matter* **2010,** *22* (47), 475003.

205. Bruix, A.; Neyman, K. M.; Illas, F., Adsorption, Oxidation State, and Diffusion of Pt Atoms on the CeO2(111) Surface. *Journal of Physical Chemistry C* **2010,** *114* (33), 14202-14207.

206. Li, B. H.; Ezekoye, O. K.; Zhang, Q. J.; Chen, L. A.; Cui, P.; Graham, G.; Pan, X. Q., Origin of Rh and Pd agglomeration on the CeO2(111) surface. *Physical Review B* **2010,** *82* (12), 125422.

207. Mayernick, A. D.; Janik, M. J., Ab initio thermodynamic evaluation of Pd atom interaction with CeO2 surfaces. *Journal of Chemical Physics* **2009,** *131* (8), 084701.

208. Jung, C.; Tsuboi, H.; Koyama, M.; Kubo, M.; Broclawik, E.; Miyamoto, A., Different support effect of M/ZrO2 and M/CeO2 (M=Pd and Pt) catalysts on CO adsorption: A periodic density functional study. *Catalysis Today* **2006,** *111* (3-4), 322-327.

209. Liu, Z. P.; Jenkins, S. J.; King, D. A., Origin and activity of oxidized gold in water-gas-shift catalysis. *Physical Review Letters* **2005,** *94* (19), 196102.

210. Branda, M. M.; Castellani, N. J.; Grau-Crespo, R.; de Leeuw, N. H.; Hernandez, N. C.; Sanz, J. F.; Neyman, K. M.; Illas, F., On the difficulties of present theoretical models to predict the oxidation state of atomic Au adsorbed on regular sites of CeO2(111). *Journal of Chemical Physics* **2009,** *131* (9), 094702.

211. Liechtenstein, A. I.; Anisimov, V. I.; Zaanen, J., Density-Functional Theory and Strong-Interactions - Orbital Ordering in Mott-Hubbard Insulators. *Physical Review B* **1995,** *52* (8), R5467-R5470.

212. Dudarev, S. L.; Botton, G. A.; Savrasov, S. Y.; Humphreys, C. J.; Sutton, A. P., Electron-energy-loss spectra and the structural stability of nickel oxide: An LSDA+U study. *Physical Review B* **1998,** *57* (3), 1505-1509.

213. Shick, A. B.; Pickett, W. E.; Liechtenstein, A. I., Ground and metastable states in [gamma]-Ce from correlated band theory. *Journal of Electron Spectroscopy and Related Phenomena* **2001,** *114-116*, 753-758.

214. Harris, J., Simplified method for calculating the energy of weakly interacting fragments. *Physical Review B* **1985,** *31* (4), 1770.

215. Foulkes, W. M. C.; Haydock, R., Tight-binding models and density-functional theory. *Physical Review B* **1989,** *39* (17), 12520.

216. Henkelman, G.; Uberuaga, B. P.; Jonsson, H., A climbing image nudged elastic band method for finding saddle points and minimum energy paths. *Journal of Chemical Physics* **2000,** *113* (22), 9901-9904.

217. Heyden, A.; Bell, A. T.; Keil, F. J., Efficient methods for finding transition states in chemical reactions: Comparison of improved dimer method and partitioned rational function optimization method. *Journal of Chemical Physics* **2005,** *123* (22).

218. Reuter, K.; Scheffler, M., First-principles kinetic Monte Carlo simulations for heterogeneous catalysis: Application to the CO oxidation at RuO2(110). *Physical Review B* **2006,** *73* (4), 045433.

219. Temel, B.; Meskine, H.; Reuter, K.; Scheffler, M.; Metiu, H., Does phenomenological kinetics provide an adequate description of heterogeneous catalytic reactions? *Journal of Chemical Physics* **2007,** *126* (20), 204711.

220. Reuter, K.; Scheffler, M., Composition, structure, and stability of RuO_{2}(110) as a function of oxygen pressure. *Physical Review B* **2001,** *65* (3), 035406.

221. Wang, X. G.; Chaka, A.; Scheffler, M., Effect of the environment on alpha-Al2O3 (0001) surface structures. *Physical Review Letters* **2000,** *84* (16), 3650-3653.

222. Wang, X. G.; Weiss, W.; Shaikhutdinov, S. K.; Ritter, M.; Petersen, M.; Wagner, F.; Schlogl, R.; Scheffler, M., The hematite (alpha-Fe2O3) (0001) surface: Evidence for domains of distinct chemistry. *Physical Review Letters* **1998,** *81* (5), 1038-1041.

223. Laursen, S.; Linic, S., Strong Chemical Interactions Between Au and Off-Stoichiometric Defects on TiO2 as a Possible Source of Chemical Activity of Nanosized Au Supported on the Oxide. *Journal of Physical Chemistry C* **2009,** *113* (16), 6689-6693.

224. Stegelmann, C.; Andreasen, A.; Campbell, C. T., Degree of Rate Control: How Much the Energies of Intermediates and Transition States Control Rates. *Journal of the American Chemical Society* **2009,** *131* (23), 8077-8082.

225. Pierre, D.; Deng, W. L.; Flytzani-Stephanopoulos, M., The importance of strongly bound Pt-CeOx species for the water-gas shift reaction: Catalyst activity and stability evaluation. *Topics in Catalysis* **2007,** *46* (3-4), 363-373.

226. Leppelt, R.; Schumacher, B.; Plzak, V.; Kinne, M.; Behm, R. J., Kinetics and mechanism of the low-temperature water-gas shift reaction on Au/CeO2 catalysts in an idealized reaction atmosphere. *Journal of Catalysis* **2006,** *244* (2), 137-152.

227. Ou, D. R.; Mori, T.; Togasaki, H.; Takahashi, M.; Ye, F.; Drennan, J., Microstructural and Metal-Support Interactions of the Pt-CeO2/C Catalysts for Direct Methanol Fuel Cell Application. *Langmuir* **2011,** *27* (7), 3859-3866.

228. Vayssilov, G. N.; Lykhach, Y.; Migani, A.; Staudt, T.; Petrova, G. P.; Tsud, N.; Skala, T.; Bruix, A.; Illas, F.; Prince, K. C.; Matolin, V.; Neyman, K. M.; Libuda, J., Support nanostructure boosts oxygen transfer to catalytically active platinum nanoparticles. *Nature Materials* **2011,** *10* (4), 310-315.

229. Zhou, Y. H.; Perket, J. M.; Zhou, J., Growth of Pt Nanoparticles on Reducible CeO2(111) Thin Films: Effect of Nanostructures and Redox Properties of Ceria. *Journal of Physical Chemistry C* **2010,** *114* (27), 11853-11860.

230. Zhou, J.; Baddorf, A. P.; Mullins, D. R.; Overbury, S. H., Growth and characterization of Rh and Pd nanoparticles on oxidized and reduced CeOx(111) thin films by scanning tunneling microscopy. *Journal of Physical Chemistry C* **2008,** *112* (25), 9336-9345.

231. Lu, J. L.; Gao, H. J.; Shaikhutdinov, S.; Freund, H. J., Gold supported on well-ordered ceria films: nucleation, growth and morphology in CO oxidation reaction. *Catalysis Letters* **2007,** *114* (1-2), 8-16.

232. Zhang, C.; Michaelides, A.; King, D. A.; Jenkins, S. J., Positive Charge States and Possible Polymorphism of Gold Nanoclusters on Reduced Ceria. *Journal of the American Chemical Society* **2010,** *132* (7), 2175-2182.

233. Loffreda, D.; Delbecq, F., Growth of a Pt film on non-reduced ceria: A density functional theory study. *Journal of Chemical Physics* **2012,** *136* (4).

234. Meunier, F. C.; Tibiletti, D.; Goguet, A.; Shekhtman, S.; Hardacre, C.; Burch, R., On the complexity of the water-gas shift reaction mechanism over a Pt/CeO2 catalyst: Effect of the temperature on the reactivity of formate surface species studied by operando DRIFT during isotopic transient at chemical steady-state. *Catalysis Today* **2007,** *126* (1-2), 143-147.

235. Kalamaras, C. M.; Gonzalez, I. D.; Navarro, R. M.; Fierro, J. L. G.; Efstathiou, A. M., Effects of Reaction Temperature and Support Composition on the Mechanism of Water-Gas Shift Reaction over Supported-Pt Catalysts. *Journal of Physical Chemistry C* **2011,** *115* (23), 11595-11610.

236. Kalamaras, C. M.; Americanou, S.; Efstathiou, A. M., "Redox" vs "associative formate with -OH group regeneration" WGS reaction mechanism on Pt/CeO2: Effect of platinum particle size. *Journal of Catalysis* **2011,** *279* (2), 287-300.

237. Meunier, F. C.; Tibiletti, D.; Goguet, A.; Reid, D.; Burch, R., On the reactivity of carbonate species on a Pt/CeO2 catalyst under various reaction atmospheres: Application of the isotopic exchange technique. *Applied Catalysis a-General* **2005,** *289* (1), 104-112.

238. Yao, H. C.; Yao, Y. F. Y., Ceria in automotive exhaust catalysts : I. Oxygen storage. *Journal of Catalysis* **1984,** *86* (2), 254-265.

239. Lykhach, Y.; Staudt, T.; Lorenz, M. P. A.; Streber, R.; Bayer, A.; Steinruck, H. P.; Libuda, J., Microscopic Insights into Methane Activation and Related Processes on Pt/Ceria Model Catalysts. *Chemphyschem* **2010,** *11* (7), 1496-1504.

240. Matolin, V.; Libra, J.; Matolinova, I.; Nehasil, V.; Sedlacek, L.; Sutara, F., Growth of ultra-thin cerium oxide layers on Cu(111). *Applied Surface Science* **2007,** *254* (1), 153-155.

241. Bernal, S.; Calving, J. J.; Cifredo, G. A.; RodrÃ-guez-Izquierdo, J. M.; Perrichon, V.; Laachir, A., Reversibility of hydrogen chemisorption on a ceria-supported rhodium catalyst. *Journal of Catalysis* **1992,** *137* (1), 1-11.

242. Daturi, M.; Finocchio, E.; Binet, C.; Lavalley, J. C.; Fally, F.; Perrichon, V., Study of Bulk and Surface Reduction by Hydrogen of CexZr1-xO2 Mixed Oxides Followed by FTIR Spectroscopy and Magnetic Balance. *The Journal of Physical Chemistry B* **1999,** *103* (23), 4884-4891.

243. González, I. D.; Navarro, R. M.; Wen, W.; Marinkovic, N.; Rodriguéz, J. A.; Rosa, F.; Fierro, J. L. G., A comparative study of the water gas shift reaction over platinum catalysts supported on CeO2, TiO2 and Ce-modified TiO2. *Catalysis Today* **2010,** *149* (3-4), 372-379.

244. Yeo, Y. Y.; Vattuone, L.; King, D. A., Calorimetric heats for CO and oxygen adsorption and for the catalytic CO oxidation reaction on Pt{111}. *The Journal of Chemical Physics* **1997,** *106* (1), 392-401.

245. Rashkeev, S. N.; Lupini, A. R.; Overbury, S. H.; Pennycook, S. J.; Pantelides, S. T., Role of the nanoscale in catalytic CO oxidation by supported Au and Pt nanostructures. *Physical Review B* **2007,** *76* (3).

246. Grabow, L. C.; Gokhale, A. A.; Evans, S. T.; Dumesic, J. A.; Mavrikakis, M., Mechanism of the water gas shift reaction on Pt: First principles, experiments, and microkinetic modeling. *Journal of Physical Chemistry C* **2008,** *112* (12), 4608-4617.

247. Huang, M.; Fabris, S., CO adsorption and oxidation on ceria surfaces from DFT+U calculations. *Journal of Physical Chemistry C* **2008,** *112* (23), 8643-8648.

248. Kalamaras, C. M.; Panagiotopoulou, P.; Kondarides, D. I.; Efstathiou, A. M., Kinetic and mechanistic studies of the water-gas shift reaction on Pt/TiO2 catalyst. *Journal of Catalysis* **2009,** *264* (2), 117-129.

249. Meunier, F. C.; Yablonsky, G.; Reid, D.; Shekhtman, S. O.; Hardacre, C.; Burch, R.; Lazman, M., Negative apparent kinetic order in steady-state kinetics of the water-gas shift reaction over a Pt-CeO(2) catalyst. *Catalysis Today* **2008,** *138* (3-4), 216-221.

250. Azzam, K. G.; Babich, I. V.; Seshan, K.; Lefferts, L., Bifunctional catalysts for single-stage water-gas shift reaction in fuel cell applications. Part 1. Effect of the support on the reaction sequence. *Journal of Catalysis* **2007,** *251* (1), 153-162.

251. Efstathiou, A. M.; Kalamaras, C. M.; Americanou, S., "Redox" vs "associative formate with -OH group regeneration" WGS reaction mechanism on Pt/CeO(2): Effect of platinum particle size. *Journal of Catalysis* **2011,** *279* (2), 287-300.

252. Aranifard, S.; Ammal, S. C.; Heyden, A., Nature of Pt-n/CeO2 (111) Surface under Water-Gas Shift Reaction Conditions: A Constrained ab Initio Thermodynamics Study. *Journal of Physical Chemistry C* **2012,** *116* (16), 9029-9042.

253. Burch, R.; Goguet, A.; Meunier, F. C., A critical analysis of the experimental evidence for and against a formate mechanism for high activity water-gas shift catalysts. *Applied Catalysis a-General* **2011,** *409*, 3-12.

254. Meunier, F. C.; Yablonsky, G.; Reid, D.; Shekhtman, S. O.; Hardacre, C.; Burch, R.; Lazman, M., Negative apparent kinetic order in steady-state kinetics of the water-gas shift reaction over a Pt-CeO2 catalyst. *Catalysis Today* **2008,** *138* (3-4), 216-221.

255. Jacobs, G.; Williams, L.; Graham, U.; Thomas, G. A.; Sparks, D. E.; Davis, B. H., Low temperature water-gas shift: in situ DRIFTS-reaction study of ceria surface area on

the evolution of formates on Pt/CeO2 fuel processing catalysts for fuel cell applications. *Applied Catalysis a-General* **2003,** *252* (1), 107-118.

256. Zafiris, G. S.; Gorte, R. J., Evidence for Low-Temperature Oxygen Migration from Ceria to Rh. *Journal of Catalysis* **1993,** *139* (2), 561-567.

257. Sharma, S.; Hilaire, S.; Vohs, J. M.; Gorte, R. J.; Jen, H. W., Evidence for Oxidation of Ceria by CO2. *Journal of Catalysis* **2000,** *190* (1), 199-204.

258. Bruix, A.; Rodriguez, J. A.; Ramirez, P. J.; Senanayake, S. D.; Evans, J.; Park, J. B.; Stacchiola, D.; Liu, P.; Hrbek, J.; Illas, F., A New Type of Strong Metal-Support Interaction and the Production of H-2 through the Transformation of Water on Pt/CeO2(111) and Pt/CeOx/TiO2(110) Catalysts. *Journal of the American Chemical Society* **2012,** *134* (21), 8968-8974.

259. Grabow, L. C.; Gokhale, A. A.; Evans, S. T.; Dumesic, J. A.; Mavrikakis, M., Mechanism of the Water Gas Shift Reaction on Pt: First Principles, Experiments, and Microkinetic Modeling. *The Journal of Physical Chemistry C* **2008,** *112* (12), 4608-4617.

260. Mhadeshwar, A. B.; Vlachos, D. G., Microkinetic Modeling for Water-Promoted CO Oxidation, Water-Gas Shift, and Preferential Oxidation of CO on Pt. *The Journal of Physical Chemistry B* **2004,** *108* (39), 15246-15258.

261. Mhadeshwar, A. B.; Vlachos, D. G., Is the water-gas shift reaction on Pt simple? Computer-aided microkinetic model reduction, lumped rate expression, and rate-determining step. *Catalysis Today* **2005,** *105* (1), 162-172.

262. Chen, Y.; Wang, H. F.; Burch, R.; Hardacre, C.; Hu, P., New insight into mechanisms in water-gas-shift reaction on Au/CeO2(111): A density functional theory and kinetic study. *Faraday Discussions* **2011,** *152*, 121-133.

263. Phatak, A. A.; Koryabkina, N.; Rai, S.; Ratts, J. L.; Ruettinger, W.; Farrauto, R. J.; Blau, G. E.; Delgass, W. N.; Ribeiro, F. H., Kinetics of the water-gas shift reaction on Pt catalysts supported on alumina and ceria. *Catalysis Today* **2007,** *123* (1-4), 224-234.

264. Thinon, O.; Rachedi, K.; Diehl, F.; Avenier, P.; Schuurman, Y., Kinetics and Mechanism of the Water-Gas Shift Reaction Over Platinum Supported Catalysts. *Topics in Catalysis* **2009,** *52* (13-20), 1940-1945.

265. Merte, L. R.; Peng, G.; Bechstein, R.; Rieboldt, F.; Farberow, C. A.; Grabow, L. C.; Kudernatsch, W.; Wendt, S.; LÃ¦gsgaard, E.; Mavrikakis, M.; Besenbacher, F., Water-Mediated Proton Hopping on an Iron Oxide Surface. *Science* **2012,** *336* (6083), 889-893.

Appendix

Summary of the reaction steps that are explained in the text and the transition states structures for reactions

(R1) $*_{Pt}\text{-}O_{int} + CO_{(g)} \rightarrow CO_{Pt}\text{-}O_{int}$

(R2) $CO_{Pt}\text{-}O_{int} \rightarrow CO_{2(Pt\text{-}int)}$

(R3) $CO_{2(Pt\text{-}int)} \rightarrow *_{Pt}\text{-}V_{int} + CO_{2(g)}$

(R4) $*_{Pt}\text{-}V_{int} + H_2O_{(g)} \rightarrow H_2O_{(Pt)}\text{-}V_{int}$

(R5) $H_2O_{(Pt)}\text{-}V_{int} \rightarrow H_{Pt}\text{-}OH_{int}$

(R6) $H_{Pt}\text{-}OH_{int} + *_{Pt} \rightarrow 2H_{Pt}\text{-}O_{int}$

(R7) $2H_{Pt}\text{-}O_{int} \rightarrow *_{Pt}\text{-}O_{int} + H_{2(g)} + *_{Pt}$

(R8) $CO_{2(Pt\text{-}int)} + *_{Pt} + CO_{(g)} \rightarrow CO_{Pt}\text{-}CO_{2(Pt\text{-}int)}$

(R9) $CO_{Pt}\text{-}CO_{2(Pt\text{-}int)} \rightarrow CO_{Pt}\text{-}V_{(int)} + *_{Pt} + CO_{2(g)}$

(R10) $CO_{Pt}\text{-}V_{int} + H_2O_{(g)} \rightarrow CO_{Pt}\text{-}H_2O_{(int)}$

(R11) $CO_{Pt}\text{-}H_2O_{(int)} + *_{Pt} \rightarrow CO_{Pt}\text{-}H_{Pt}\text{-}OH_{int}$

(R12) $CO_{Pt}\text{-}H_{Pt}\text{-}OH_{int} + *_{Pt} \rightarrow CO_{Pt}\text{-}2H_{Pt}\text{-}O_{int}$

(R13) $CO_{Pt}\text{-}2H_{Pt}\text{-}O_{int} \rightarrow CO_{Pt}\text{-}O_{int} + H_{2(g)} + 2*_{Pt}$

(R14) $CO_{Pt}\text{-}H_{Pt}\text{-}OH_{int} \rightarrow COOH_{(Pt\text{-}int)}\text{-}H_{Pt}$

(R15) $CO_{Pt}\text{-}H_{Pt}\text{-}OH_{int} \rightarrow CHO_{(vert,Pt)}\text{-}O_{int}\text{-}H_{Pt}$

(R16) $CHO_{(vert,Pt)}$-O_{int}-H_{Pt} → $CHO_{(horiz,Pt)}$-O_{int}-H_{Pt}

(R17) $CHO_{(horiz,Pt)}$-O_{int}-H_{Pt} → $HCOO_{(Pt,int)}$-H_{Pt}

(R18) CO_{Pt}-$H_2O_{(int)}$ + O_s → CO_{Pt}-OH_s-OH_{int}

(R19) CO_{Pt}-OH_s-OH_{int} + $*_{Pt}$ → CO_{Pt}-H_{Pt}-O_{int}-OH_s

(R20) CO_{Pt}-H_{Pt}-O_{int}-OH_s + $*_{Ce}$ + $H_2O_{(g)}$ → CO_{Pt}-H_{Pt}-O_{int}-$H_2O_{(Ce)}$-OH_s

(R21) CO_{Pt}-H_{Pt}-O_{int}-$H_2O_{(Ce)}$-OH_s → CO_{Pt}-H_{Pt}-OH_{int}-OH_{Ce}-OH_s

(R22) CO_{Pt}-H_{Pt}-OH_{int}-OH_{Ce}-OH_s → CO_{Pt}-H_{Pt}-OH_{int}-$H_2O_{(Ce)}$-O_s

(R23) CO_{Pt}-H_{Pt}-OH_{int}-$H_2O_{(Ce)}$-O_s → CO_{Pt}-H_{Pt}-OH_{int} + O_s + $*_{Ce}$ + $H_2O_{(g)}$

(R24) CO_{Pt}-O_{int} + $H_2O_{(g)}$ + $*_{Ce}$ → CO_{Pt}-$H_2O_{(Ce)}$-O_{int}

(R25) CO_{Pt}-$H_2O_{(Ce)}$-O_{int} + O_s → CO_{Pt}-OH_{Ce}-O_{int}-OH_s

(R26) CO_{Pt}-OH_{Ce}-O_{int}-OH_s → $COOH_{Pt}$-O_{int}-OH_s + $*_{Ce}$

(R27) $COOH_{Pt}$-O_{int}-OH_s → $CO_{2(Pt)}$-OH_{int}-OH_s

(R28) $CO_{2(Pt)}$-OH_{int}-OH_s → $*_{Pt}$-OH_{int}-OH_s + $CO_{2(g)}$

(R29) $*_{Pt}$-OH_{int}-OH_s + $CO_{(g)}$ → CO_{Pt}-OH_{int}-OH_s

(R30) $*_{Pt}$-CO_{Pt}-O_{int} + $CO_{(g)}$ → $2CO_{Pt}$-O_{int}

(R31) $2CO_{Pt}$-O_{int} → $CO_{2(Pt\text{-}int)}$-CO_{Pt}

(R32) $CO_{2(Pt\text{-}int)}$-CO_{Pt} → $*_{Pt}$-CO_{Pt}-V_{int} + $CO_{2(g)}$

(R33) $*_{Pt}\text{-}CO_{Pt}\text{-}V_{int} + H_2O_{(g)} \rightarrow *_{Pt}\text{-}CO_{Pt}\text{-}H_2O_{(int)}$

(R34) $*_{Pt}\text{-}CO_{Pt}\text{-}H_2O_{(int)} \rightarrow CO_{Pt}\text{-}H_{Pt}\text{-}OH_{int}$

(R35) $CO_{Pt}\text{-}H_{Pt}\text{-}OH_{int} + *_{Pt} \rightarrow CO_{Pt}\text{-}2H_{Pt}\text{-}O_{int}$

(R36) $CO_{Pt}\text{-}2H_{Pt}\text{-}O_{int} \rightarrow *_{Pt}\text{-}CO_{Pt}\text{-}O_{int} + H_{2(g)} + *_{Pt}$

(R37) $*_{Pt}\text{-}CO_{Pt}\text{-}V_{int} + CO_{(g)} \rightarrow 2CO_{Pt}\text{-}V_{int}$

(R38) $2CO_{Pt}\text{-}V_{int} + H_2O_{(g)} \rightarrow 2CO_{Pt}\text{-}H_2O_{(int)}$

(R39) $2CO_{Pt}\text{-}H_2O_{(int)} + *_{Pt} \rightarrow 2CO_{Pt}\text{-}H_{Pt}\text{-}OH_{int}$

(R40) $2CO_{Pt}\text{-}H_{Pt}\text{-}OH_{int} + *_{Pt} \rightarrow 2CO_{Pt}\text{-}2H_{Pt}\text{-}O_{int}$

(R41) $2CO_{Pt}\text{-}2H_{Pt}\text{-}O_{int} \rightarrow 2CO_{Pt}\text{-}O_{int} + H_{2(g)} + 2*_{Pt}$

(R42) $2CO_{Pt}\text{-}H_2O_{(int)} + O_s \rightarrow 2CO_{Pt}\text{-}OH_{int}\text{-}OH_s$

(R43) $2CO_{Pt}\text{-}OH_{int}\text{-}OH_s \rightarrow COOH_{(Pt\text{-}int\text{-}I)}\text{-}CO_{Pt}\text{-}OH_s$

(R44) $COOH_{(Pt\text{-}int\text{-}I)}\text{-}CO_{Pt}\text{-}OH_s \rightarrow CO_{2(Pt\text{-}int)}\text{-}CO_{Pt}\text{-}OHH_s$

(R45) $CO_{2(Pt\text{-}int)}\text{-}CO_{Pt}\text{-}OHH_s \rightarrow COOH_{(Pt\text{-}int\text{-}II)}\text{-}CO_{Pt}\text{-}OH_s$

(R46) $COOH_{(Pt\text{-}int\text{-}II)}\text{-}CO_{Pt}\text{-}OH_s + *_{Pt} \rightarrow CO_{2(Pt\text{-}int)}\text{-}CO_{Pt}\text{-}H_{Pt}\text{-}OH_s$

(R47) $CO_{2(Pt\text{-}int)}\text{-}CO_{Pt}\text{-}H_{Pt}\text{-}OH_s \rightarrow *_{Pt}\text{-}V_{int}\text{-}CO_{Pt}\text{-}H_{Pt}\text{-}OH_s + CO_{2(g)}$

(R48) $*_{Pt}\text{-}V_{int}\text{-}CO_{Pt}\text{-}H_{Pt}\text{-}OH_s + CO_{(g)} \rightarrow 2CO_{Pt}\text{-}V_{int}\text{-}H_{Pt}\text{-}OH_s$

(R49) $2CO_{Pt}\text{-}V_{int}\text{-}H_{Pt}\text{-}OH_s + H_2O_{(g)} \rightarrow 2CO_{Pt}\text{-}H_2O_{(int)}\text{-}H_{Pt}\text{-}OH_s$

(R50) $2CO_{Pt}\text{-}H_2O_{(int)}\text{-}H_{Pt}\text{-}OH_s + *_{Pt} \rightarrow 2CO_{Pt}\text{-}2H_{Pt}\text{-}OH_{int}\text{-}OH_s$

(R51) $2CO_{Pt}\text{-}2H_{Pt}\text{-}OH_{int}\text{-}OH_s \rightarrow 2CO_{Pt}\text{-}OH_{int}\text{-}OH_s + 2*_{Pt} + H_{2(g)}$

(R52) $2CO_{Pt}\text{-}O_{int} + *_{Ce} + H_2O_{(g)} \rightarrow 2CO_{Pt}\text{-}H_2O_{(Ce)}\text{-}O_{int}$

(R53) $2CO_{Pt}\text{-}H_2O_{(Ce)}\text{-}O_{int} + *_{Pt} \rightarrow 2CO_{Pt}\text{-}OH_{(Ce\text{-}Pt)}\text{-}OH_{int}$

(R54) $2CO_{Pt}\text{-}OH_{(Ce\text{-}Pt)}\text{-}OH_{int} \rightarrow CO_{Pt}\text{-}COOH_{Pt}\text{-}OH_{int} + *_{Ce}$

(R55) $CO_{Pt}\text{-}COOH_{Pt}\text{-}OH_{int} + *_{Pt} \rightarrow CO_{Pt}\text{-}CO_{2(Pt)}\text{-}H_{Pt}\text{-}OH_{int}$

(R56) $CO_{Pt}\text{-}CO_{2(Pt)}\text{-}H_{Pt}\text{-}OH_{int} \rightarrow *_{Pt}\text{-}CO_{Pt}\text{-}H_{Pt}\text{-}OH_{int} + CO_{2(g)}$

(R57) $*_{Pt}\text{-}CO_{Pt}\text{-}H_{Pt}\text{-}OH_{int} + CO_{(g)} \rightarrow 2CO_{Pt}\text{-}H_{Pt}\text{-}OH_{int}$

(R58) $2CO_{Pt}\text{-}H_{Pt}\text{-}OH_{int} + *_{Pt} \rightarrow 2CO_{Pt}\text{-}2H_{Pt}\text{-}O_{int}$

(R59) $2CO_{Pt}\text{-}2H_{Pt}\text{-}O_{int} \rightarrow 2CO_{Pt}\text{-}O_{int} + 2*_{Pt} + H_{2(g)}$

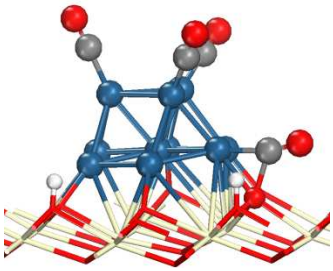

TS-R2

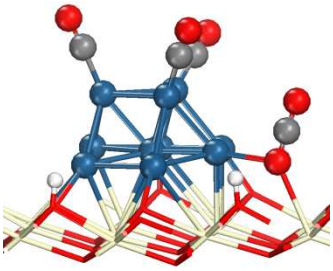

TS-R3

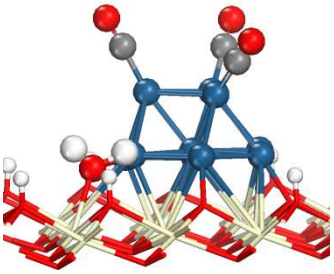

TS-R5

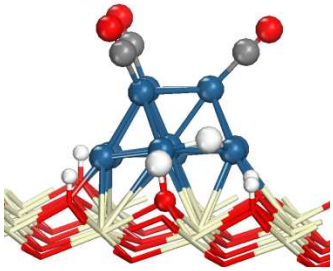

TS-R6

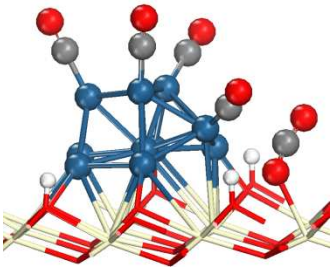

TS-R9

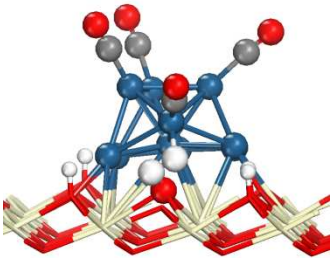

TS-R11

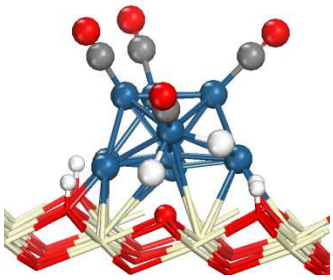

TS-R12

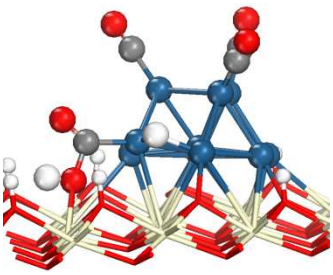

TS-R14

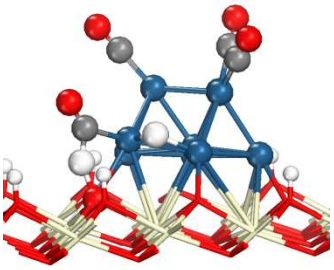

TS-R15

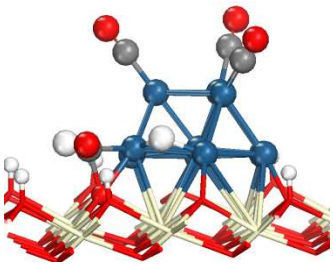

TS-R17

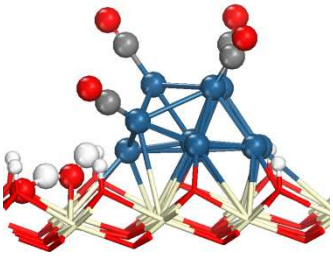

TS-R18

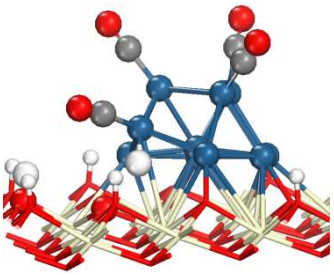

TS-R19

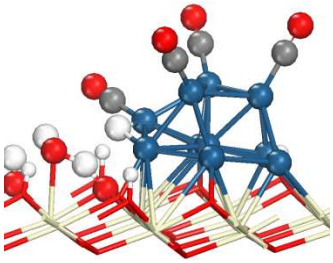

TS-R21

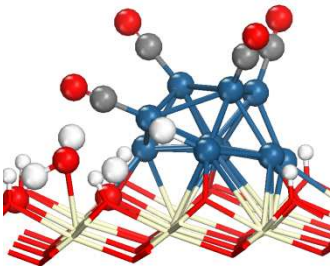

TS-R22

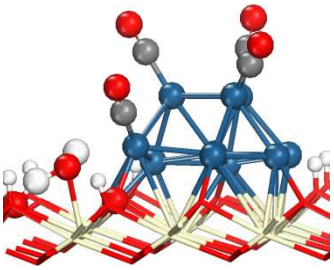

TS-R25

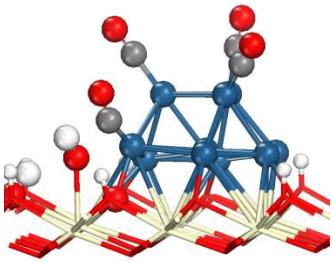

TS-R26

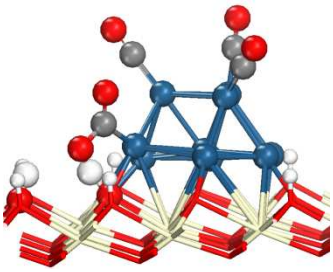

TS-R27

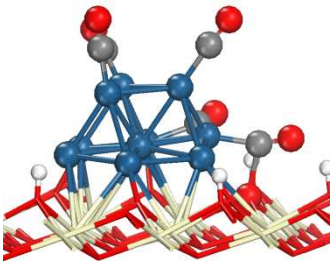

TS-R31

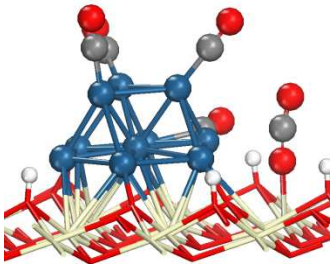

TS-R32

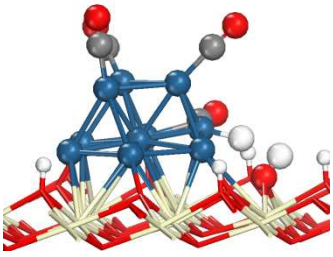

TS-R34

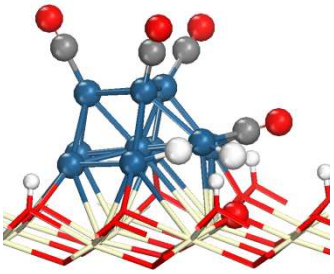

TS-R35

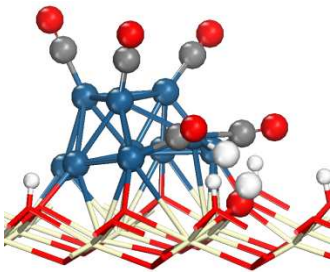

TS-R39

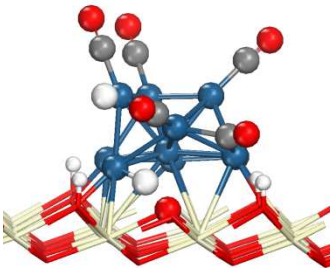

TS-R40

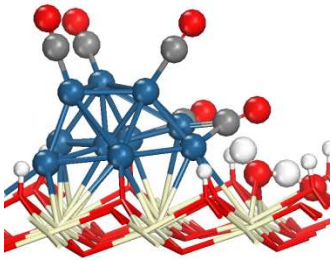

TS-R42

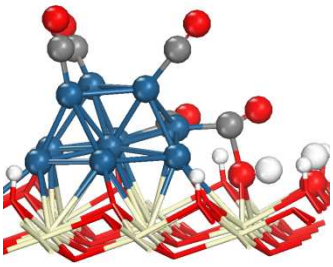

TS-R43

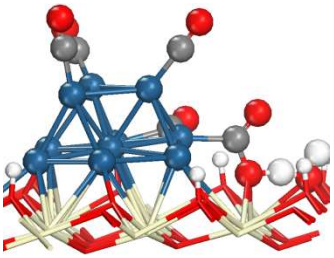

TS-R44

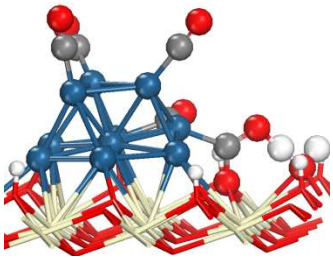

TS-R45

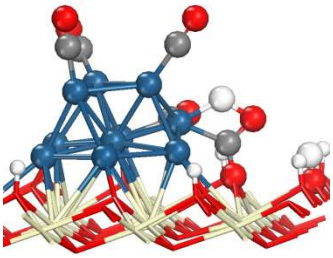

TS-R46

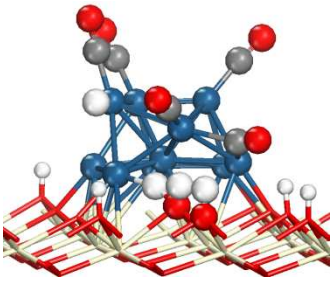

TS-R50

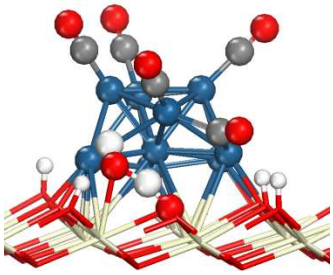

TS-R53

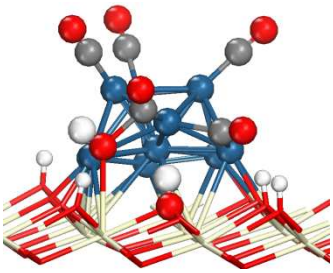

TS-R54

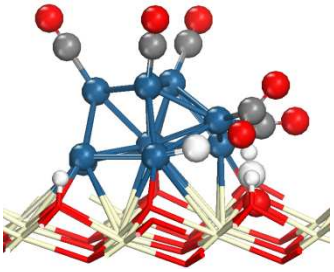

TS-R55

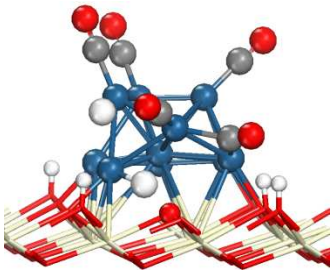

TS-R58